Mechanical Characterization of Carbon Nanosheets

Dissertation

zur

Erlangung der Doktorwüde

der Fakultät für Physik

der Universität Bielefeld

Vorgelegt von

M.Sc. in Physik

Xianghui Zhang

Bielefeld, Oktober 2010

Gutachter: Prof. Dr. Armin Gölzhäuser
Prof. Dr. Peter Reimann

Hiermit erkläre ich an Eides Statt, dass ich die vorliegende Arbeit selbständig und ohne unerlauter Hilfsmittel durchgeführt habe.

Bielefeld,

Abstract

A carbon nanosheet is a new type of two-dimensional material that is fabricated by the electron-induced crosslinking of aromatic self-assembled monolayers. A novel bulge test in an atomic force microscope has been used to study the mechanical properties of carbon nanosheets. The elastic behavior was investigated by analyzing the pressure-deflection relationship in the bulge test. Young's moduli of carbon nanosheets as a function of irradiation electron doses can be determined. With an electron dose above 50 mC/cm^2, BPT nanosheets exhibit a stable Young's modulus ranging from 6 GPa to 8 GPa and NBPT nanosheets ranging from 8 GPa to 10 GPa. CBPS nanosheets have a similar mechanical stiffness which appears to increase slightly at higher electron doses. The residual stresses that have been introduced into carbon nanosheets through the crosslinking and the transferring process are in the range of 40 to 100 MPa. In addition to the adhesion and corrugation of a carbon nanosheet on a SiO_2 substrate, the adhesion between an AFM tip and a freestanding nanosheet was also estimated and analyzed.

The viscoelasticity of carbon nanosheets was investigated with hysteresis, creep and stress relaxation being observed. We were able to probe the creep deformation with a strain rate above 1 % and the resultant creep rates range from $10^{-6}\,s^{-1}$ to $6\times10^{-6}\,s^{-1}$ with a dependence on stress levels. Recovery after creep unloading has also been demonstrated. The ultimate tensile strength of carbon nanosheets was also determined by performing bulge tests. BPT and NBPT nanosheets have tensile strength ranging from 400 MPa to 700 MPa.

We fabricated multilayer carbon nanosheets and the average Young's modulus is demonstrated to be very similar to that of the single layer carbon nanosheet. Overlapping reduces the possibility of a rupture of a monolayer because of defects. Therefore it improves the mechanical stability and enhances the yield of suspended multilayer nanosheets in even larger sizes.

The structural transformation of carbon nanosheets upon annealing has been studied by various analytical techniques. From a mechanical point of view, annealing leads to a systematic increase of Young's moduli with rising temperature, up to 48 GPa at ~1000 K.

Finally, polymer brushes grafted on biphenyl-based nanosheets provided a new class of material termed as "polymer carpet". Both bulge test and nanoindentation were used to characterize the mechanical properties of polymer carpets. The polystyrene carpets experience a decrease in stiffness with decreases of thickness smaller than 20 nm. The polystyrene brush component has a Young's modulus of ~1.3 GPa for the thinnest polystyrene carpet. With a thicknesses over 30 nm, Young's moduli range from 3 GPa to 4 GPa.

Table of contents

Chapter 1

Introduction and Basics

1.1 Two-dimensional materials

Richard P. Feynman, in his classic talk of 1959, pointed out that “there’s plenty of room at the bottom”. He foresaw that a new field of phenomena would come out and could be accompanied by an enormous number of technical applications, if we could manipulate and control things on the molecular or atomic scale. New materials can be synthesized with bottom-up strategies which exploit self-processes for the ordering of supramolecular or solid state architectures from the atomic to the mesosopic scale. Carbyne is an allotrope of the one-dimensional form of carbon that is composed of *sp*-hybridized carbon atoms. As a model for the production of carbyne, polyynes can be synthesized by bolting chains of acetylenic units together. So far, the synthesis of polyynes of up to 44 contiguous *sp*-carbons has been reported [1].

Two-dimensional (2D) materials are some of the most fascinating research targets nowadays [2]. Graphene is an ideal system as a two-dimensional crystalline sheet of carbon atoms, for its infinite number of repetitive elements and long-range order. Strictly speaking, 2D materials are required to be handled as individual molecular units and it is also required that there are no interlayer forces existing in the materials and the two-dimensional structures are held together via inter- and/or intra-molecular interactions. There are many fundamental understandings which need to be clarified, including the basic equilibrium morphologies and their optical properties, transport properties and mechanical properties. Regarding applications, 2D materials can be used as ultrasensitive gas transducers when they are placed over cavities. If they are functionalized with defined anchor groups, 2D materials may serve as sensors to detect even single molecules absorbing on the surface. 2D materials can also provide a platform for the construction of well-defined three dimensional systems. With regard to a much wider range of applications, 2D materials with tunable capabilities in

mechanical stiffness, conductivity and mobility, transparency, morphology and pore size open up new possibilities in nanoscale device fabrication, sensors, imaging, separations, membrane mimetics and so on.

Self-assembled monolayers (SAMs) provide a molecular-thickness limit in 2D materials. Enhancement of the mechanical stability by modification of SAMs allows us to obtain freestanding 2D polymeric nanosheets and handle them individually. However, in terms of a long range order, we may also refer to this new kind of material as “quasi-2D polymeric nanosheet”. They can be utilized as ultrathin and highly transparent supporting materials for nano-sized objects in microscopy methods. They should be very sensitive to external stimuli and may thereby find applications in ultrasensitive sensors. Selective chemical modification or biocompatible modification of the nanosheet improves its reactivity as a chemical or biological sensor.

Both theoretical predictions and experiments on the mechanical properties of 2D materials are quite challenging. The theory of the elasticity of 2D systems has been discussed and mainly applied to solid Langmuir-Blodgett films [3]. As a true 2D material, graphene can be modeled as a membrane with zero bending stiffness. However, suspended graphene sheets exhibit random distributed ripples that indicate interactions between bending and stretching long-wavelength phonons [4]. In the same way, the bending stiffness of carbon nanosheets is not kept at zero but can be neglected in comparison with in-plane stiffness. It indicates that the in-plane deformation of carbon nanosheets could provide more useful information. According to the scaling law for 2D materials, the magnitude of deformation under load is proportional to scale. The first difficult task is to find a suitable experimental method to deform this molecular-thick nanosheet. In order to understand the general nature of the experiment data, a suitable theoretical model is also required for analysis.

In this chapter, we will give a basic introduction related to SAMs and electron-induced modifications of SAMs as well as an outline of the thesis will be also described.

1.2 Self-assembled monolayers (SAMs)

A monolayer is a single closely packed layer of atoms or molecules. In 1917, Langmuir investigated a large number of amphiphilic molecules on a water surface to figure out the forces involved in the adsorption and surface tension [5]. These amphiphilic molecules spreading upon an aqueous surface are called Langmuir monolayers. Later, Langmuir and Blodgett transferred the monomolecular layers from a water surface to a solid substrate, and multilayers (20~200 layers), which could be deposited on various substrates [6, 7]. The monolayer and multilayers that have been deposited onto a solid substrate are named Langmuir-Blodgett films. Even a single layer could be seen on polished chromium by using polarized light. The refractive index of those multilayers was determined from the reflection intensity of monochromatic light. These earlier studies were driven by the study of surface tension.

In 1946, Zisman prepared a monomolecular layer by self-assembly of a surfactant onto a clean metal surface [8]. In 1980s, Sagiv reported the preparation of *n* -octadecyltrichlorosilane (OTS) monolayers on various solid polar substrates in solution [9]. Nuzzo and Allara also reported the preparation of a series of organic disulfides that have been adsorbed on gold substrates in dilute solutions [10]. Since then, many other SAMs have been prepared and investigated among which

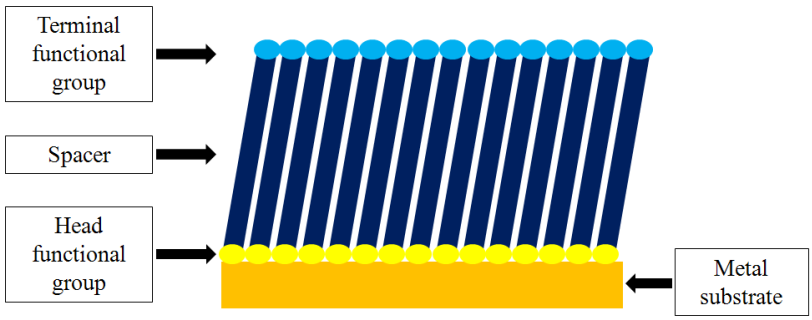

Fig. 1 Schematic diagram of SAMs on a metal surface

alkanethiolates on gold are probably the most extensively studied system. SAMs of thiols on a gold substrate have been used to study interfacial phenomena including wetting [11], adhesion [12], tribology [13, 14], crystallization [15], electron transport [16], biochemistry and biology [17, 18].

The molecules for preparing SAMs consist of three parts: (1) a head functional group which can be chemically absorbed on a metal substrate, (2) a terminal functional group which determines the surface properties of SAMs, (3) in between there is a molecular backbone which provides a well-defined thickness, mechanical stability, electronic conductivity and optical properties, as schematically shown in fig. 1.

The self assembly process can be achieved either from the solution or from the gas phase. In general, the formation of SAMs is not a single step process and it comprises multiple time scales and phases. Adsorption of docosanethiol ($CH_3(CH_2)_{21}SH$) investigated by nonlinear vibrational spectroscopy indicates three different steps [19]: (1) a fast initial adsorption step described by Langmuir kinetics results in the coverage of 80~90 % and the time scale is 5~6 minutes, this step is related to chemisorptions of the head group; (2) a second step indicates a transition of hydrocarbon chains from a highly kinked to an all-trans conformation and the time scale is 3~4 times slower than the first step, this step is related to straightening of hydrocarbon chains; (3) a third step proceeds even slower (35~70 times slower than the second step) and it is related to reorientation of terminal functional groups. Both ex-situ and in-situ analytical techniques have also been used to investigate SAMs formation kinetics, such as electrochemical quartz crystal microbalance (EQCM) [20], grazing incidence X-ray diffraction (GIXD) [21], surface plasmon resonance (SPR) [22], atomic force microscope (AFM) [23], Fourier transform infrared reflection absorption spectroscopy (FT-IRRAS) [24] and so on.

The reaction to forming SAMs on gold from thiols involves the breakage of a RS-H bond and formation of a RS-Au bond. The typical adsorption process of alkanethiol on Au can be expressed as follows:

$$CH_3(CH_2)_nSH+Au \rightarrow CH_3(CH_2)_nS\text{-}Au+\frac{1}{2}H_2 \quad (1)$$

Taking into account the thermodynamics of monolayer formation, there is a balance between enthalpic contributions of the reaction and entropy associated with the self assembly process. The adsorption enthalpy was found to be -20 kcal/mol [25]. The bond dissociation energy for RS-H and RS-Au is estimated to be ~87 kcal/mol and ~40 kcal/mol, respectively. In addition, the formation of molecular hydrogen is favored over the dissolution of $H^{\bullet}$ into an Au matrix, for the reaction $2H^{\bullet} \rightarrow H_2$, $\Delta h = -104$ kcal/mol. The heat involved in the reaction is -5 kcal/mol, which is available in the reactant. Self-assembly is a process from a disordered to an ordered system which indicates negative entropy associated with the formation of monolayer. The entropy of adsorption is determined to be -48 kcal/mol [26].

Apart from the most extensively studied n-alkanethiol (AT) SAMs, thioaromatic SAMs are expected to have a different relation between intermolecular and headgroup-substrate interactions. In comparison to AT molecules, thioaromatic molecules have a more rigid chain which may have an influence on the molecular structure and coverage. 4-methyl-4'-mercaptobiphenyl assembled on Au (111) has been investigated by GIXD and low-energy atomic diffraction (LEAD) and two phases of different density similar to AT thiols were observed. In the low-density "stripped" phase, a commensurate rectangular $\left(8\times 2\sqrt{3}\right)$ structure was identified. In the high-density "standing-up" phase, a commensurate hexagonal $\left(\sqrt{3}\times\sqrt{3}\right)R30^{o}$ structure was found [27]. Self-assembled monolayers formed from thiophenol, 1,1'-biphenyl-4-thiol, 1,1';4',1''-terphenyl-4-thiol and anthracene-2-thiol on polycrystalline Au and Ag were characterized by X-ray photoelectron spectroscopy and angle-resolved near-edge X-ray absorption fine structure spectroscopy and it was found that the molecular orientations and orientational order of the adsorbed thioaromatic molecules depend on the number of aromatic rings, the substrate, and the rigidity of the aromatic system [28].

1.3 Electron-induced modification of SAMs

The damage of X-rays, electrons and X-ray generated primary and secondary electrons on organic molecules and biological systems have attracted growing attention. SAMs have been used as a system for understanding the mechanism behind the damage done to organic molecules that are exposed to x-rays [29]. It indicates that the electrons instead of x-rays are responsible for the damage to SAMs. The genotoxic effect of ionizing radiation (x-rays) in living cells was investigated by detecting the transformation of DNA molecules due to the low energy electrons irradiation. It was illustrated by the mechanism that electrons initiate fragmentation of small molecules by the attachment of the incident electron which leads to the formation of a transient molecular resonance that subsequently decays either via electron autodetachment or bond dissociation [30, 31]. Dissociative electron attachment (DEA) is considered to contribute significantly to these damages. The DEA process can be represented by:

$$AB + e^{-} \rightarrow AB^{-*} \rightarrow A^{-} + B \qquad (2)$$

where AB^{-*} is a superexcited state of the molecular anion which can dissociate to give molecular fragments A^{-} and B.

The damage of alkanethiol SAMs has been intensively investigated by various analytical techniques, such as X-ray photoelectron spectroscopy (XPS) [32, 33], angle-resolved near edge X-ray absorption fine structure spectroscopy (NEXAFS) [33, 34], infrared reflection-absorption spectroscopy (IRAS) [34], surface enhanced Raman spectroscopy (SERS) [35], static secondary ion mass spectroscopy (SIMS) [36], advancing water contact angle measurements [34] and electron stimulated desorption (ESD) [37]. Upon electron exposure, alkanethiol SAMs undergo cleavage of $C-H$, $C-S$ and $C-C$ bonds, formation of crosslinking $C=C$ bonds and desorption of small molecular species including H_2, CH_2CH_3 and $CH_2CH_2CH_3$. Furthermore, cleavage of Au-thiolate bonds, desorption of S-containing fragments and appearance of disulfide, degradation of SAM-vacuum interface were also observed.

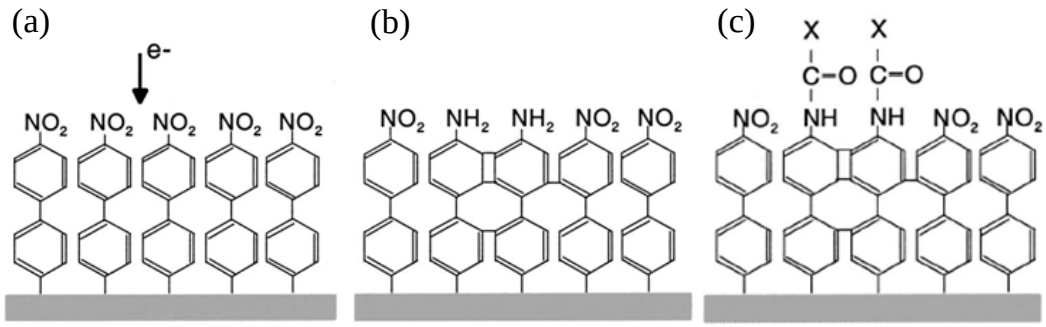

Fig. 2 Schematics of the electron induced crosslinking process: (a) NBPT SAMs are exposed to the low energy electrons; (b) SAMs are dehydrogenated and crosslinked, with terminal nitro group turning into amino group; (c) Amino group can be used to couple other molecules. (Images taken from reference 41)

Therefore alkanethiol SAMs have been demonstrated to act as self-developing positive electron beam resists. The critical electron dose that cause substantial change of SAMs is influenced by substrate conductivity and molecular structures [38].

For aromatic SAMs, the low-energy electron induced modification has been explored with XPS, NEXAS, AFM and infrared spectroscopy (IR) [39-41]. Unlike aliphatic SAMs being damaged when exposed to electrons, aromatic molecules remain bonded on the substrate and maintain their orientation. An increased etching resistance and changes in IR spectra were observed. Formation of crosslinking between adjacent molecules has been demonstrated, which implies that aromatic SAMs can be used as negative electron beam resists. Furthermore, the nitro group terminated aromatic

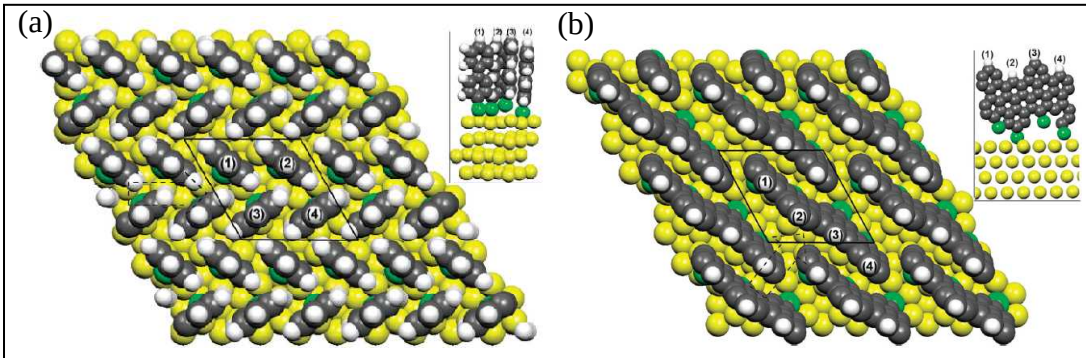

Fig. 3 (a) DFT-optimized BPT SAMs on Au(111) following the $2\sqrt{3}\times\sqrt{3}$ superstructure. (b) After dehydrogenation BPT SAMs form “graphene-like” nanoflakes. Insets indicate side views of four BPT units. (Images from reference 43)

SAMs undergo conversion of a nitro group into an amino group, which is utilized as “chemical nanolithography” for immobilizing a variety of molecules on specific patterns in molecular nanotechnology and biology [41]. The electron induced crosslinking process on NBPT SAMs is schematically shown in fig. 2.

A very detailed model of electron-induced crosslinking in aromatic SAMs based on experimental and theoretical analysis has been presented by Turchanin [42]. The UV-photoelectron spectra (UPS) suggest a prevailing formation of stable dimers with four C-C crosslinks between two adjacent biphenyl molecules. Density functional theory (DFT) calculations have been performed to understand electron-induced cross-linking of biphenylthiol SAMs on Au (111) [43]. After dehydrogenation of BPT SAMs, molecules tend to interact covalently to spontaneously form small “graphene-like” nanoflakes, as schematically shown in fig. 3. However, the mechanism of electron-induced crosslinking is far more complex than that is currently understood, and other analytical techniques such as scanning tunneling microscope (STM) are required to perform more detailed experiments.

1.4 Outline of the thesis

A basic introduction related to SAMs and electron-induced modifications of SAMs is presented in this chapter. Chapter two will give fundamental principles of techniques involved in our experiments. The operational principle of the AFM is to be presented firstly, followed by scanning electron microscope (SEM), XPS, photolithography, critical point drying (CPD) and so on. The experimental details of SAM preparation, crosslinking and transferring will also be presented in this chapter.

Chapter three introduces experiments and theory of bulge test which is the most widely used method for the mechanical characterization of free standing thin films. Two methods (Line Scanning Method and Central Point Method) for determining the deflection of membranes are presented in detail and the AFM point deflection method and some results will also be presented in this chapter.

Chapter four discusses the mechanical properties of carbon nanosheets. First the adhesion and corrugation between a carbon nanosheet and a substrate will be discussed. The elastic response and viscoelasticity of carbon nanosheets are investigated by means of bulge test. Young's modulus and the residual stress of carbon nanosheets which are prepared from different molecules are derived and the electron dose effect is also investigated. A rupture test is utilized to determine the ultimate tensile strength of carbon nanosheets. Furthermore, multilayer carbon nanosheets and annealed nanosheets will also be presented in this chapter.

Chapter five presents the mechanical properties of polymer carpets. The fabrication of polymer carpets is described and a theoretical analysis of such a composite system is discussed. Young's modulus as a function of polymerization time is reported and discussed. Nanoindentation has also been employed to determine the hardness and the elastic modulus of the polymer carpet.

Chapter 2

Experimental

2.1 Experimental techniques

2.1.1 Atomic force microscope (AFM)

In 1986, Binnig, Quate and Gerber invented the first atomic force microscope that has overcome disadvantages of the STM which has limited applications on conductive or conducting layer coated specimen.

An AFM has a general set-up with a sharp tip (with a radius of typically 10~100 nm) mounted on a micro-machined cantilever. The tip was brought in a well-controlled close proximity to the sample. During the scanning process, interaction forces between the tip and the sample result in the bending of the cantilever, as shown in fig. 4. Vertical bending from its equilibrium is proportional to the normal force applied to the tip, while lateral forces cause a twisting of the cantilever. A piezoelectric tube is

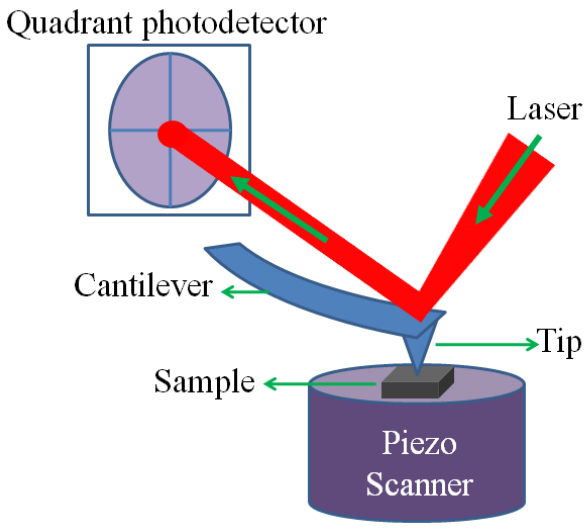

Fig. 4 Schematic diagram of a general AFM set-up: A laser beam is transmitted and focused on the backside of a cantilever and reflected from it into a four-quadrant photodetector. A sample is mounted on a piezo tube that can move the sample in three directions.

used as a stage for mounting the samples. It can move in z direction for maintaining a constant force or a constant height, also in X and Y direction for scanning the samples. Measurements can be done in a variety of environments, such as ambient air, liquid and ultrahigh vacuum (UHV).

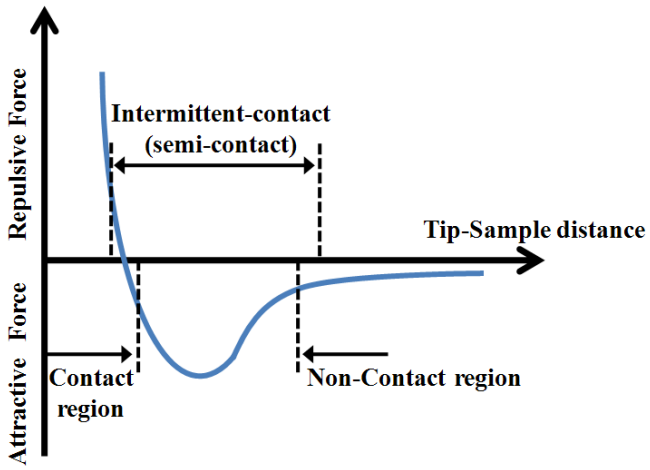

Fig. 5 Idealized sketch of tip-sample forces. Different operation modes can be performed in contact region, intermittent contact or non-contact region.

In the **contact mode** of operation, the cantilever bending under scanning reflects a repulsive force between tip and sample. It mainly contains the constant force mode, the constant height mode and the lateral force mode. In the former two modes, a vertical cantilever deflection is measured by an optical beam method and converted into an electrical signal DFL. In the *constant force mode* of operation, the deflection of cantilever is maintained by the feedback circuit on the preset value, so that the vertical displacement of the scanner gives rise to the topography of the sample under investigation. In the *constant height mode* of the operation, the scanner maintains a fixed end of the cantilever on the constant height value, so that the deflection of cantilever gives rise to the topography of the sample under investigation. In the *lateral force mode*, besides the cantilever deflection in normal direction, an additional torsion bending of cantilever occurs and thus is used to record the lateral force. The main advantage of the contact mode is high scanning speed. Its disadvantage is requirement of a sufficiently smooth surface. The damages due to scratching with tip have a high

probability to happen on soft materials such as polymers and biological specimen.

In the **intermittent contact** mode of operation, an oscillating cantilever close to or at its fundamental resonance frequency is used to scan the sample. The force sensed by the tip is not only an attractive force but also a repulsive force that concerns oscillation with a relatively high amplitude (typically 100~200 nm). Such a force gradient has an influence on the vibration amplitude of the cantilever and also on the frequency of the cantilever. A feedback system adjusts the height of the cantilever base to maintain the vibration amplitude at a constant set-point value. Therefore the topography of the sample is achieved. A phase shift occurs in the inhomogeneous sample and thus the phase contrast imaging mode will give additional information on the material being scanned.

In the **non-contact mode** of operation, the cantilever is forced to vibrate at a preset frequency slightly above its resonance frequency. The amplitude of oscillation is in the range of a few nanometers (less than 10 nm) where a long range attractive force dominates. This has the advantage that the tip never gets into contact with the sample and therefore it can be avoided destroying the samples.

Tip-sample interactions

When the tip and the sample are in contact, the elastic forces give rise to both sample and tip deformations. If we consider only the elastic force, the elastic deformation in the contact zone is termed as Hertzian theory. The solution relates to the loading force F and the penetration depth h:

$$F = ER^{1/2}h^{3/2} = \frac{4}{3}\frac{Ea^3}{R} \tag{3}$$

where R , a and E are the tip curvature radius, the contact circle radius and the reduced Young's modulus for the tip and the sample by the equation below

$$\frac{1}{E} = \frac{1-\nu_{tip}^2}{E_{tip}} + \frac{1-\nu_{sample}^2}{E_{sample}} \tag{4}$$

The Johnson, Kendall and Roberts (JKR) model considered the adhesion within the contact regime in a Hertz model, which accounts for the influence of the Van der Waals force within the contact zone [44].

$$F = \frac{4}{3}\frac{Ea^3}{R} - \sqrt{8\pi\gamma Ea^3} \tag{5}$$

whereas γ is the work of adhesion.

The Derjagin Muller and Toropov (DMT) theory also considered Van der Waals interactions outside the elastic contact regime and was applied to tips with a small curvature radius and high stiffness, which weakens the elastic repulsive forces [45].

$$F = \frac{4}{3}\frac{Ea^3}{R} - 2\pi R\gamma \tag{6}$$

Since water adsorbs at many surfaces, it tends to wet the tip and may form a concave or convex meniscus in between the tip and the sample. The maximum attractive capillary force acting on the tip is simply given by

$$F_c = -4\pi\gamma R\cos\theta \tag{7}$$

where the contact angles θ with the sample and the tip are assumed to be equal.

When the tip is away from the sample, Van der Waals interaction has to be taken into account. Considering the probe with a sphere at a small tip-sample separation, the corresponding force is given as

$$F = \frac{\pi^2 n_1 n_2 AR}{6h^2} \tag{8}$$

where A is the Hamaker constant ($A \approx 10^{-78}\,\mathrm{J\cdot m^6}$), n_1 and n_2 are the concentrations of tip and sample molecules, h is the tip-sample separation. For the tip radius of 10 nm and separation of 0.1 nm, the force is $3.3\times10^{-9}\,\mathrm{N}$.

2.1.2 Scanning electron microscope (SEM)

The first commercial SEM was developed by Charles Oatley and Gary Stewart in 1965. It is widely used to image the sample surface from signals of interactions between electrons and atoms of the sample. Characteristic information from SEM comprises topography, morphology, composition and crystallographic information.

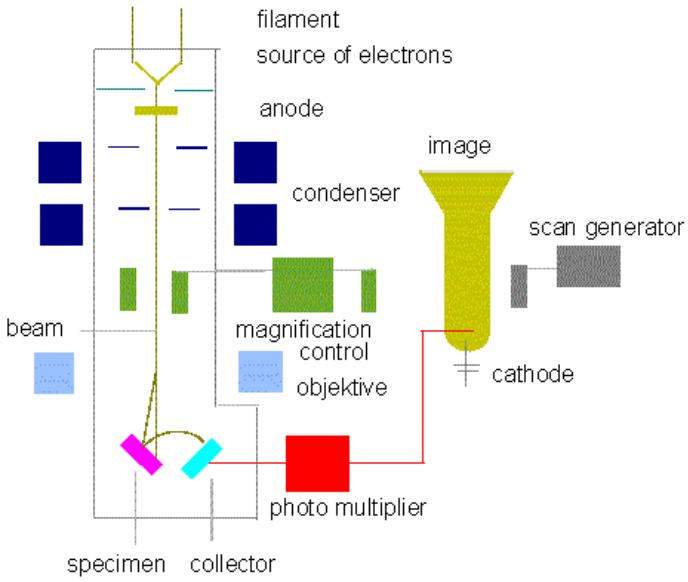

Fig. 6 Block diagram of a typical SEM (Image redrawn from J.W.S. Hearle, J.T. Sparrow, P.M. Cross, 1972)

The electron beam is emitted from the filament cathode (e.g. tungsten) in the electron gun. The beam is then focused by two condenser lenses: the first one forms the beam and limits the amount of current in the beam and the second one forms the beam into a thin and coherent beam with a spot size 0.4~5 nm. The beam then passes through a set of scan coils which are usually located in the final lens to sweep the beam in a raster fashion with a certain scan speed to focus the beam on the part of sample being investigated. The secondary electrons being emitted from the sample are collected and analyzed by a detector which gives a topographic contrast. The backscattered electrons may also be detected to give further compositional contrast.

2.1.3 X-ray photoelectron spectroscopy (XPS)

XPS is a technique for surface analysis, such as elemental composition, chemical or electronic state of elements, and in-depth distribution of elements. In 1954 XPS equipment was developed by Kai Siegbahn who received a Nobel Prize in 1981 for this work. The mechanism of XPS is based on the photoelectric effect which describes the ejection of electrons when photons are impinging on the surface. In an UHV environment, monochromatic X-rays are used to irradiate the sample and the energy of those emitted photoelectrons are analyzed by an electrostatic analyzer before the intensity of the defined energy is recorded by a detector.

At an atom with a core hole created by X-ray photons, you can observe the decay of an electron from a higher energy level to fill the vacancy in several ways, either in the form of characteristic X-ray, or in the form of an Auger electron emitted from an outer shell.

The kinetic energy of ejected photoelectrons E_K is determined by the energy of X-ray radiation, $h\nu$, binding energy of core electrons, E_B, and work function of spectrometer, Φ_{SP}.

$$E_K = h\nu - E_B - \Phi_{SP} \tag{9}$$

Due to the fact that the binding energy is characteristic of core electrons for each element, it also depends on the chemical state of that atom, such as oxidation states and ligands of that atom.

However, unlike the photoelectric lines, the kinetic energy of Auger lines are independent of photon energy of the X-ray source and only correspond to the difference between the states involved in the whole process, which is the energy of initial electronic transition and the ionization energy of the electron shell from which the Auger electron was emitted.

If the attenuation length of electrons could be determined by experiments and the

elastic electron scattering was neglected, the thickness of an overlayer thin film can be determined by comparison of the XPS signal between the clean substrate and that of the specimen.

$$I_S = I_S^0 \exp(-\frac{t}{\lambda \cos\theta}) \tag{10}$$

where t is the thickness of the overlayer film, I_S is the substrate intensity from under the overlayer thin film, and I_S^0 is the pure substrate intensity, θ is the emission angle and λ is the attenuation length of the electrons of the thin film material. In order to collect photoelectrons at a more grazing emission angle, the analyzed region can be made more surface-localized and the sensitivity increased.

XPS detects those electrons ejected from the surface of the specimen. The deeper emitted photoelectrons ($t \geq 5\lambda$) would be captured or trapped into the material due to the limitation of the mean free path of low energy electrons. Fig. 7 shows the mean free path of electrons in solids as a function of electron energy.

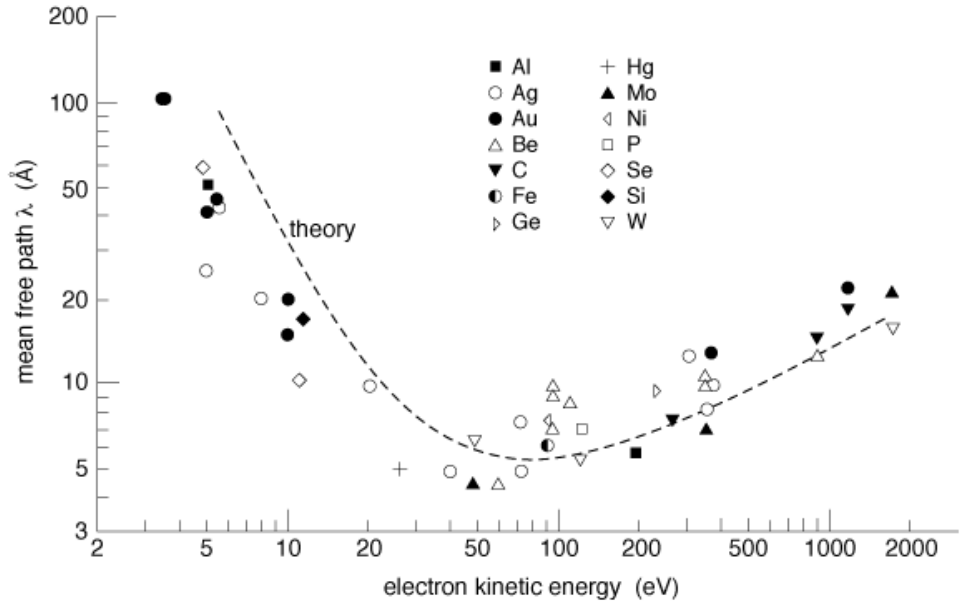

Fig. 7 The mean free path of electrons in solids, the dashed curve is theoretical calculation and the dots are experimental measurements [47].

2.1.4 Photolithography

Optical photolithography is a process of transferring a geometric pattern from a photo mask to a light-sensitive photoresist on the substrate. It has been a crucial technique in the development of the semiconductor industry from the traditional planar process to current super-large-scale integration (SLSI) with one million to ten million transistors on single chip. The process combines several complex steps in sequence: cleaning, spin coating, pre-baking or soft baking, exposure, post exposure baking, development, etching, photoresist removal and so on.

Fig. 8 describes a simple scheme of photolithography, where photoresists are classified into positive and negative types. For positive photoresists, the exposed regions become soluble to the developer and the unexposed regions remain insoluble to the developer. For negative photoresists, the exposed regions become insoluble to the developer and the unexposed regions are still soluble to the developer.

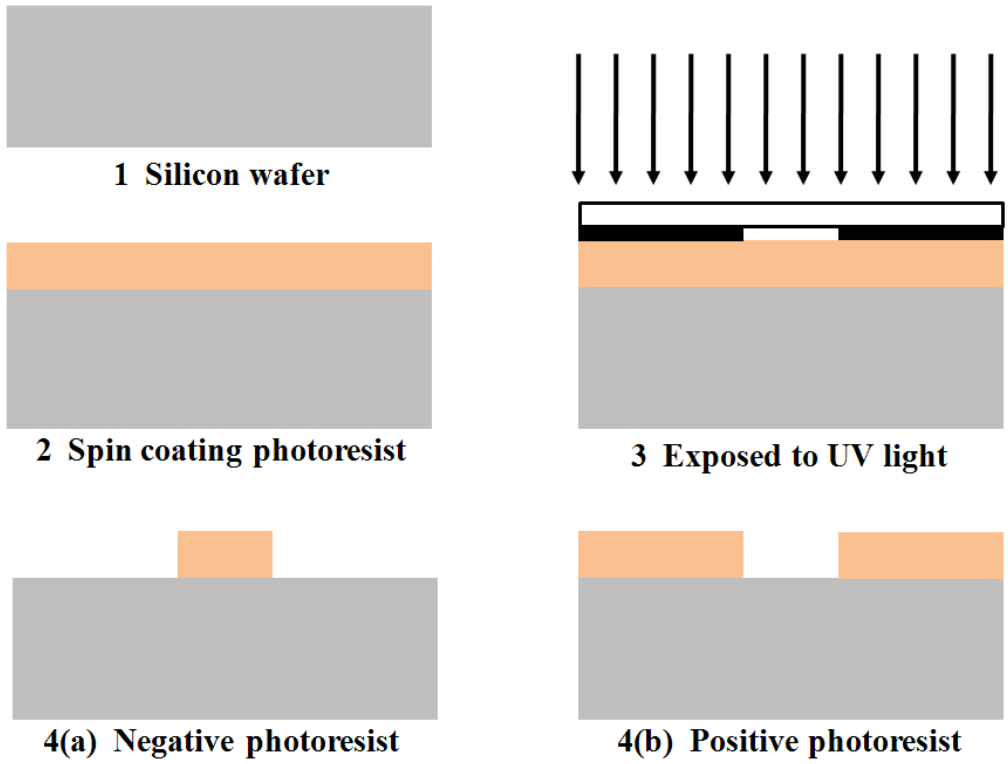

Fig. 8 Scheme of photolithography: 1) Cleaning the silicon wafer; 2) Spin coating the photoresist on the wafer; 3) Expose the photoresist to UV light through a photo mask; 4) For a negative photoresist the exposed region remain on the wafer, however for a positive photoresist the unexposed regions remain on the wafer after development.

There are three major exposure methods: contact printing, proximity printing and projection printing. Contact printing provides physical contact between the photomask and the photoresist and allows for high resolution (0.5~1 um). In proximity printing, a small gap from a few microns to tens of microns between the photomask and the photoresist is maintained to avoid damages. Proximity printing has a resolution of 2~4 microns. In projection printing, patterns are transferred by optical imaging of a photomask on photoresist. The resolution depends on the optical imaging system. In our work, soft contact printing is utilized to get a high resolution of structures.

After development and removal of undesired photoresist, etching is carried out to remove materials from the wafer. It consists of wet etching and dry etching: wet etching utilizes liquid chemicals and etchants; dry etching is usually accomplished by chemical reactions using reactive gases or plasma with high selectivity. In our work, wet etching is the primary method to remove Au, Cr, SiO_2, Si_3N_4, and Silicon.

Apart from the rigid silicon wafer as rigid substrate on which complex nanostructures are constructed, soft and elastomeric substrates are also being desired to build flexible plastic optoelectronic systems. Poly (dimethysiloxane) (PDMS) is one excellent example for such a purpose. Patterned metal on a PDMS substrate with small feature sizes can be generated using optical lithography. Annealed carbon nanosheets can be transferred on a PDMS stamp with well-controlled metal electrodes, piezoelectricity properties are investigated by stretching or compressing the flexible PDMS stamps.

Furthermore, patterned Au/PDMS can be employed directly as a photomask which has some additional advantages compared to a rigid photomask. Edge-pattern generation widens its applications and metal cracks can be avoided. A soft and flexible photomask might contribute to organic semiconductor devices.

2.1.5 Critical point drying

Critical point drying is a method to remove liquid in a controlled way, without collapsing or deforming the structure of wet specimens. It is widely used in the preparation of biological specimens for SEM. It is also used in the final fabrication step of releasing microstructures in the Micro- Electro-Mechanical Systems (MEMS) devices. The reason for the specimens being damaged by normal air drying is due to large surface tension created in a liquid/gas interface. During the air drying process, liquid/gas interface moves and the surface tension causes the collapse of those structures.

In critical point drying, a dehydrating fluid miscible with water such as ethanol or acetone gradually replaces the water contained in a specimen. The next step is to substitute a transitional fluid for the dehydrating fluid in the specimen and then removing the transitional fluid. The transitional fluid commonly used is carbon dioxide (CO_2) and the critical temperature and pressure of carbon dioxide are 31° C. and 1,072 psi, respectively. Then the specimens are heated and pressurized above the critical pressure and critical temperature. The critical point of a liquid is when its temperature and pressure are at or above the critical temperature and pressure and the densities of the liquid phase and vapor phase are equal. This absence of a phase boundary eliminates surface tension that exists when changing a liquid to a gas.

In our case, a double layer PMMA needs to be removed by acetone from the surface of a monolayer. Specimens are immersed carefully into the cylindrical drying chamber of the Critical Point Dryer (Tousimis Autosamdri-815B, Series B) that is filled with acetone. After PMMA is completely dissolved by acetone (60 min), CO_2 is introduced into the chamber to replace acetone according to a predefined time. Finally the dryer heats and pressurizes CO_2 to its critical point and gas CO_2 bleeds off to leave the monolayer dry.

2.1.6 Nanoindentation

Nanoindentation tests were carried out with Agilent Nanoindenter G200, as shown in fig. 9a. It can be utilized to determine Young's modulus and the hardness of the desired materials. A G200 enables the measurement of deformation over six orders of magnitude from nanometers to millimeters. The actuating and sensing mechanism is shown schematically in fig. 9b. A load is exerted through the coil-magnet assembly by controlling the current in the coil which is mounted on top of the indenter column. The field of the coil acts against the permanent magnet and a force is exerted onto the column. The indenter column is supported by very delicate leaf springs, which are parts of the capacitance device for measuring the displacement of the indenter column. The stage is mobile for positioning the sample with an accuracy of $1\,um$.

The robust standard G200 XP head uses a pyramidal diamond Berkovich indenter tip and applies the continuous stiffness technique. A Berkovich indenter is a three faceted tip with semi angle (θ) of 65.3^{o}.

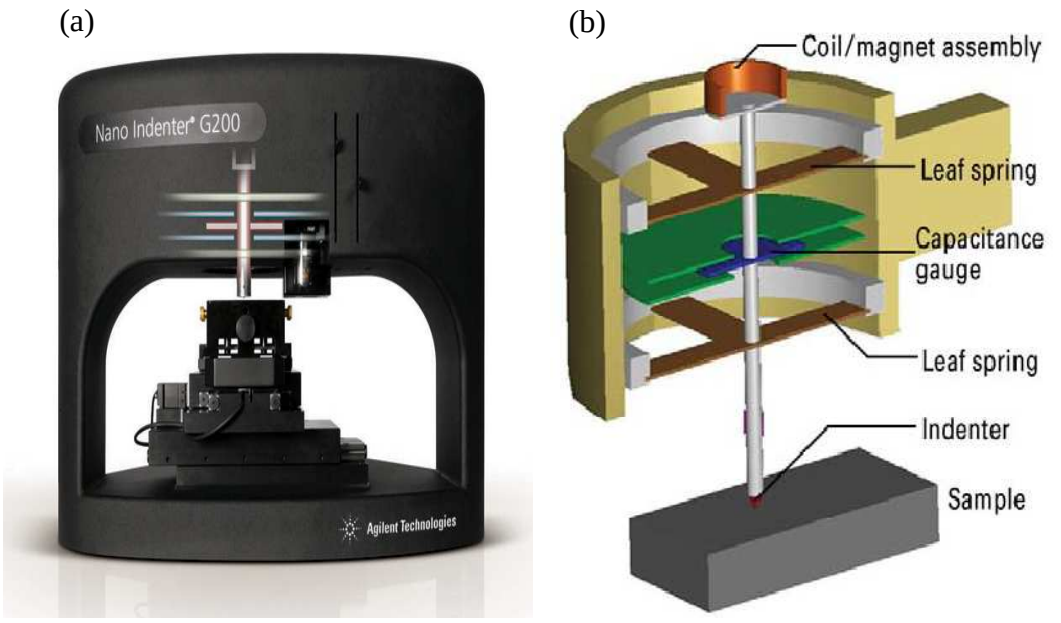

Fig. 9 (a) The instrument image of Agilent Nano Indenter G200; (b) The schematic diagram of the actuating and sensing mechanism of the Nano Indenter G200 [48].

2.2 Experimental aspects

2.2.1 SAM preparation

Preparation of BPT/NBPT SAMs

For the preparation of 1,1'-biphenyl-4-thiol (BPT) self-assembled monolayers (SAMs) and 4'-Nitro-1,1'-biphenyl-4-thiol (NBPT) SAMs, we use a 300 nm polycrystalline Au layer with (111) crystal planes epitaxied-grown on a mica substrate (Georg Albert Physical vapor Deposition). The substrates are put into an UV-Ozone cleaner (UVOH 150 LAB FHR Anlagenbau) for 5 min in order to remove main organic contaminations from the surface. After that the substrates are rinsed with ethanol twice and blown dry in nitrogen stream. Subsequently the substrates are immersed into a ~10 ml solution of dry and degassed dimethylformamide (DMF) with 10 mmol BPT or NBPT molecules for 72 h in a sealed flask under nitrogen atmosphere. After the samples are taken out, they are rinsed firstly with DMF and then with ethanol twice, blown dry in a stream of nitrogen.

Preparation of CBPS SAMs

To prepare 4'-[(3-trimethoxysilyl)propoxy]-[1,1'-biphenyl]-4-carbonitril (CBPS) SAMs, we use silicon nitride substrates (150 nm Si_3N_4 /10 nm SiO_2, CrysTec, Germany). The substrates are cleaned with Piranha solution (H_2SO_4:H_2O_2 in volume ratio of 3:1) for 20 min to remove organic residues. The substrates are rinsed firstly with purified water and mounted on a Teflon sample holder under water. Then the substrates are rinsed with fresh purified water again and then with methanol, and blown dry in a stream of nitrogen. Afterwards the substrates are immersed into a ~10 ml solution of dry and degassed toluene with 10 mmol CBPS molecules for 120 h in a sealed flask under nitrogen atmosphere. After being taken out, they are rinsed firstly with ethyl acetate and mounted on a Teflon sample holder under solvent. Then the samples are rinsed with fresh ethyl acetate again and then with methanol, and blown dry in nitrogen.

Sample storage

In order to avoid contamination from moisture or oxidization, samples are always stored in Petri dishes with a piece of cleanroom paper on the bottom. The Petri dishes are filled with an argon atmosphere and sealed off with Parafilm (Alcan Packaging) strips.

2.2.2 Electron irradiation of SAMs

Electron-induced crosslinking of aromatic SAMs is achieved in a home-made projection lithography instrument. For BPT and NBPT SAMs, the samples are simply mounted on the sample stage with clamps for the purpose of fastening and electrical contact. For CBPS SAMs, electrical contact is attained by gently scratching continuous cross lines on the blank margin of the sample with a diamond cutter and adding gallium indium eutectic (99.99%, Sigma-Aldrich, Germany) and conductive pure silver paint (Conrad). Then wait for 10 min until the electrical contact is dry and then mount the sample with the conducting region having close contact with the clamps.

Afterwards the samples are put into a vacuum chamber where a high vacuum ($<5\times 10^{-8}$ mbar) can be achieved approximately 1h after both the rotary vane pump and turbomolecular pump are switched on. Electron irradiation is operated with an electron floodgun at an electron energy of 100 eV and a current of 3 mA. The electron beam is made much more homogeneous with a scan controller that is mounted at the lower part of the cylinder where a filament is inside. Electron doses are calibrated from five faraday cups which are located beneath the metal plate for the holding of the samples. A typical electron dose of 50 mC/cm^2 is required to obtain the fully crosslinked SAMs.

Patterning of SAMs is attained by placing a shadow mask, e.g. grid for transmission electron microscope (TEM) in close proximity to the surface of the samples, with clamps which are used for the purpose of close contact and eliminating the charging effect.

2.2.3 Transferring of carbon nanosheets

Double layer Electron-Beam resist poly(methyl methacrylate) (PMMA) are used as a transfer medium. The first layer is PMMA (50K, AR-P 631.09, Allresist) with a lower molecular weight which will be further diluted to a 4% solid content with chlorobenzene. This layer assures the cleanness of nanosheets because it can easily and more completely be removed. The first layer is spincoated to a nominal thickness of 130 nm at 2000 rpm for 30 s and baked on a hotplate at 90℃ for 5 min. The second layer PMMA (950K, AR-P 671.04, Allresist) with a higher molecular weight provides a mechanical stability for the transferring process. The second layer is spincoated to a nominal thickness of 310 nm at 4000 rpm for 30 s and also baked at 90℃ for 5 min. For Au/mica substrates, all four edges are cut ~1 mm with a scissor from the samples to avoid resists' blocking in the releasing process. For silicon substrates, the edges covering the resists are either broken off using a diamond cutter or gently scratched with a sharp blade.

The traditional way to release PMMA/nanosheet/Au from mica is the immersion of the sample in hydrofluoric acid (48 %) for 20~60 min. Mica is thus etched both from the back side and its lateral interface with Au. The separation of PMMA/nanosheet/Au from mica is attained by carefully dipping the sample into water. We found recently that the sample floats on the liquid level of I_2/KI etching bath (I_2:KI:H_2O with ratio of 1g:2g:10ml) for 20~60 min and the Au layer is also etched laterally which allows us to separate PMMA/nanosheet/Au and mica. Afterwards the PMMA/nanosheet/Au structures are put into an I_2/KI etching bath for 15 min. After the Au layer is completely removed, the PMMA/nanosheet is transferred to a fresh water bath for rinsing.

With the new technique we can really avoid using hydrofluoric acid (HF) as an etching bath and handling it with extreme care. However, for releasing PMMA/nanosheet from Si_3N_4/Si substrate we have to use HF as an etching bath.

Now we have a PMMA/nanosheet composite swimming on the purified water surface.

Other substrates or devices, such as SiO_2/Si, Si_3N_4/SiO_2/Si, quarts, TEM grids, Si substrate with window-structured openings, PDMS stamp with metal electrodes, Au/Cr/SiO_2/Si in transistor structures, can be used as new substrates for the monolayer. By fishing out the PMMA/nanosheet with a new substrate and drying it carefully with cleanroom paper and gently blow drying with a small stream of nitrogen, the transferring process is accomplished. Baking the new sample on a hotplate at 90℃ for 2 min could also allow for a much better contact and an adhesion between monolayer and new substrate.

Removal of transfer medium

For dissolving PMMA, the sample is mounted on a suitable sample holder. If the monolayer is on a solid substrate, the sample is simply immersed into an acetone solution and then put into an ultrasonic bath for 10~15 min. Later on the sample is immersed into another acetone solvent and a methanol solvent for a short while, and blown dry in a stream of nitrogen.

If the monolayer is suspended on the substrate, removing of PMMA is done either by a home-made setup that obtains a smooth flowing of liquid or by CPD that avoids surface tension induced damage to the monolayer. The sample in the former setup is put in an empty glass vessel which is gradually and smoothly filled with acetone. The sample is immersed in acetone for 40~60 min, and then put in methanol by the same procedure, and lastly blown dry in a stream of nitrogen. By means of CPD (Tousimis Autosamdri-815B, Series B), the sample that has been mounted on a sample holder is carefully immersed into acetone that fills the chamber of CPD. After 60 min, the whole chamber is cooled down with liquid CO_2 and then liquid CO_2 is introduced into the chamber in a very fine stream to avoid turbulence. Liquid CO_2 is going to substitute acetone according to a predefined time (15 or 20 min). Finally the dryer heats and pressurize CO_2 to its critical point and gas CO_2 bleeds off to leave the monolayer dry.

2.2.4 Preparation of PDMS stamps

Polydimethylsiloxan (PDMS) is a silicon-based organic polymer which is widely used in microchannel systems, medical devices and flexible organic electronic devices. For preparation of PDMS, 10 parts of prepolymer and 1 part of curing agent by weight ratio are put in a large petri dish and mixed uniformly with a glass rod for a couple of minutes until the entire mixture is full of bubbles. Then the mixture is placed in a vacuum oven to be degassed for 15 min. Afterwards the mixture is poured into another petri dish with molds which are lying flat on the bottom, such as a pressure cell or Si substrate. In order to avoid bubbles, the new petri dish is degassed in the vacuum oven again for 2 min. The petri dish is transferred to an oven and cured at 70℃ for 2h. The PDMS stamp is gently cut around the pattern with a razor blade and removed carefully from the petri dish and also separated from the mold if necessary.

Chapter 3

Bulge Test and AFM Point Deflection Method

3.1 Introduction

Bulge testing is one of the most important techniques for the mechanical characterization of freestanding thin films. It was first introduced by Beams in 1959 [49]. In this technique, a membrane is clamped over an orifice with circular or rectangular geometries. A controlled pressure is uniformly applied to the film through the orifice and the corresponding deflection of the membrane is measured. The mechanical properties, e.g. Young's modulus and residual stress, can be determined from the pressure-deflection relationship. The advantages of this technique are that it can measure intrinsic membrane properties without any substrate effect, microstructures of the membranes under load or unload and could be observed and investigated to have more understanding of mechanism.

In the past, sample preparation was very crucial to the results, because the results are quite sensitive to the dimension of membranes. With the development of micromachining techniques and improvements in theoretical analysis, many preparation problems have been already overcome and the bulge test has been more and more accurately understood. The initial states of films, such as residual stress, wrinkling, initial height, will have an influence on the pressure-deflection behaviors of thin films. Residual stress is an important parameter in device fabrication and affects performance of those devices. Failure to consider the initial height of the membrane will cause an apparent nonlinear elastic behavior [50]. The effects of bending stiffness were investigated by Vlassak [51], and he found that a bending momentum was only significant in the region close to the edge of the membranes.

Until now, the deflection of a membrane was monitored by an optical microscope either by viewing the membrane from the side [52] or by using a laser interferometer [53]. Both approaches have a rather low resolution in the range of hundreds of

nanometers to micrometers. The atomic force microscope enables the recording of the sample topography with nanometer resolution and is used as an indenter to perform indentation on freestanding membranes with low stiffness [54] as well as on graphene monolayers [55]. The combination of a bulge test with an AFM has been reported where the curvature of the membrane was determined by AFM [56], while deflection was measured with a laser autofocus displacement sensor.

In our work, the mechanical characterization of carbon nanosheets has been carried out by means of an in-situ bulge test in an AFM, where the AFM is used to record the deflection of the membrane's centre either by dynamically scanning a bulged membrane (Line Scanning Method) or by statically approaching the center of the membrane and measuring the deflection with a sensor built in the piezotube of the AFM (Central Point Method). The technique also allows us to determine the creep deformation and the ultimate tensile strength of carbon nanosheets.

3.2 Bulge test theory

Beams [49] and his coworkers derived a simple model to describe the stress and strain in the film. The model featured a circular bulged membrane with spherical cap geometry. From such an assumption, different equations can be derived for thin membranes with different initial conditions. In the following section, the models of bulge test will be presented in a detailed way.

3.2.1 Spherical membrane equations

A bulged circular membrane is schematically shown in Fig. 10, where P is the applied pressure, σ is the stress of the membrane, t is the membrane thickness, a is the radius of the membrane and R is the corresponding bulge radius of its curvature, which is the same in both radial and circumferential directions. In Beam's equation, the relationship between pressure P and stress σ is assumed to be

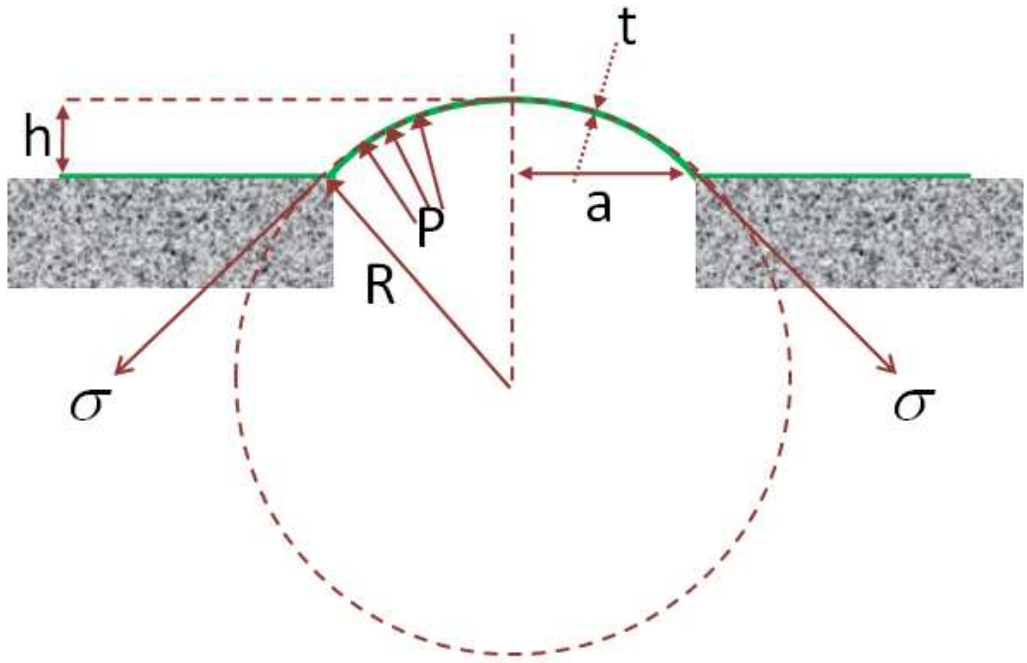

Fig. 10 Schematic diagram of a spherical cap geometry used to calculate the stress and the strain in a bulge test

$$P = \frac{4t\sigma}{a^2}h \tag{11}$$

The stress σ in the membrane is a sum of the stretching stress and the residual stress.

$$\sigma = \frac{E}{1-\nu}\varepsilon + \sigma_0 \tag{12}$$

where ε is the average strain of the membrane, E is Young's modulus, ν is in-plane Poisson's ratio, and σ_0 is residual stress.

The stress σ can be derived from the condition of the force equilibrium, resulting in the standard formula for stress in a thin-walled spherical pressure vessel:

$$\pi R^2 P = 2\pi R t\sigma \tag{13}$$

$$\sigma = \frac{PR}{2t} \tag{14}$$

To apply this to the bulge test, it is rewritten in terms of the deflection height of the bulged film in the case where the bulge height, h, is much less than the membrane radius, a. The bulge radius of curvature, R, can be written as:

$$R = \frac{a^2 + h^2}{2h} \approx \frac{a^2}{2h} \tag{15}$$

The strain in the membrane can be similarly derived using geometry with the assumption that deflection h is much more small than a. The strain is defined as the change in arclength divided by the original arclength with the following result:

$$\varepsilon = \frac{\Delta l}{l} = \frac{R\theta - a}{a} = \frac{2h^2}{3a^2} \tag{16}$$

By substituting Eq. 12 and Eq. 16 into Eq. 11, the final form of Beam's equation is written as:

$$P = c_1 \frac{\sigma_0 t}{a^2} h + c_2 \frac{Yt}{a^3} h^3 \tag{17}$$

where c_2=8/3 and c_1=4, Y, the biaxial modulus, is defined as $\frac{E}{1-\nu}$.

3.2.2 Energy minimization method

One common approach to model the deflection behavior of thin membranes is the energy minimization method. In this method the shape of the deformed membrane is assumed in such a way that the strain energy of the whole system is minimized.

Circular membranes

The solution for circular membranes can be derived by defining the shape of the deformed membrane. The first solution was derived by assuming that the shape of the deformed membrane as that of a clamped circular plate [57],

$$w = h\left[1 - \left(\frac{r}{a}\right)^2\right]^2 \tag{18}$$

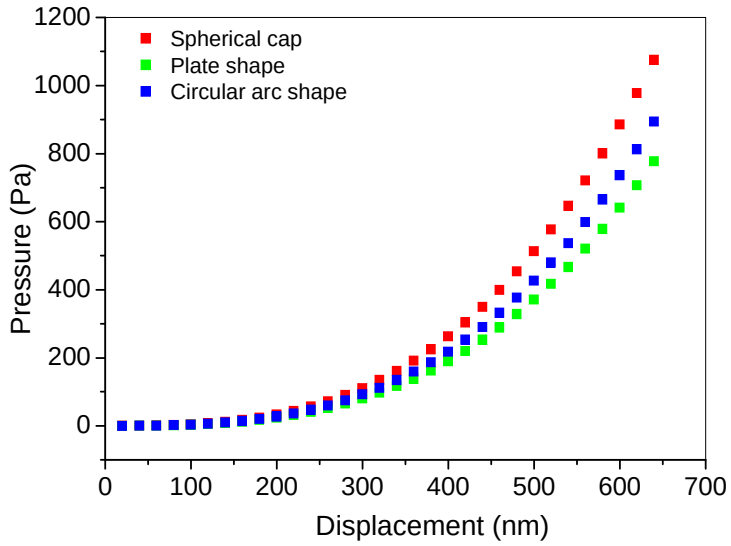

Fig. 11 Comparison of pressure-displacement relationship from three models.

where w is the vertical deflection of the membrane and h is the deflection at $r=0$, which means the bulge height. This shape function is valid for very small deflections. One can obtain the following pressure-displacement relation by means of energy minimization method.

$$P=\frac{Et}{(1-\nu)}\left(\frac{7-\nu}{3a^4}\right)h^3+\frac{4\sigma_0 t}{a^2}h \tag{19}$$

The second solution was derived by Lin [58]. The shape was defined as a circular arc assuming that the bulge height is much less than the film radius:

$$w=h\left[1-\left(\frac{r}{a}\right)^2\right] \tag{20}$$

In the same way, the corresponding pressure-displacement equation is expressed as

$$P=\frac{16Et}{3a^4(1-\nu^2)}0.488h^3+\frac{16Et^3}{3a^4(1-\nu^2)}h \tag{21}$$

The pressure-displacement curves corresponding to the three models are shown in fig. 11. It was found that both energy minimization methods predicted more compliant membrane behaviors than the spherical membrane equation. Moreover, the two energy minimization methods showed a different dependence on the Poisson's ratio.

Square and rectangular membrane equations

Vlassak and Nix [59] have developed a model based on an energy minimization method for analysis of the deflection of both square and rectangular models. The potential energy of the total system can be written as,

$$V = \frac{Et}{2(1-\nu^2)} \iint \left(\varepsilon_x{}^2 + \varepsilon_y{}^2 + 2\nu\varepsilon_x\varepsilon_y + \frac{1}{2}(1-\nu^2)\gamma_{xy} \right) dxdy - \iint pwdxdy \qquad (22)$$

where ε_x and ε_y are the strain components in the x-direction and in the y-direction, E, t and ν are Young's modulus, thickness and Poisson's ratio of the membrane, respectively, P is the pressure applied to the membrane.

Minimization of the above equation with respect to the undetermined parameters leads to a set of three simultaneous nonlinear equations. Considering the residual stress in the membrane, the pressure-deflection relationship of a stressed membrane is given by

$$P = c_1 \frac{\sigma_0 t}{a^2} h + c_2 \frac{Et}{a^4(1-\nu)} h^3 \qquad (23)$$

where both parameters c_1 and c_2 are functions of aspect ratio and Poisson's ratio and the values are given in table 1 for different membrane shapes.

Table 1 Values of the c_1 and c_2 parameters for different membrane shapes

	Square $(b/a = 1)$	**Rectangular** $(2 > b/a > 1)$	**Long rectangular** $(b/a \geq 4)$
c_1	3.393	$3.393 > c_1 > 2$	2
c_2	$(0.800 + 0.062\nu)^{-3}$	$1.004 > c_2 > 0.827$	$\left(\frac{6}{8}(1+\nu)\right)^{-3}$

3.3 Line scanning method

It is well known that AFM is used to image specimens by mechanically “feeling” the surface with a sharp tip that is mounted on a cantilever. The lateral resolution is determined by the radius of the tip. The sharper the tip, the higher resolution it has, because the interaction area between tip and specimen is a fraction of the tip radius. The radius of an AFM probe tip is at best a few nanometers and this limiting factor determined the ultimate lateral resolution of an AFM operated at ambient conditions. However, an AFM operated in an ultrahigh vacuum at very low temperature, with a carbon monoxide molecule on the tip, can achieve an atomic-scale image of the pentacene molecule [60].

With the line scanning method in a bulge test, the membrane is simply scanned with the AFM. The deflection of the membrane is recorded from the topographic AFM image. The scanning range of an AFM depends on the scanner, either sample scanner or tip scanner. It is the scanning range of an AFM which determines the maximum membrane to be measured in a bulge test. The maximum membrane size is thus limited to 100 μm and the maximum deflection is limited to 8 μm.

3.3.1 Experimental description

The pressure cell is made from a hollow steel cylinder with two sideway openings for introducing and measuring the gas pressure, and one circular opening at the centre of the topside for applying pressure to the membrane, as shown in fig. 12a. In order to establish a gas-tight seal between sample and pressure cell, a layer of polydimethylsiloxane (PDMS) with a thickness of 2 mm was prepared on top of the pressure cell. In order to achieve a uniform level of PDMS layer while still leaving the circular hole open, two supports for the sideways and one screw with a needle-like terminate for the central hole are used to adjust the level of the pressure cell when it is kept upside down during the preparation of PDMS layer.

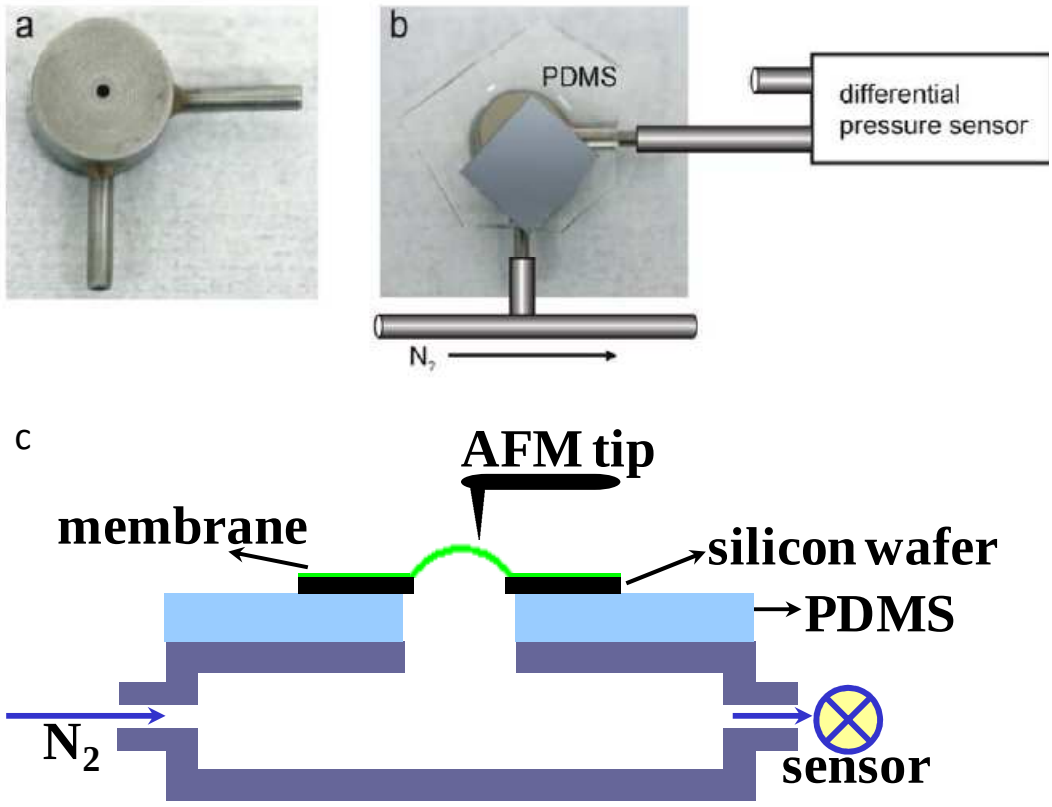

Fig. 12 (a) A photograph of the pressure cell; (b) The schematic diagram of an experimental set up and the photograph of the pressure cell with one sample mounted; (c) The schematic diagram of the bulge test.

Pressurized nitrogen is provided by a gas cylinder (Linde Gas). The pressure is controlled by a regulator and a loading valve on the gas inlet, as well as by a tube regulator on the gas outlet. The differential pressure is measured with a pressure transducer (HCX001D6V, Sensortechnics). It is connected with the pressure cell as schematically shown in fig. 12b. The pressure range is from 0 to 1 bar and the output signal is voltage. The output voltage is measured with a digital multimeter (VC840, Voltcraft). The conversion from 1 mV voltage to pressure is 25 Pascal.

In line scanning method, the deflection of the membrane is measured with an AFM (NT-MDT NTEGRA) in contact mode by employing a platinum-coated silicon cantilever (force constant: 0.1 N/m). The platinum coating can reduce the adhesion between the tip and the suspended monolayers. Scans for data acquisition were

conducted in constant height mode with a scan-speed of 5~8 μm/s and a very low feedback gain of 0.01~0.02, while scans for imaging were conducted in constant force mode with a scan-speed of 15 μm /s and a feedback gain of 0.35. The latter setting with a faster scanning period yields an improved image quality of the whole membrane. It is not as gentle and the probability of rupture is enhanced.

The sensheight signal in the AFM instrument was calibrated by using grating sets (Calibration grating set TGS1, NT-MDT) and deflection was acquired from the Sensheight image. For the substrates usually have a slight obliquity as a result of the PDMS layer underneath, it leads to a higher lateral force as well as a higher vertical force on the membrane when the AFM probe tip is scanning upward. To avoid the error from the height difference between the forward and backward images, either forward or backward images or their mean values are used for data acquisition. The correction due to point load from the AFM probe tip will be discussed later.

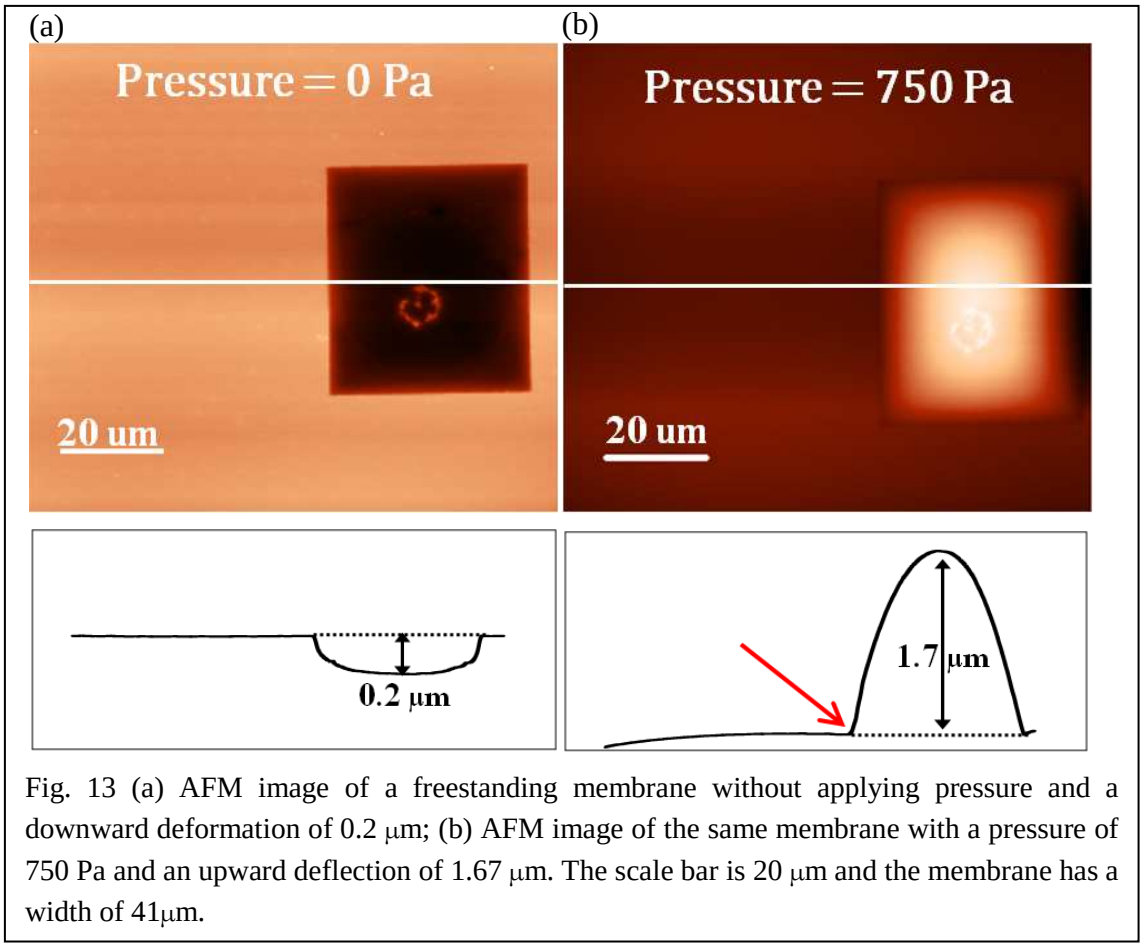

Fig. 13 (a) AFM image of a freestanding membrane without applying pressure and a downward deformation of 0.2 μm; (b) AFM image of the same membrane with a pressure of 750 Pa and an upward deflection of 1.67 μm. The scale bar is 20 μm and the membrane has a width of 41μm.

3.3.2 Results and discussions

Fig. 13a shows the AFM image of a membrane without applying gas pressure, whereas a downward step height of ~200 nm was observed which is caused by the point load of the AFM probe tip. The step height can be decreased by reducing the force of the AFM tip. Fig. 13b shows the AFM image of the same membrane with an applied pressure of ~750 Pa, an upward deflection of 1670 nm was measured at the center of the membrane. It was found that the monolayer adhered strongly to the Si substrate by Van der Waals interaction. During the whole loading and unloading process, no lifting events along the border are observed.

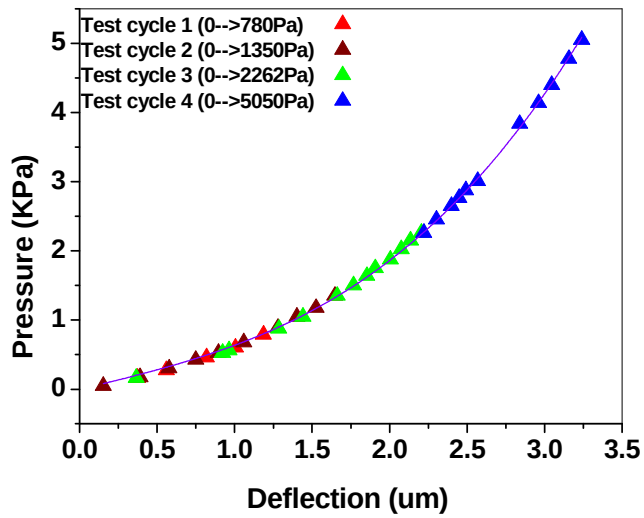

Fig. 14 Pressure deflection relationship of a carbon nanosheet with four test cycles, the maximum strain is 2.08 % at a pressure of 5050 Pa.

Fig. 14 exhibits a typical nonlinear pressure-deflection relationship of carbon nanosheets by means of a line scanning method. Four successive loading cycles ending at elevated pressures are carried out and the corresponding experimental data is presented with different colors in the plot and the repeatability of measurements is thereby demonstrated. The size of this membrane is $36.6\times73.2\,\mu m$ and the maximum strain at the highest pressure is 2.08 %. After corrections relating to the point load produced by the AFM tip, Young's modulus and residual stress can be determined from the fitting curve.

3.4 Central point method

3.4.1 Introduction

In the last section the line scanning method was utilized to determine the deflection of the membranes. However, this method has some obvious disadvantages. Firstly, the membranes can easily become ruptured during the scanning process due to the lateral force of the AFM tip, especially for the transferred nanosheets with even a tiny amount of residual PMMA on the surface. Secondly, the method is very time-consuming due to the scanning at a low speed and the subsequent data analysis. Thirdly, the measurement cost is high, once a membrane is ruptured and the AFM probe would get contaminated and would be unusable. That is why it is necessary to find a new way to perform a bulge test more productively and conveniently.

3.4.2 Experimental description

In order to minimize the failure in measurements, a central point detection method was utilized in the mechanical characterization of ultrathin membranes in bulge tests. Instead of line scanning, the AFM tip was positioned simply on top of the membrane's center to detect the deflection of the membrane.

The determination of the center of a membrane was done by a well-controlled positioning system of the AFM instrument that has a minimum movement of 0.1 um. The membrane was positioned very close to the AFM tip with the assistance of an optical microscope. As shown by the scheme in fig. 15, the sample is firstly moved with larger steps (e.g. 5 um) using the sample stage controlled by the positioning system. The height variations between steps were monitored with the AFM tip. There will be a detectable variance between the steps on a tilted substrate (red dots on the substrate) and the step from substrate to a suspended membrane (two red dots in the black frame). After the rough position of the membrane's left side was determined, smaller steps (e.g. 0.5 um) were taken to find out the transition location more precisely, as shown in the lower-left enlarged frame. After the transition position from the substrate to the membrane was determined, the sample will be moved to a distance

equal to half the width of that membrane, which leads to the central position in the horizontal direction. The same procedures can be repeated to determine the transition position from the substrate to the membrane on the top or bottom side, afterwards the sample is then to be moved a distance equal to half the length of the membrane, which leads to the central position in the vertical direction. The dimensions of the membranes are measured with an optical microscope before all other measurements.

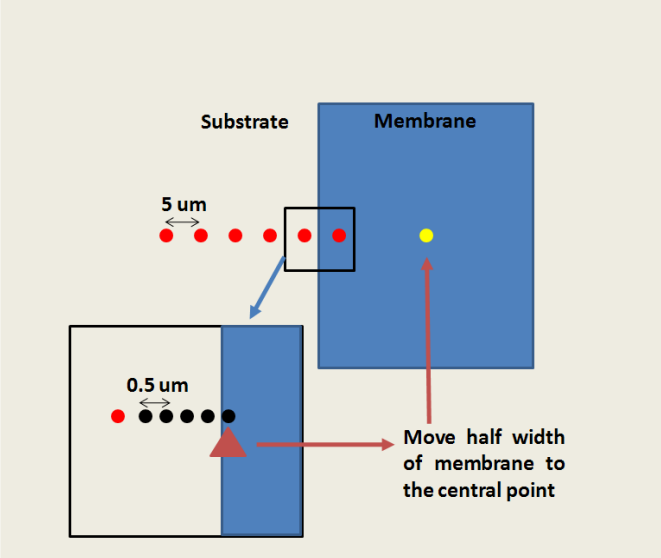

Fig. 15 Scheme of central point determination: Dots represent the positions of the AFM tip. The height variations of larger steps (red dots) on a substrate are different from that of from a substrate to a suspended membrane. An enlarged frame describes smaller steps to detect the sides of the membrane. Move half the width of the membrane to the central position in the horizontal direction. The same procedures can be done to move the membrane to the central position in the vertical direction. The central point is shown in a yellow dot.

Once the AFM tip is positioned above the centre of the membrane, by switching on the feedback gain, the piezotube scanner will move up the membrane up to a contact with the AFM tip. After the reading is recorded, the scanner will move down the membrane by switching off the feedback gain. Different pressures give rise to resultant readings from the scanner's movements. We need a reference on the substrate to determine the true deflection of that membrane.

As shown schematically in fig. 16, the substrate first moves up to get into a contact with the AFM tip and the distance is recorded as d_0. In the same way, the central point of a membrane can be moved up to the tip with a distance d_1. The deflection of that membrane δ is computed as $d_0 - d_1$. The red and green lines represent the deflection of the membrane due to a lower and a higher pressure, respectively.

In reality, the substrate has an inclination angle θ which can be used to figure out the initial height of the central point without applying pressure. Considering the elevation of the substrate which resulted from the deformation of PDMS beneath the sample and the thermal drift on the AFM itself as well, several reference points on the substrate were taken in order to eliminate these effects, as shown in fig. 16c. The initial height of the central point O is determined as,

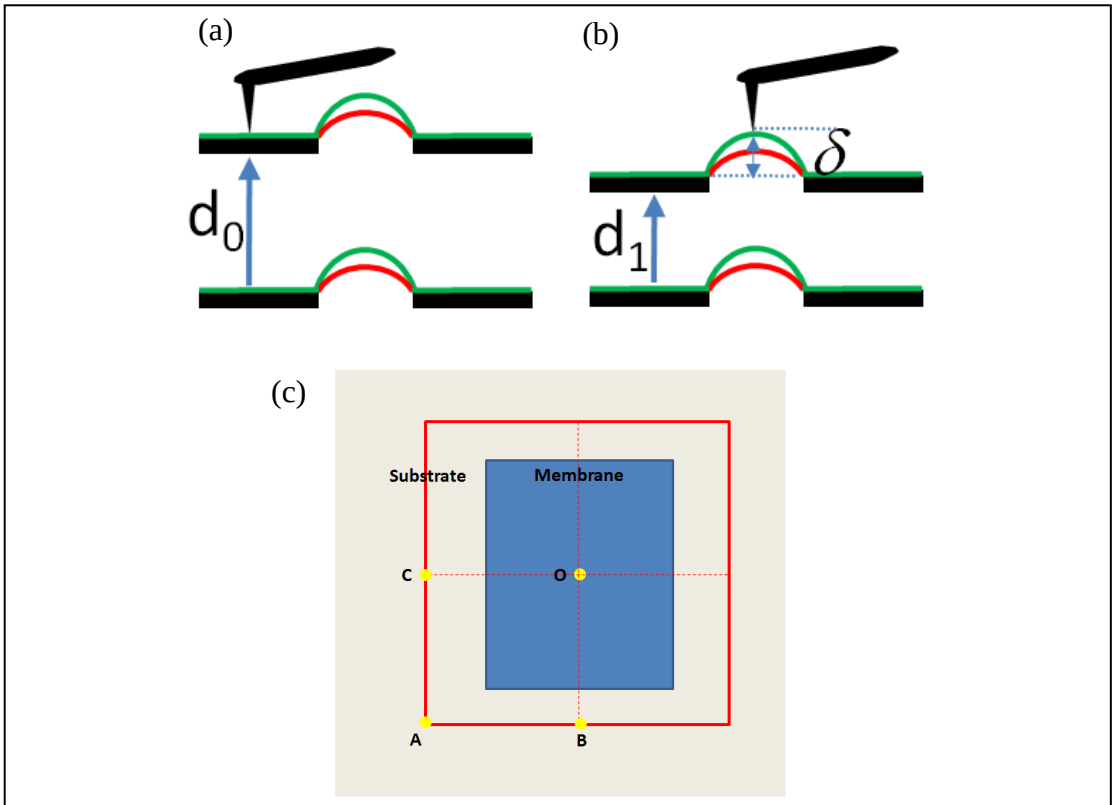

Fig. 16 Schematic diagram of the central point method in a bulge test: (a) The Piezotube moves the substrate up to contact with an AFM tip. (b) The Piezotube moves the membrane up to contact with the AFM tip. (c) The central point "O" and three other reference points "A", "B" and "C" on the substrate are presented as yellow dots and the scanning frame is shown as a red frame.

$$h_O = h_C + h_B - h_A \tag{24}$$

Once the initial height was known, only one reference point (e.g. point C) will be measured as a reference for each measurement, assuming the variation between the other two references (e.g. point A & B) keeps constant during the measurements.

3.4.3 Calibration of sensor height signal

To examine the validity of the central point method in comparison with the line scanning method, pressure versus deflection curves of one membrane were obtained from both methods. All the experimental data were presented in fig. 17a. It was observed that the deflection signals in the line scanning method are much higher than that in the central point method at the same applied gas pressure. For confirmation, we employed both the contact mode and the tapping mode and the different cantilevers have been used as well. This indicates that the signal readings from oscillograph panel in the software are not yet calibrated. The calibration grating set TGS1 (NT-MDT) contains three grating TGZ1 (21.5±1 nm), TGZ2 (113.5±2 nm), TGZ3 (540±3 nm) with different step heights. The height signal obtained from the oscillograph is exactly two times smaller than that from Sensheight image. All the deflection data need to be corrected by multiplying by a factor of 2. After correcting the data, both methods are in good agreement, as it was demonstrated in fig. 17b.

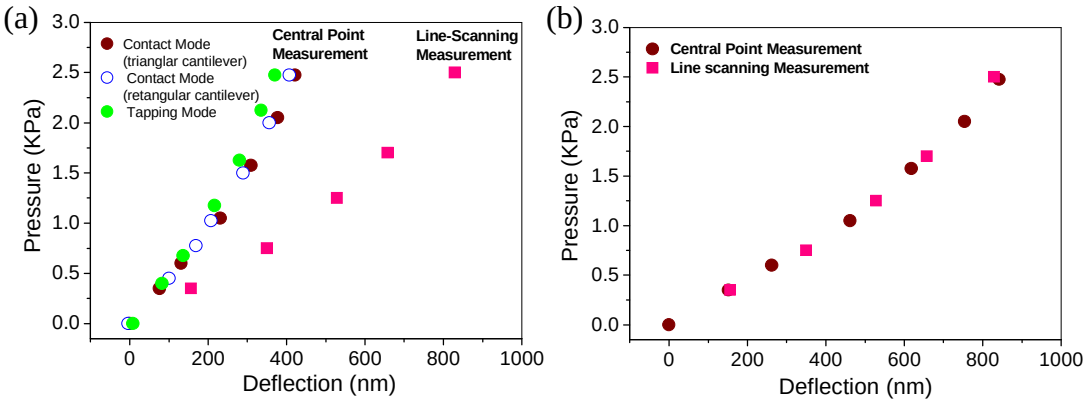

Fig. 17 Pressure vs. deflection curves determined with the central point method in comparison with the line scanning method: (a) Before correcting the data, a large deviation was found. (b) After correcting the data, both methods are in agreement.

3.4.4 Deflection correction

The deflection setpoint can be preset in order to adjust the force which the tip applies to the nanosheet. This force leads to an indentation as a step between the silicon frame and the nanosheet. A series of setpoint settings with the resultant step heights is presented in fig. 18. The linear dependence shows a decreasing step height as the result of a reducing deflection setpoint. The step height tends towards vanishing at a zero setpoint, which corresponds to the deflection value of an unperturbed cantilever, e.g. far away from the sample. In other words the cantilever is not bent at the deflection value of zero and therefore it does not apply any force to the nanosheet at this deflection value.

In the central point method, the measurements were usually performed with a setpoint slightly higher than zero which leads to a certain step height. This quantity was measured on nonpressurized membranes and it was employed to correct the measured deflection of the nanosheets as shown in the following diagram. The deflection of the membrane h is given by the AFM height signal h_{AFM} and the step height by

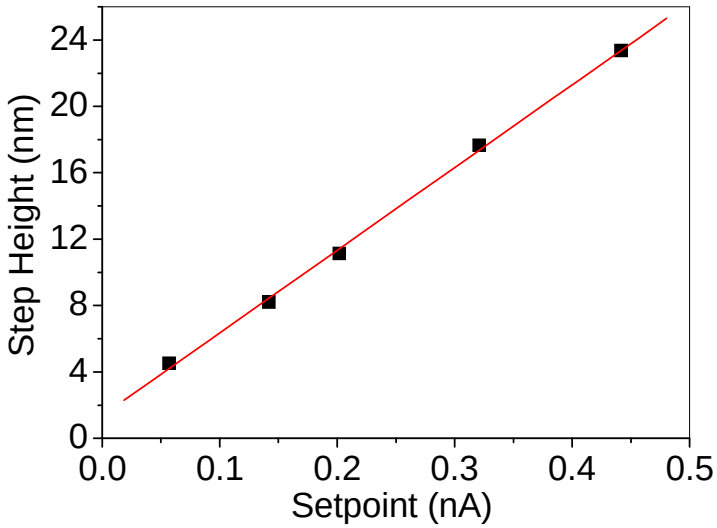

Fig. 18 Step heights between a membrane and a silicon frame as a function of the setpoint determined in an AFM.

$$h_{corrected} = h_{measured} + \delta \tag{25}$$

If we consider the main energy contributions to such a system, the energy from the AFM tip is balanced by the lateral tension of the membrane, the bending stiffness at the boundary, the curvature energy around the tip, the adhesion energy between the AFM tip and the membrane. The energy contributed by the bending stiffness is much smaller than that from the tension and can thus be neglected. A small tip radius in comparison to the membrane dimension allows us to neglect both the curvature energy and the adhesion energy related to the tip. To simplify the calculation, the tension energy (or the stretch energy) of the membrane is assumed to be the only contribution. Without applying a pressure, the membrane has a prestress that dominates the tension energy of the membrane. After applying a pressure, the indentation depth δ can be obtained from total stress in a bulged membrane, in comparison to the step height δ_0 from the prestress of a non-pressurized membrane,

$$\delta = \delta_0 \frac{\sigma_0}{\sigma_0 + \sigma} = \delta_0 \frac{\sigma_0}{\sigma_0 + \frac{2}{3}\frac{E}{1\text{-}\nu}\frac{h_c^3}{a^2}} \tag{26}$$

Note that one approximation of this correction scheme assumes a constant step height, i.e. $\delta = \delta_0$, this simplification results in an underestimation of Young's modulus and an overestimation of the residual stress. Nevertheless, all the data could be treated with the full correction scheme. In order to avoid thermal drift from the AFM cantilever and to obtain constant force during the whole measurements, the setpoint is always set at the same value as that of the unperturbed cantilever and the feedback gain signal is also set to a constant, e.g. 0.25.

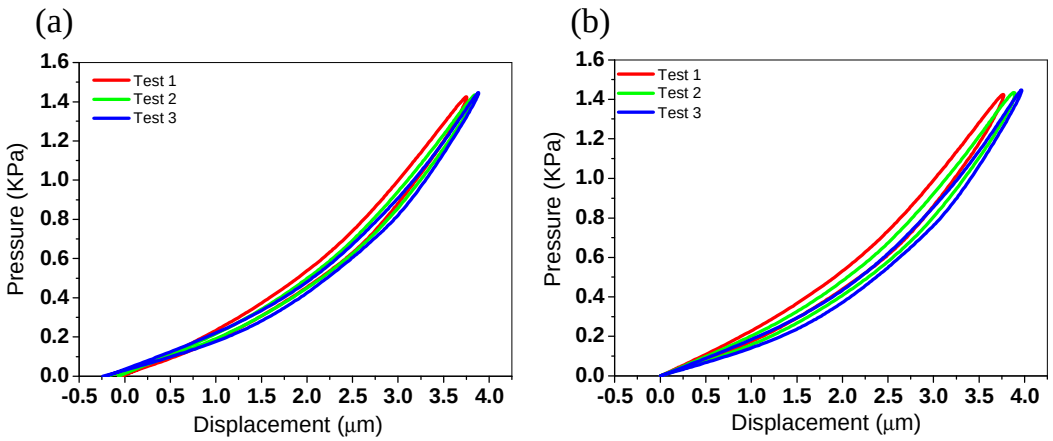

Fig. 19 (a) Pressure-displacement curves of three loading and unloading tests before the deflection correction; (b) Pressure-displacement relationship after the deflection correction.

Table 2 Young's modulus and residual stress before and after deflection correction

	1st Test Cycle		2nd Test Cycle		3rd Test Cycle	
	Load	Unload	Load	Unload	Load	Unload
Young's Modulus Not-Corrected(GPa)	8.62	11.0	9.32	11.0	9.16	10.5
Young's Modulus Corrected(GPa)	**8.86**	**11.2**	**9.55**	**11.2**	**9.37**	**10.7**
Residual Stress Not-Corrected(GPa)	49.4	32.1	43.9	30.5	42.9	32.1
Residual Stress Corrected(GPa)	**46.9**	**28.8**	**41.1**	**27.2**	**40.2**	**28.6**

Fig. 19a shows an example of the pressure-displacement curves of three successive loading and unloading measurements before deflection correction. It can obviously be observed that all the displacements at zero pressure became zero after the deflection correction, as presented in fig. 19b. Table 2 presents a detailed comparison of Young's modulus and residual stress before and after the deflection correction. A small increase in Young's modulus and a decrease in the residual stress were found. The detailed determination will be explained in the next chapter.

3.4.5 Uncertainty analysis

The precision of the bulge test describes how close a number of measurements agree with each other, which is limited by random errors. The accuracy of the bulge test describes how close the measured values are to the true value, which is limited by systematic errors.

Estimation of the random error in a bulge test, Eq. 23 can be divided into five parts.

$$E \propto \left(\frac{P}{h^3}\right) \times a^4 \times c_2 \times \frac{1}{t} \times (1-\nu) \tag{27}$$

The first term $\frac{P}{h^3}$ is determined from the fitting curve for the pressure-deflection relationships. In this term, the pressure was measured with a pressure transducer and the output voltage was measured with a digital multimeter. The random error in the pressure measurement is from both the transducer and the multimeter. The displacement was recorded from a Sensheight signal in the AFM which has been already calibrated with the standard calibration gratings. The random error of the term $\frac{P}{h^3}$ was estimated as 1 %.

The second term a^4 describes the half width of a membrane which was measured with an optical microscope and further examined with a SEM. Because Young's modulus is proportional to the fourth power of width, a larger random error of approximately 6 % is estimated for this term.

The third term is the parameter $c_2 = \frac{1}{g(\nu, b/a)^3}$ which was taken from a chart in the literature [59]. The random error is mainly due to measuring and reading. A 3 % random error is thus estimated. The thickness and the Poisson's ratio are constants which do not contribute to a random error. In all we achieve approximately 10 % random errors in the bulge test, as shown in Eq. 28.

Table 3 Uncertainty analysis of bulge test

E Young's Modulus	Error Components	Error Descriptions	Error Estimation
$\frac{P}{h^3}$	$\left\|\frac{\Delta c_1}{c_1}\right\|$	Standard deviation of curve fitting	1 %
a	$4\left\|\frac{\Delta a}{a}\right\|$	Measurements errors	6 %
$g\left(\nu,\frac{b}{a}\right)$	$3\left\|\frac{\Delta g}{g}\right\|$	Measurements errors	3 %
t	$\left\|\frac{\Delta t}{t}\right\|$	Constant for all measurements	0 %
$(1-\nu)$	$\left\|\frac{\Delta(1-\nu)}{1-\nu}\right\|$	Constant for all measurements	0 %
Summation			10 %

$$\frac{\Delta E}{E}=\left|\frac{\Delta(\frac{P}{h^3})}{\frac{P}{h^3}}\right|+4\left|\frac{\Delta a}{a}\right|+3\left|\frac{\Delta g}{g}\right|+\left|\frac{\Delta t}{t}\right|+\left|\frac{\Delta(1-\nu)}{1-\nu}\right| \tag{28}$$

To estimate the systematic error in a bulge test, the accuracy of values (e.g. thickness, Poisson's ratio and constant $g(\nu,b/a)$), the calibration of the measurements (e.g. pressure transducer, AFM, SEM) and the reliability of theoretical calculations have to be taken into account. The errors from the AFM, SEM and the pressure transducer sum up to 15 %. The accuracy of the constant $g(\nu,b/a)$ gives a contribution to Young's modulus uncertainty of 9 %. The monolayer thickness uncertainty was estimated to be 15 %. Thus these error contributions add up to about 40 %.

3.5 AFM point deflection method

Apart from the bulge test, the point deflection method has been another technique for the mechanical characterization of freestanding thin films with very low stiffness [61]. Unlike the uniform pressure on thin films in a bulge test, a spherical nanoindenter or an AFM tip is utilized to apply a small concentrated transverse point load at the center of a thin film. Young's modulus and residual stress are determined from the corresponding force displacement relationships.

Theoretically, there are different regimes of behavior for thin films subjected to point loads, such as plate, linear membrane and nonlinear membrane. Focused on literature results for point loads, Komaragiri and his co-workers provide a comprehensive theoretical framework that describes the effects of prestretch, film thickness and loads [62]. Experimentally, freestanding circular elastomer films were measured using spherical indenters. It demonstrates that soft materials and ultra-thin films with load-deflection stiffness on the order of 0.01 N/m can be characterized with such an experiment and theoretical framework [63]. A high-throughput mechanical characterization (HTMECH) apparatus was constructed for polymer films in 10~1000 μm thickness [64] and it allows measurements from near-static to dynamic deformation and characterization of the viscoelasticity. The point deflection method using the AFM tip as an indenter has attracted researchers to evaluate the mechanical response of nanoscale freestanding membranes to indentation. The graphene monolayer has also been investigated by the point deflection method in an AFM (nanoindentation in an AFM) [65].

In this section, we will introduce the point deflection method in an AFM for the mechanical characterization. The cantilever calibration and some results will be presented and discussed. The boundary constraint and other limitations of this method will also be discussed.

3.5.1 Experimental description

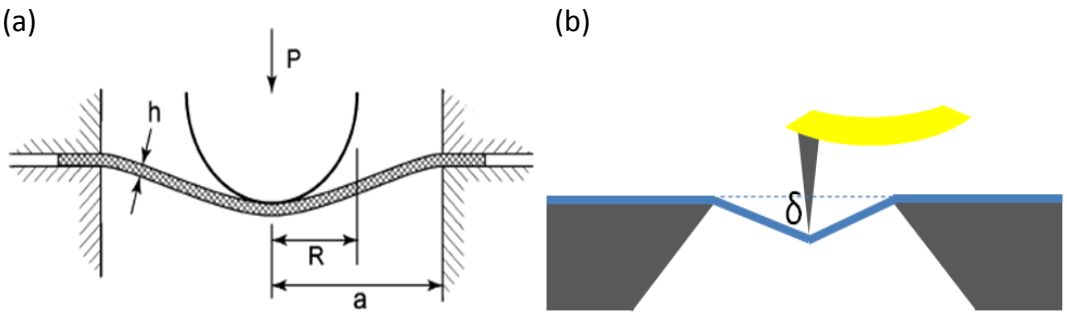

Fig. 20 (a) A schematic diagram of the point deflection method using a nanoindenter for a freestanding thin film [63]. (b) A schematic diagram of the point deflection method using an AFM tip as an indenter for a carbon nanosheet.

The point deflection method using a nanoindenter is schematically shown in fig. 20a. A spherical indenter is usually utilized to apply a load on the freestanding membrane [63]. The indenter is driven by a load cell which is mounted on a linear screw-driven positioning stage. The deflection of thin films could be determined in various ways, for example by light interferometer and strain stage on the film itself. One can also measure the displacement directly using an optical encoder built into the positioning stage.

The point deflection method using an AFM tip as an indenter is schematically shown in fig. 20b. First of all, the central point of a freestanding membrane can be determined according to the method mentioned in the last section. For polymer thin membranes with thicknesses bigger than 20 nm, the whole membrane can be imaged using the AFM and the central positions are thus determined more precisely. A load is applied by an AFM tip with the radius of 20~50 nm. The maximum load, i.e. the maximum bending of the cantilever, is defined by presetting a DFL signal for the quadrant photodiode. The deflection of the cantilever is recorded from a force-distance curve. The force constant of the cantilever has to be calibrated in order to subtract the cantilever stiffness from the force-distance curves.

3.5.2 Calibration of cantilevers

The spring constant of a cantilever has to be calibrated in order to calculate the exact force applied through this cantilever. For a rectangular cantilever, Sader's method [66] is believed to be very practical and accurate. The mechanism of calibration is based on a shift in the resonant frequency of the cantilever from a vacuum to a fluid, whose density and viscosity are known,

$$\omega_{vac}=\omega_f\left(1+\frac{\pi\rho_f b}{4\rho_c h}\Gamma_r(\omega_f)\right)^{1/2} \tag{29}$$

where ρ_f is the density of the fluid, ρ_c the areal mass density, ω_{vac} the vacuum resonant frequency, ω_f the resonant frequency in fluid, Γ_r the real component of the hydrodynamic function Γ. The spring constant k is given by

$$k=0.1906\rho_f b^2 L Q_f \Gamma_i(\omega_f)\omega_f{}^2 \tag{30}$$

where b and L are dimensions of the cantilever, Q_f the quality factor, Γ_i the imaginary component of the hydrodynamic function Γ.

The dimensions of the cantilever can be determined with an optical microscope. Fig. 21a shows an optical microscopy of an AFM cantilever that has a length of 222.8 μm

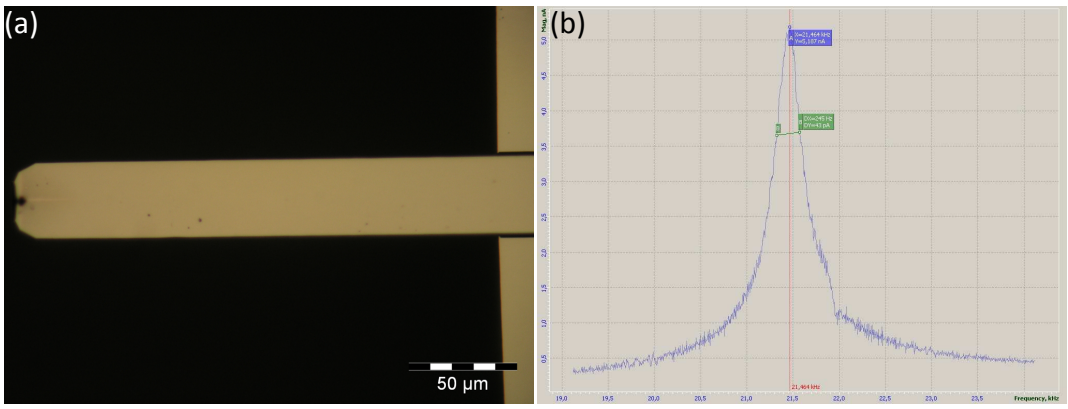

Fig. 21 (a) The optical microscopic image of an AFM cantilever. (b) The amplitude of the oscillation of the cantilever as a function of the excitation frequency with a resonance frequency of 21.434 KHz and a Q factor of 75.

and a width of 35 μm. The resonance frequency of the cantilever can be recorded by the AFM software. The Q factor was calculated from the graph of the resonance frequency peak. It is equal to the resonance frequency divided by full width of that peak at maximum magnitude multiplied by 0.707, which gives rise to half of the initial maximum energy in the resonator. As shown in fig. 21b, the cantilever has a resonant frequency of 21.434 KHz and a Q factor of 75. The force constant is therefore estimated to be 0.182 N/m.

Table 4 Cantilever's specific for calibration of spring constant

cantilever length (L)	Cantilever width (w)	Resonance frequency (ω_f)	Quality factor (Q_f)	Force constants (k)
222.8 μm	35.0 μm	21.434 KHz	75	0.182 N/m

3.5.3 Results and discussions

The point deflection method has been firstly used to check the membrane stiffness. Two different forces (7.25 nN and 21.75 nN) were applied and the corresponding deflections of the cantilever were recorded. The coupled stiffness S of the AFM cantilever in contact with the membrane (a NBPT nanosheet) is given by

$$\frac{1}{S}=\frac{1}{S_0}+\frac{1}{S_c} \tag{31}$$

where S_c is the AFM cantilever stiffness and S_0 is the membrane stiffness which can be computed from the equation.

Fig. 22 shows an example of the determined membrane stiffness as a function of the eccentricity ratio $2r/a$, where a is the diagonal dimension of the membrane and r is the distance from the membrane center to the position where the load has been applied, $2r/a=1$ corresponds to the corner of the membrane. It indicates that the measured stiffness is independent of the eccentricity ratio in the range of 0~0.5.

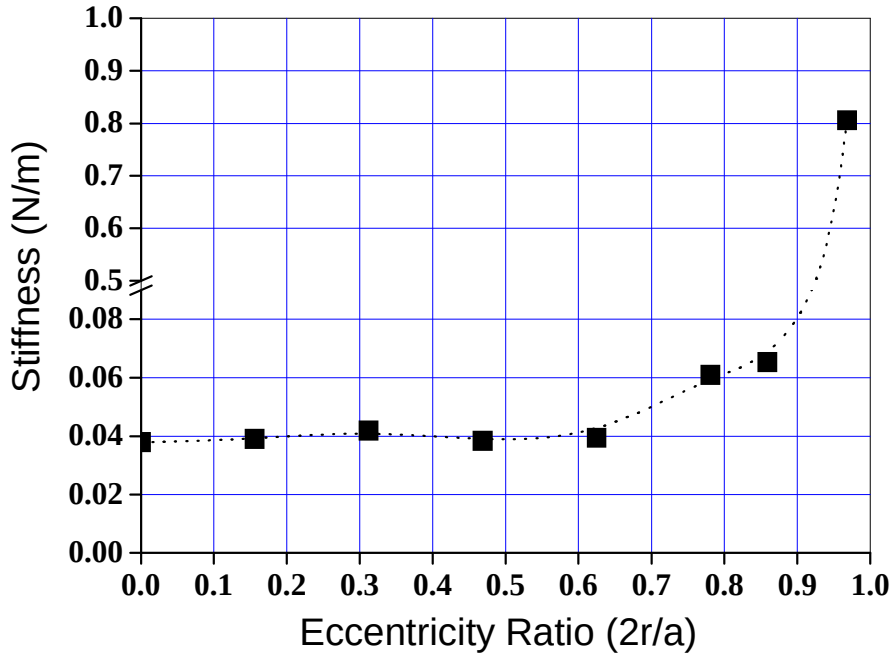

Fig. 22 Variation of the membrane stiffness S_0 as a function of the eccentricity ratio.

The point deflection method has been carried out on the freestanding PS/nanosheets bilayer membranes. The force distance curves that were applied on a silicon nitride substrate were taken as a reference, which is based on the assumption that once the AFM tip contacted the substrate the cantilever would undergo a simple bending without penetrating into the surface.

Fig. 23a exhibits a force-distance curve with respect to the AFM tip on the substrate and its linear behavior representing the stiffness of the AFM cantilever. The force curve with respect to a PS/nanosheets membrane is shown in fig. 23b, a nonlinear deformation was observed from the force curve. The displacement was recorded from the Z-piezo sensor and it contained both the displacement of the membrane and the bending of the cantilever. As discussed above, the cantilever's displacement has to be subtracted in order to obtain the pure load-indentation depth relationship. The displacement of the membrane is equal to the Z-piezo displacement minus that of the cantilever,

$$\delta_{membrane} = \delta_{piezo} - \delta_{cantilever} = \delta_{piezo} - F / k \tag{32}$$

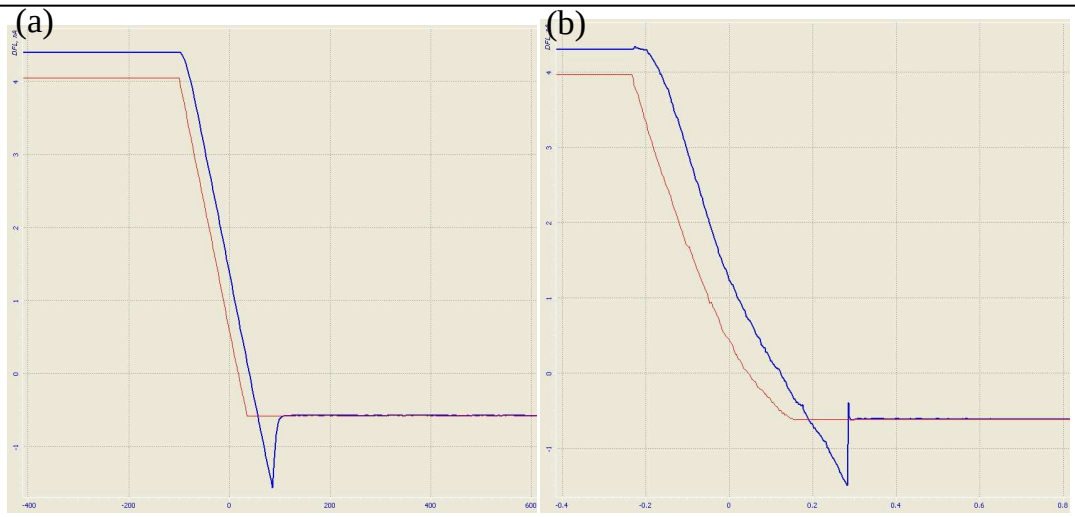

Fig. 23 (a) Force-distance curve with respect to an AFM tip on a substrate; (b) Force-distance curve with respect to an AFM tip on a freestanding polystyrene/nanosheet membrane. (red curve: snap in; blue curve: retract)

where F is the force applied with the AFM cantilever and k is the spring constant of the cantilever. In fig. 24, the lower red curve shows the load vs. indentation depth relationship derived from the original force curve and the upper green curve shows the relationship after subtracting the cantilever stiffness.

Both the carbon nanosheets and PS/nanosheets bilayer system have a much lower thickness (in the range of nanometers) compared with their dimensions (in the range of tens of micrometers). The classical plate theory which is based on the assumption

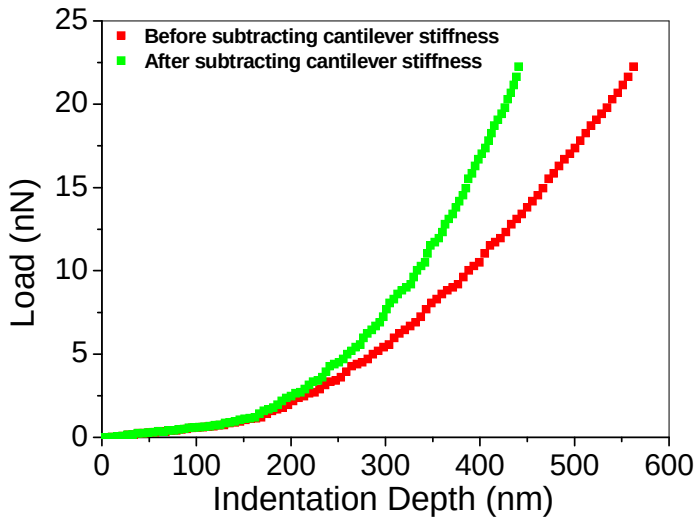

Fig. 24 Load vs indentation depth derived from the original force curve (red one) and load vs indentation depth after subtracting the cantilever stiffness (Green one).

that stretching in the plane of the film is negligible compared to the bending deformation is not suitable to interpret such systems. They are supposed to be in the linear membrane regime where prestress is greater than the bending stiffness, as well as the load is still small enough to balance the prestrain and to avoid a large deflection. In this regime, the relationship between force and deflection can be expressed as [67],

$$F=\pi\sigma_0\delta+\frac{Et}{a^2}f(\nu)\delta^3 \tag{33}$$

where F is the applied force, δ is the displacement at the central point, σ_0 is the prestress, $f(\nu)$ is a dimensionless constant. Young's modulus E can be derived from the cubic term in the equation.

Table 5 A comparison of the point deflection method and the bulge test

Method	PS2h_G1	PS2h_G2	PS2h_G3	PS2h_G5
Point Deflection Method	4.45 GPa	3.08 GPa	6.0 GPa	1.14 GPa
Bulge Test	2.05 GPa	n.a.	2.8 GPa	n.a.

A series of samples have been measured by using both the point deflection method and the bulge test. The results were shown in table 5. Young's modulus determined from the point deflection method exhibits a bigger scattering in comparison with that of a bulge test. It indicates that the point deflection method has some limitations: (1) the deformation in the point deflection method is rather small and the elastic response is largely influenced by the prestress; (2) the tip radius is not quantitatively determined and the uncertainty is thus much bigger; (3) the membrane's stiffness is not sensitive to the central position; (4) the equation is derived for circular membranes, which needs to be further modified for square and rectangular membranes.

Chapter 4

Mechanical Properties of Carbon Nanosheets

4.1 Adhesion and corrugation of a carbon nanosheet on a substrate

4.1.1 Introduction

Interfacial adhesion describes the adhesion in which interfaces between phases or components are maintained by intermolecular forces, chain entanglements or both, across the interfaces [68]. Interfacial adhesion plays an important role in wide categories from construction materials to optical coatings, from block copolymers to cell adhesion. In MEMS systems, one common failure mechanism is adhesion between structures that prevents the normal motion and function of the devices [69], which is due to their large surface-to-volume ratio. Hydrophobic self-assembled monolayers (SAMs) have been used as coatings in micromachines for the purpose of adhesion reduction, which cause the apparent work of adhesion of polysilicon cantilever beams reduced by four orders of magnitude [70]. The interfacial adhesion of a SAMs-based system to a substrate is rather strong due to covalent siloxane (Si-O-Si) bonds to the surface or metal thiolate (Au-S) bonds.

In the case of carbon nanosheets, their covalent bonds to the surface have been already cleaved and some free radicals are consequently formed. If a carbon nanosheet is transferred to a new substrate, the interfacial adhesion is mainly due to van der Waals interactions rather than previous chemical bonds. How big the interfacial strength is or how much force it needs to peel the carbon nanosheet from the surface, the answers to these questions are very important in determining the performance and the reliability of the nanosheets-based MEMS systems or the flexible organic electronic devices. They are important to build a fundamental adhesion model for a monolayer-substrate system.

4.1.2 Evidence of strong adhesion between a nanosheet and a substrate

In the mechanical characterization of suspended thin membranes, one of the most crucial procedures is mounting the membranes. For semiconductors, the membranes are prepared on a sacrifice layer by sputtering or vapor deposition. The substrate and sacrifice layer are then selectively removed from the backside and the suspended membrane to be measured is supported by the sacrifice layer patterns that are not removed. In the case of polymers, the membranes are formed by casting the film in a mold composed of two clamping plates that fit into the mounting metal disks. In our experiments, the nanosheet is transferred together with a transfer medium onto a silicon substrate which has structured orifices. The transfer medium is subsequently dissolved in acetone and only the carbon nanosheet is left on the silicon substrate.

We observed that carbon nanosheets adhere to substrates very strongly. Even the treatment in an ultrasonicating bath is not able to separate the nanosheets from the substrates. One argument was that delamination or blisters will form unless there is covalent bonding to the surface. It is speculated that the nanosheets might slip on the surface during gas pressure loading. If such a slipping event really occurs, we could immediately find out with the central point method in the bulge test. Here we show the result from one experiment where the deflection of a membrane was recorded

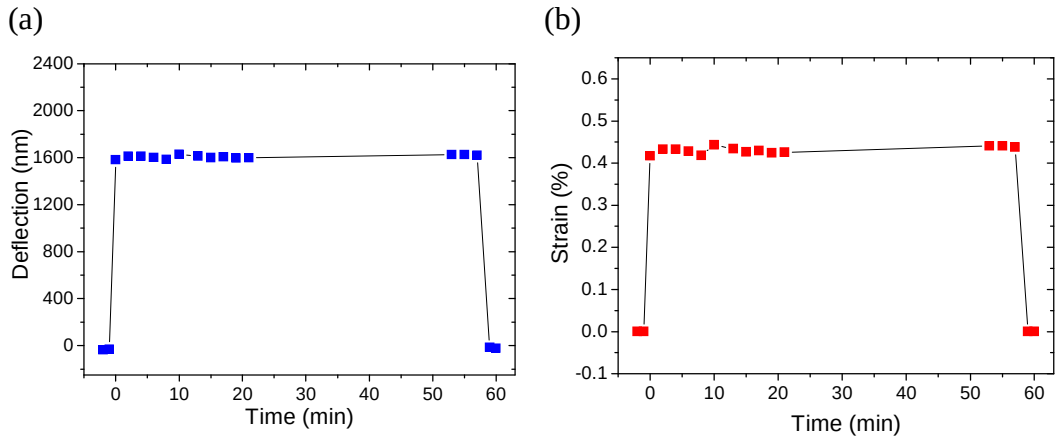

Fig. 25 (a) Deflection of a nanosheet keeps constant at a pressure of 1375 Pa, which indicates a time-independent behavior; (b) Strain of the nanosheet also keeps constant.

under a certain pressure for 1h. Due to the uncertainties in pressure controlling, the pressure applied to the membrane was 1375±75 Pa. The deflection of that membrane was 1607±15 nm and the corresponding tensile strain was 0.431±0.008 %, as shown in fig. 25a and 25b, respectively. It turns out that the interfacial adhesion is very strong and a slipping of the monolayer due to pressure loading is impossible.

4.1.3 Interfacial adhesion between a carbon nanosheet and a substrate

To simplify the interfacial interaction between a carbon nanosheet and a substrate, we first consider an ideal substrate with a perfectly flat surface. We take the Lennard-Jones potential model which describes the interaction of a pair of atoms or non-polar molecules,

$$V(r) = -4\varepsilon\left[\left(\frac{h_0}{r}\right)^6 - \left(\frac{h_0}{r}\right)^{12}\right] \tag{34}$$

where ε is the depth of potential well, h_0 is the separation at which the potential is zero, r is the distance between the atoms. The r^{-6} term describes the attraction at long range due to van der Waals forces and London dispersion forces. The r^{-12} term describes the repulsion due to overlapping electron orbitals. For one atom on an ideal surface, we integrate the energy between this molecule and all the atoms in the substrate to obtain an atom-surface potential and then integrate an atom-surface potential for all atoms in a flat monolayer. The interaction potential between a flat monolayer and a flat substrate surface can be written as [71]

$$V(r) = -\Gamma_0\left[\frac{3}{2}\left(\frac{h_0}{r}\right)^3 - \frac{1}{2}\left(\frac{h_0}{r}\right)^9\right] \tag{35}$$

where Γ_0 is the interfacial adhesion energy per unit area, c_1 and c_2 are constants for attractive and repulsive forces, h_0 is the equilibrium separation, r is the distance between the monolayer and the substrate. When the distance is equal to the

equilibrium separation, the interaction potential reaches a minimum and the interfacial adhesion energy corresponds to the depth of the energy well at the equilibrium.

The separation between a carbon nanosheet and a substrate can be estimated from the height profiles which are determined by AFM and the thickness of carbon nanosheets which is determined by XPS. XPS spectra indicate that the thickness of the BPT nanosheets ranges from 8.5 to 9.5 Å. The AFM height profiles exhibit that BPT nanosheets have a thickness ranging from 12.0 to 14.0 Å. It indicates that BPT nanosheets that have been transferred to a substrate have a separation values ranging from 3.5 to 4.5 Å. For a graphene monolayer, the equilibrium separation between it and an oxide substrate was assumed to be similar to the interlayer spacing in bulk graphite (3.4 Å) and the AFM measurements reported the height ranging from 4.0 to 9.0 Å [72, 73].

The adhesion energy between a carbon nanosheet and a substrate has not yet been experimentally measured so far. For a graphene monolayer, the adhesion energy was estimated according to the interlayer interaction energy in graphite, which has a value of 0.6 eV/nm^2 (0.096 J/m^2). In the case of the carbon nanosheet, we estimate the adhesion energy as 30 mJ/m^2, based on the adhesion energy of the hydrocarbons in the range of 20~36 mJ/m^2 [71, 74-75].

By taking the first derivative of equation (2), the van der Waals interaction between a monolayer and a flat substrate is presented as

$$F_{vdW} = \frac{9\Gamma_0}{2h_0}\left[\left(\frac{h_0}{z}\right)^4 - \left(\frac{h_0}{z}\right)^{10}\right] \tag{36}$$

When the distance is equal to $0.165h_0$, the van der Waals force reaches its maximum. We obtain a maximum van der Waals force of 120 MPa, taking the equilibrium separation as 4 Å and the adhesion energy as 30 mJ/m^2. The force is approximately half of the value for a graphene monolayer (~230 MPa)[76].

4.1.4 Corrugation of carbon nanosheet on a substrate

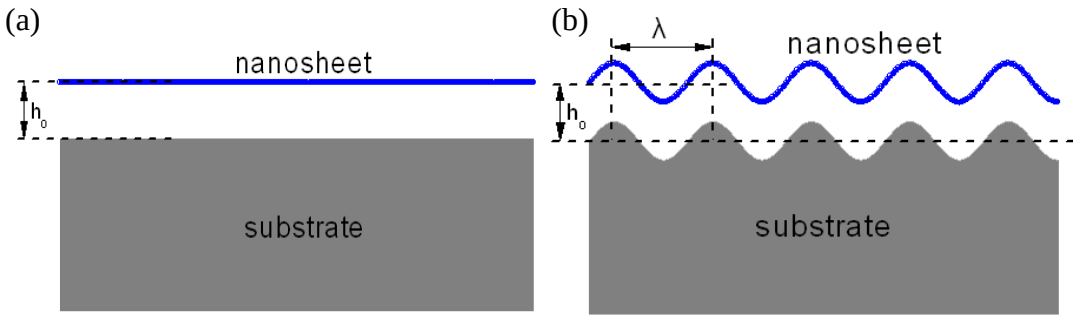

Fig. 26 (a) Schematic illustration of a flat carbon nanosheet on a flat surface with a separation of h_0; (b) Schematic illustration of a carbon nanosheet on a corrugated substrate surface with a corrugation wavelength λ.

We have discussed the ideal case for a flat carbon nanosheet on a flat surface, where the van der Waals force can be estimated from the adhesion energy and the separation, as shown in fig. 26a. In reality, the surface of a substrate usually exhibits a nanometer-scale roughness which can be assumed to be sinusoidal with an wavelength λ and an amplitude δ, as shown in fig. 26b. When the carbon nanosheet is transferred onto a corrugated surface, the van der Waals interaction between a monolayer and a substrate tends to conform the monolayer to the corrugation, however, the elastic strain energy which resulted from corrugation tends to counteract the corrugation and thus form a flat morphology. Since a carbon nanosheet has a lower stiffness than a graphene monolayer, we believe that the carbon nanosheet is much more conformal to the substrate surface than the graphene monolayer. Furthermore, considering the transfer medium (double layer PMMA) is not yet removed after the carbon nanosheet is transferred to the substrate, we believe that the elastic strain energy is contributed both from the transfer medium and the carbon nanosheet.

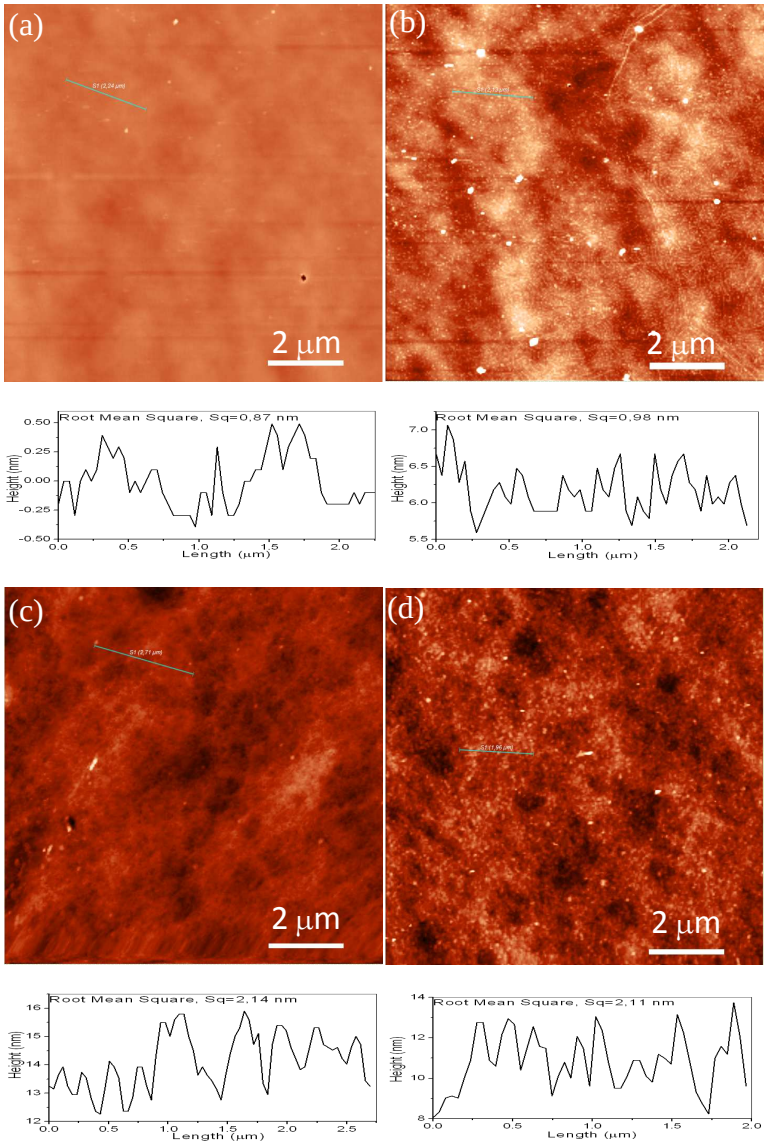

Fig. 27 (a) and (b) AFM images of SiO_2/Si substrate topside surface without and with a BPT carbon nanosheet and their corresponding height profiles; (c) and (d) AFM images of the backside surface of a SiO_2/Si wafer without and with a BPT carbon nanosheet and their corresponding height profiles.

The equilibrium morphology is thus determined by competition between the van der Waals interaction and the elasticity of the PMMA/nanosheet layer. If the corrugation wavelength is much larger than its amplitude, the monolayer tends to completely conform to the surface with the same corrugation wavelength and amplitude. If the wavelength is comparable to or even smaller than the amplitude, the monolayer tends to have a flatter morphology with similar corrugation wavelength and smaller amplitude.

To investigate corrugation of a carbon nanosheet on a substrate, we take a SiO_2/Si wafer (with a thickness of SiO_2 ~300 nm) which is frequently used to measure conductivity of an annealed carbon nanosheet and acts as a very basic embodiment for building electronic devices as well. The surface was found out to have long range corrugations which are multiples of the correlation length of 39 nm and the AFM measurements indicate that the correlation length of 78 nm (amplitudes: 0.196nm, 0.294 nm, 0.392 nm) and 117 nm (amplitudes: 0.294 nm, 0.392 nm, 0.589 nm) are the dominant surface morphology, as shown in fig. 27a. After the carbon nanosheet transferred onto the SiO_2 surface, the same corrugation wavelength and amplitude are observed which implies that the nanosheet conforms very well to the surface. The RMS roughness within a scanning range of 5×5 μm in both cases is very close (substrate: Sq=0.87 nm; nanosheet: Sq=0.98 nm). We have also measured the backside surface of a SiO_2 /Si wafer as a rough supporting surface for the carbon nanosheet. The surface is dominated by corrugation wavelength of 78 nm and 118 nm with a larger amplitude of 1.5 nm. The PMMA/nanosheet on the backside was determined to have the same corrugation wavelength with a smaller amplitude of 0.15 nm. After the PMMA layer was removed, the nanosheet had the same amplitude as the bare surface, as shown in fig. 27d. The RMS roughness of the nanosheet is pretty much the same as that of the bare surface (substrate: Sq=2.14 nm; nanosheet: Sq=2.11 nm).

In conclusion, carbon nanosheets are found to have a strong adhesion to the substrate, which is mainly due to the van der Waals interaction between nanosheet and substrate. The van der Waals force was estimated to be ~120 MPa which is half of that of a graphene monolayer. Our experiments exhibit that carbon nanosheets have a morphological corrugation with both wavelength and amplitude conforming to the surface with different roughness.

4.2 Local mechanical properties of freestanding carbon nanosheets

4.2.1 Adhesion between an AFM tip and a freestanding nanosheet

The adhesion between an AFM tip and a freestanding nanomembrane can be characterized through the force-distance curve which displays the cantilever's normal deflection versus the cantilever-sample displacement. The pull-off force is the resulting change in force relaxation where the adhesive bond ruptures in the course of retracting the tip. The force may come from electrostatic interaction, capillary condensation, or van der Waals interaction. We determined the pull-off forces both for the nanosheet supported on a silicon nitride frame (nanosheet/substrate) and a freestanding nanosheet. Four different positions have been chosen to derive the force-distance curves, as shown in fig. 28.

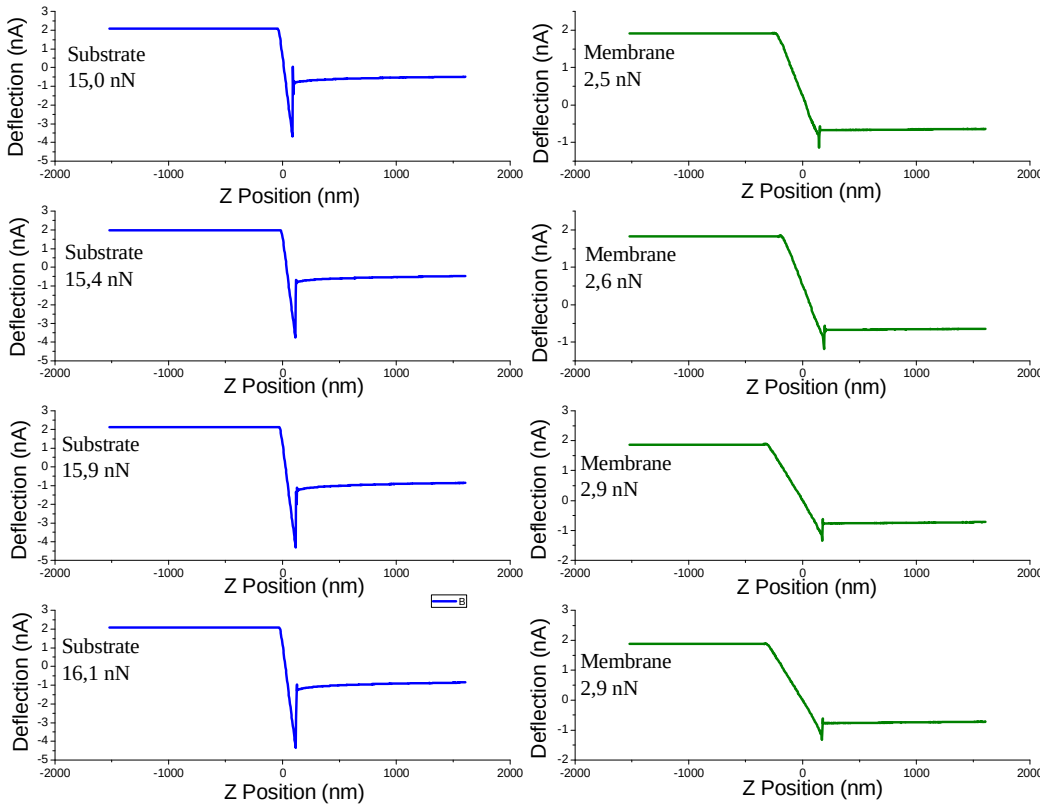

Fig. 28 Force vs. distance curves generated on a silicon nitride frame (Left column: blue curves) and a freestanding nanomembrane (Right column: olive curves), the corresponding pull-off forces are presented.

The experiments were carried out at room temperature (24.0℃) and at a relative humidity (48 %). The pull-off force is independent of relative humidity for a hydrophobic tip, while exhibits an obvious dependence for a hydrophilic tip. M. He and his coauthors refer to three distinct regimes of the pull-off forces as a function of relative humidity: van der Waals regime, mixed van der Waals-capillary regime, and capillary regime respectively [77]. The relative humidity in our experiments is in the mixed van der Waals-capillary regime. The capillary condensations keep constant both for nanosheet/substrate and the freestanding nanosheet, because there is no influence on Laplace pressure or surface tension from the substrate beneath the nanosheet. The van der Waals interaction between tip and nanosheet/substrate is contributed from both tip-nanosheet and tip-substrate interactions, which is bigger than a simple tip-nanosheet interaction. Moreover, another main contribution to a high adhesion between tip and nanosheet/substrate is the electrostatic interaction. Because the semiconductor substrate is placed on a PDMS stamp and not directly grounded, an electric charge may appear on the surface of the substrate. From the above analysis, the adhesion between tip and nanosheet/substrate should be much higher. We observed that pull-off forces for the tip-nanosheet/substrate system ranges from 15 to 16 nN, which are 5~6 times bigger than the pull-off force for the tip-nanosheet system.

This observation also gives us a hint as to why the line-scanning method in a bulge test is very destructive. Rupture events occur at the positions where the tip is scanning from the silicon frame to a freestanding nanosheet. Here an abrupt change in adhesion causes the rupture of nanosheets.

4.2.2 Deformation of a freestanding carbon nanosheet due to an AFM tip

Bending stiffness can be derived from continuum mechanics. Based on Kirchhoff hypothesis, there is a linear relationship between the classical bending modulus and Young's modulus. Bending stiffness of carbon nanosheets can be roughly derived from the following equation [78]:

$$D = \frac{Et^3}{12(1-\nu^2)} \tag{37}$$

where E and ν are Young's modulus and Poisson's ratio, t the membrane thickness. If we take a typical Young's modulus of 10 GPa and a Poisson's ratio of 0.35, thickness of 1 nm. The bending rigidity was computed to be 9.5×10^{-19} Nm. In the plate regime, the stretching in the plane of the film is negligible in comparison to the bending deformation. While in the membrane regime, the bending stiffness is negligible in comparison to the stiffness generated by prestrain or stretching arising from large deformations. Carbon nanosheets are in the membrane regime and we can neglect contribution from the bending stiffness of carbon nanosheets.

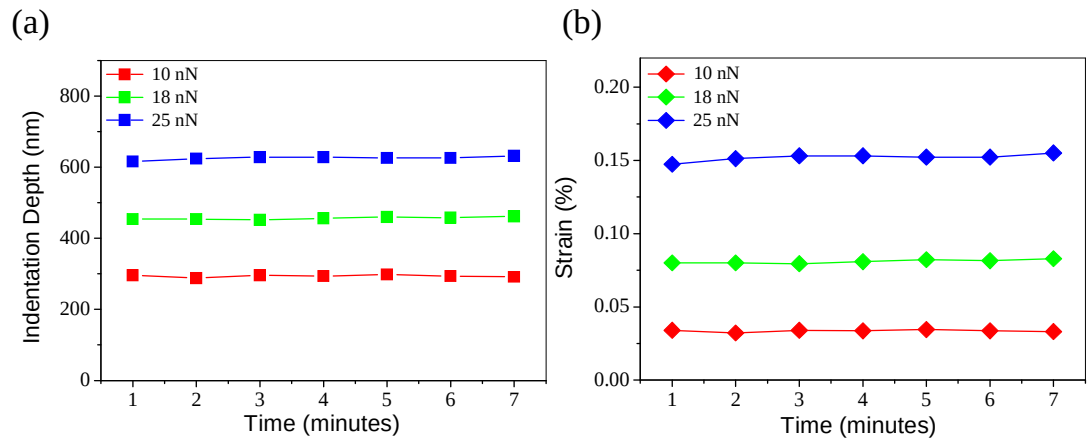

Fig. 29 (a) Indentation depth with different forces shows a time independent behavior; (b) Strain of nanosheets with different forces also shows a time independent behavior.

We want to understand the local deformation of a carbon nanosheet that is in contact with an AFM tip. Does the AFM tip cause any permanent deformation of the carbon nanosheet around the tip? What is the secure force that can be applied to the carbon nanosheets without breaking them? For that purpose, both indentation depth and strain of an unstressed membrane were measured with different forces over time, as seen in fig. 29. Neither indentation depth nor strain shows time dependent behavior. It indicates an equilibrium in the global deformation which is balanced between the force applied via an AFM tip and the stretching energy and the residual stress of the membrane. No permanent local deformation around and/or under the AFM tip was detected. However a large force will cause a permanent deformation and will even break the membrane. Our experiments suggest a secure force range until ~30 nN. In experiments, the forces to be applied are limited within 0 ~ 5 nN to avoid large correction parameters.

4.3 Elastic properties of carbon nanosheets

4.3.1 Introduction

Elasticity describes the tendency of a material under external stress to return to its original shape when the stress is removed. Linear elasticity is characterized by the relationship defined as Hooke's law where the ratio of stress to strain keeps constant. During the tensile test along an axial, the ratio of uniaxial stress to uniaxial strain is called elastic modulus or Young's modulus which is a measure of stiffness or elasticity of a material. Axial strain is usually accompanied by transverse strain in the other two directions. The ratio of transverse and axial strain with a minus sign is defined as Poisson's ratio. Most common materials have a positive Poisson's ratio ranging from 0.08 to 0.5, with few exceptions such as cubic "single crystal" pyrite ($-\frac{1}{7}$) [79] and reentrant foam (-0.7) [80].

The elastic responses of alkanethiol SAMs have been investigated by simulations [81] and experiments [82-84]. The elastic moduli have been reported to have a huge wide range from 0.15 GPa to 75 GPa. There was also a debate whether the elastic response is dependent on the number of carbon atoms in the molecular chains, with some suggesting independent behavior [81] while some believing dependence [83-84]. All the research works were limited to normal stress locally applied to alkanethiol SAMs on substrate where the substrate effect may account for the huge difference among them. Furthermore, an adhesive force between an AFM tip and the substrate and a capillary force must be taken into account to correct the results.

Carbon nanosheets provide a system that enables applying lateral stress to SAMs and measurements of its elasticity as well. As a quasi-two-dimensional material, carbon nanosheets may shed light on the understanding of the elasticity in low-dimensional material and bring challenges to experiments as well as theoretical models.

4.3.2 Determination of elastic modulus of carbon nanosheets

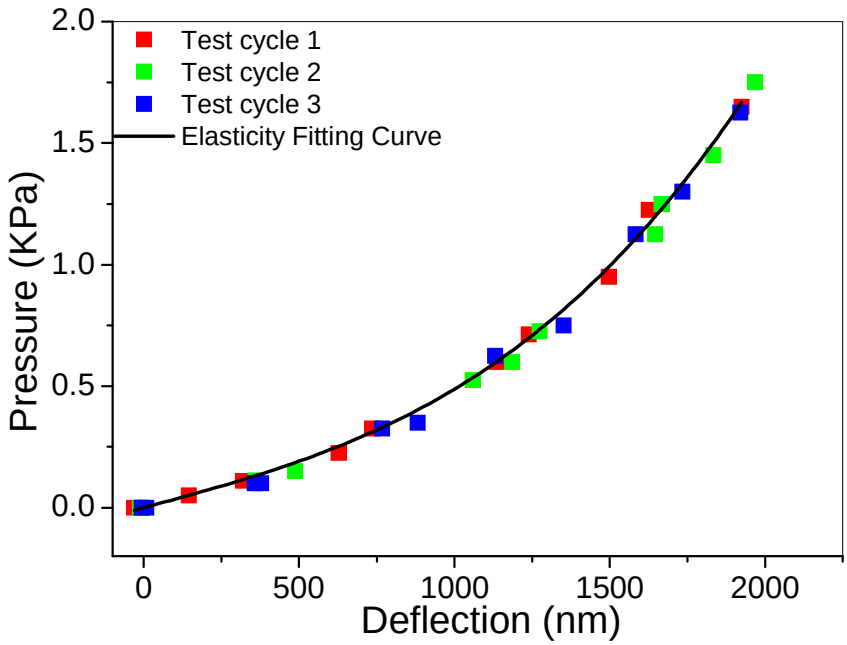

Fig. 30 Pressure and deflection relationship of a NBPT nanosheet with three loading and unloading test cycles and the corresponding elasticity fitting curve.

The central point method in a bulge test is utilized to investigate the elastic response of carbon nanosheets. A typical pressure deflection relationship obtained from a bulge test is shown in fig. 30. In order to evaluate the reproducibility of those results, we applied three loading and unloading test cycles. It was found that three test cycles were also quite similar. This indicates that there is neither a sliding of the nanosheet on the substrate nor a small permanent deformation of the nanosheet which resulted from pressure loading. It turns out that the characterization method is very reliable and has a good repeatability.

For each loading and unloading curve, we find that the loading curve is slightly higher than the unloading curve. The difference can be reduced with a longer period of time to reach the equilibrium. This hysteresis is believed to relate to the viscoelasticity of carbon nanosheets, which will be investigated in the next section in detail.

For the determination of the elastic modulus and the residual stress of freestanding carbon nanosheets, the thickness and Poisson's ratio have to be estimated. The isotropic upper limit of the Poisson's ratio is 0.5. The Poisson's ratio of polymers is in the range of 0.3~0.4. Carbon nanosheet is structurally like amorphous polymers. The Poisson's ratio is assumed to be 0.35 in all our calculations. Such an assumption will only contribute to systematic errors in the determination of Young's modulus and the residual stress. Further experiments need to be designed to determine the true Poisson's ratio of carbon nanosheets.

Table 6 Poisson's ratio of various materials [85]

Carbon & Silicon		Polymers		Metals, Ceramic & Glass	
Graphene	0.165	Polycarbonate	0.37	Gold	0.42
Isotropic Graphite	0.31	PS	0.33	Copper	0.33
Diamond (natural)	0.1~0.29	Polyvinyl Chloride	0.38	Aluminum	0.36
Diamond-like Films	0.22	Poly methyl methacrylate	0.37	Hafnium Carbide	0.18
Silicon (111)	0.27	Polyethylene Terephthalate	0.43	Glass	0.18~0.3

The thickness of nanosheets is determined from XPS spectra. Considering the attenuation of photoelectrons that penetrate through BPT SAMs, the thickness is calculated from the formula $I_S = I_S^0 \exp(-t / \lambda_{\mathrm{IMFP}} \cos\theta)$ where λ_{IMFP} indicates the inelastic mean free path (Au 4f). The inelastic mean free path is the crucial parameter in determining the film thickness. Lamont reported that the attenuation length of electrons in alkanethiol SAMs can be described by the expression $\lambda = 0.3E^{0.64}$

where E denotes the kinetic energy of photoelectrons [86]. It was believed that λ_{IMFP} also depends sensitively on the film density which can locally vary significantly and the value 32 Å is achieved by using the Gries formula and an effective density of 1.63 g/cm^3 for the BPT SAMs [87].

Fig. 31 shows XPS spectra of C 1s, S 2p and Au 4f regions of both BPT SAMs and NBPT SAMs. It was calculated that BPT SAMs usually have a thickness of 10.0±0.7 Å and NBPT SAMs 12.5±0.8Å, with the inelastic mean free path value of 36 Å [88]. Electron-induced irradiation could slightly decrease the thickness of BPT nanosheets to ~9 Å. From a mechanical point of view, the main contribution to elasticity is from biphenyl rings and the functional groups have much less effect on the mechanical properties. In our work, we take the thickness of carbon nanosheets as 1 nm.

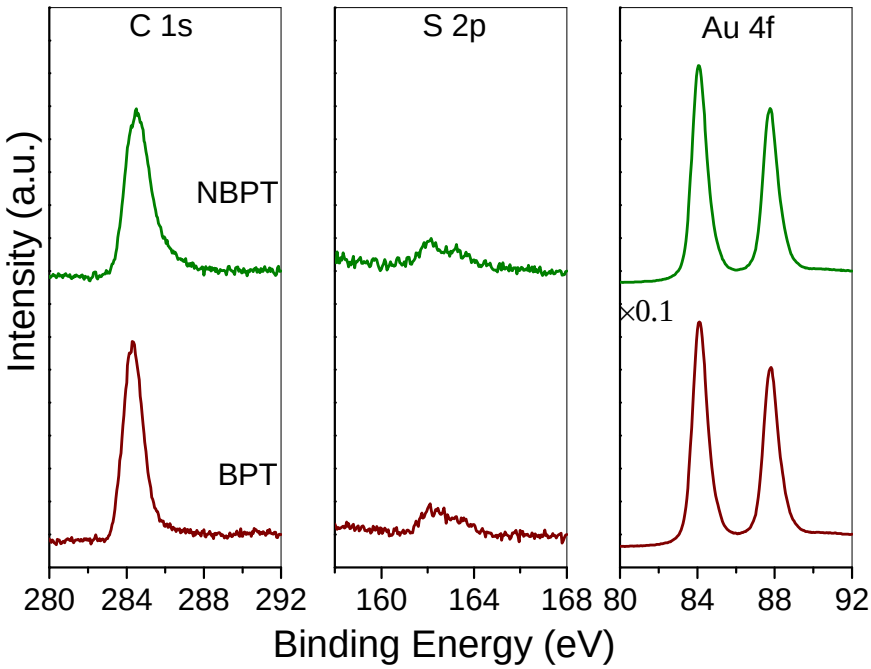

Fig. 31 XPS spectra of BPT and NBPT SAMs on Au surface acquired with a monochromatic Al-K$_\alpha$ source and the effective thickness is determined by comparison of Au 4f intensity of a clean Au substrate and that of the samples.

Table 7 Young's modulus of a NBPT nanosheet

Young's Modulus (GPa)	Loading	Unloading	Average Value
Test Cycle 1	10.2	11.2	10.7
Test Cycle 2	11.2	12.2	11.7
Test Cycle 3	10.2	12.2	11.2

Table 8 Residual stress of a NBPT nanosheet

Residual Stress (MPa)	Loading	Unloading	Average Value
Test Cycle 1	52.7	44.3	48.5
Test Cycle 2	46.5	37.2	41.9
Test Cycle 3	50.7	37.3	44.0

Table 7 and 8 present an example of Young's modulus and residual stress for a NBPT nanosheet with three successive loading and unloading cycles. Small differences among these measurements are observed which indicates that this method is quite repeatable. The values obtained from unloading measurements show a higher Young's modulus and lower residual stress compared with those for loading measurements, which is also correlated with pressure and deflection relationships in which loading curves are slightly higher than unloading curves. The average values are taken to estimate Young's moduli and residual stress more precisely.

4.3.3 Electron irradiation dose effect

In order to understand the low energy electrons induced crosslinking process in the formation of carbon nanosheets, we measured the mechanical properties of carbon nanosheets as a function of electron doses. Three different kinds of molecules with biphenyl rings have been used to prepare carbon nanosheets for comparison. They are 4'-[(3-trimethoxysilyl)propoxy]-[1,1'-biphenyl]-4-carbonitril(CBPS), 4'-Nitro-1,1'-biphenyl-4-thiol(NBPT) and 1,1'-biphenyl-4-thiol (BPT). Fig. 32 shows the evolution of the mechanical stabilities during the cross-linking process, Young's modulus of carbon nanosheets as a function of irradiated electron doses.

Below 20 mC/cm^2, cross-linkages in SAMs are not mechanically stable enough to support and to form suspended carbon nanosheets. No intact membranes can be obtained. From 30 mC/cm^2 to 40 mC/cm^2, more and more cross-linkages are formed and promote stabilities of suspended carbon nanosheets. Very few intact membranes can be obtained. For CBPS nanosheets, Young's modulus with an electron dose of 30 mC/cm^2 is a little bit higher than that at 40 mC/cm^2. The results can be interpreted in the way that incomplete statistic values from very few intact membranes might overestimate Young's modulus.

In case of BPT nanosheets, when the irradiation electron doses are above 50 mC/cm^2, cross-linkages are getting saturated and Young's moduli are in the range of 6~8 GPa. In case of NBPT nanosheets, the mechanical stiffness exhibits quite stable characteristics when the electron doses exceed 50 mC/cm^2 and Young's moduli of carbon nanosheets tends to keep constant at 8~10 GPa. CBPS nanosheets show a similar behavior in the mechanical stiffness. But it still shows a small increase at higher electron doses. Since CBPS SAMs are prepared on Si_3N_4 substrates, considering the secondary electron yield, we cannot assume the same electron dose as that received by BPT and NBPT SAMs on an Au substrate. It has been demonstrated that the degradation of SAMs is strongly dependent on conductivity of substrate [34].

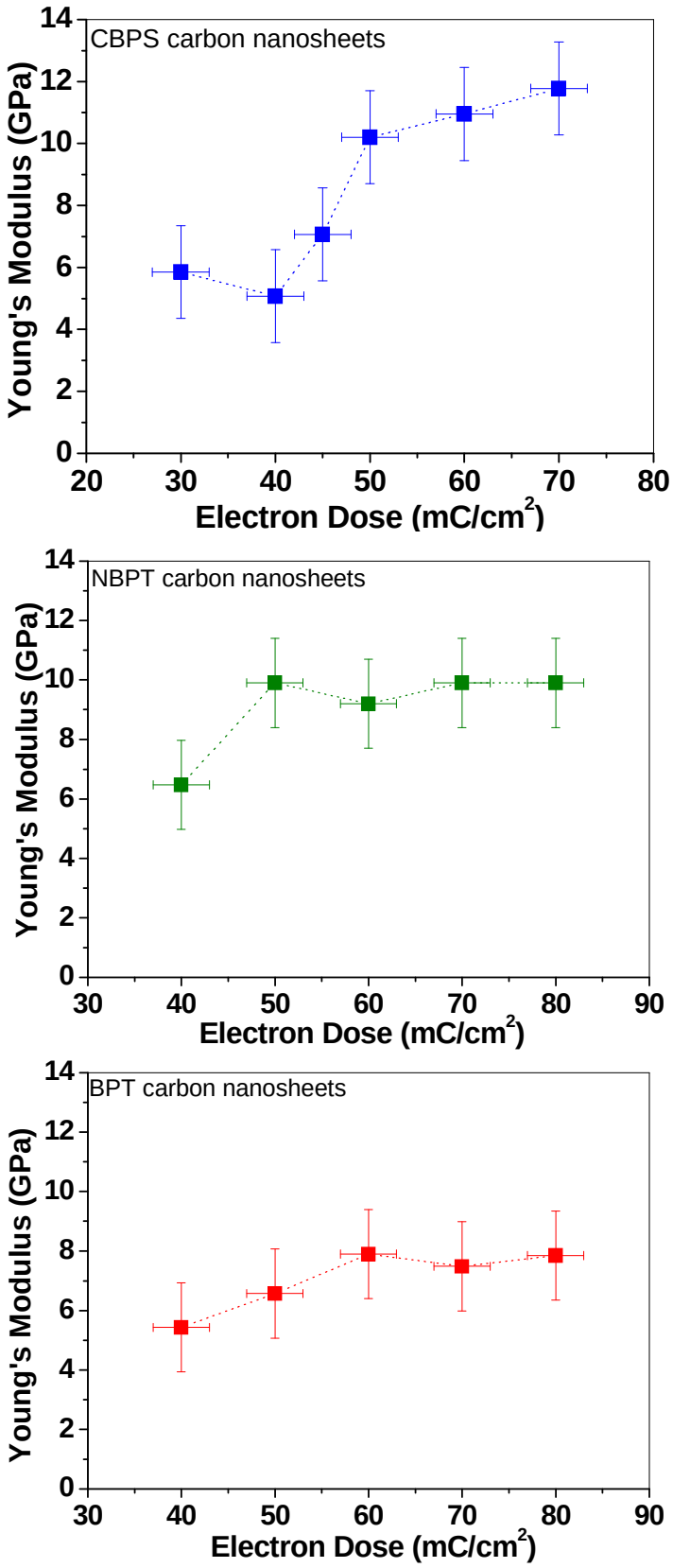

Fig. 32 Young's modulus of CBPS, NBPT and BPT carbon nanosheets as a function of electron irradiation doses.

In the same way, at a given electron dose, aromatic SAMs on semiconductor substrate endure different crosslinking compared with those on metals. In our experiments, we use conductive pure silver paint on the substrate to ground the sample, but a possible static charge buildup may still exist, we need further investigation on the charging effect of CBPS nanosheets on Si_3N_4 substrate due to the electrons.

4.3.4 Size effect

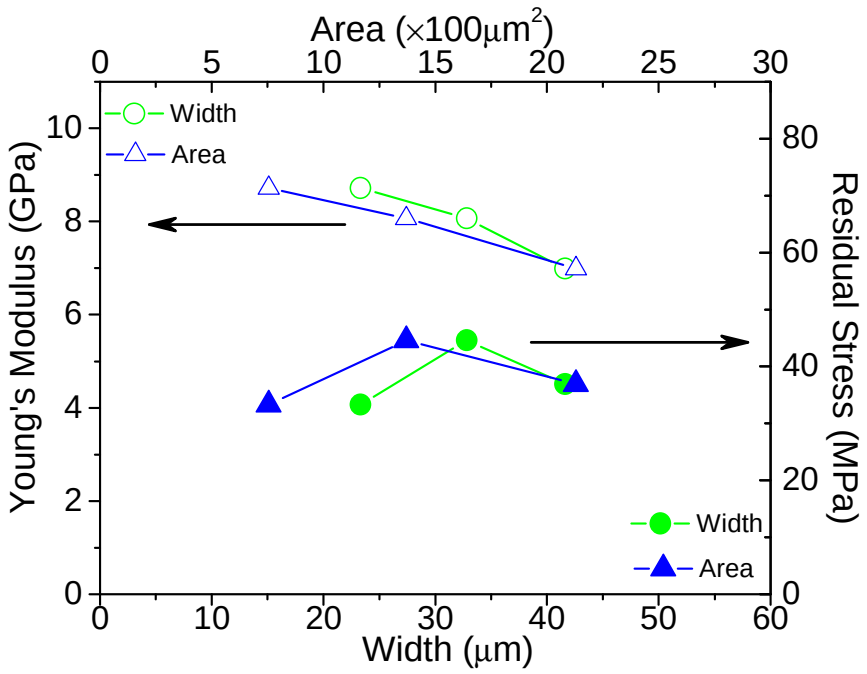

Fig. 33 Young's modulus and residual stress as a function of membranes' width and area.

As shown in fig. 33, smaller membranes tend to exhibit a higher Young's modulus, while residual stresses don't display a size dependent behavior. The phenomenon may be interpreted under two aspects: (1) Limitations of the theoretical formula in determining nanoscale membranes and in boundary conditions of the monolayer/substrate system due to the interfacial adhesion; (2) Large random errors in determining the central point of membranes with sizes smaller than 30 μm. Accordingly the membranes' sizes ranging from 30 to 50 μm give more consistent values.

4.4 Viscoelasticity of carbon nanosheets

4.4.1 Introduction

In the previous section we assumed that carbon nanosheets behave as a linear elastic material in small strains which can be described by Hook's law. However, in reality, all materials deviate from Hook's law in various ways, for example, both viscous and elastic characteristics under a constant load, so called viscoelasticity. Viscoelasticity refers to the deformation exhibits time-dependent behavior, which manifests itself in a number of ways, such as creep, relaxation and hysteresis.

Creep describes that strain increases with time under a constant load and creep rate increases at elevated temperatures. This characteristic exists in many materials, such as metals, ceramics, polycrystalline solid, polymers and so on. Sliding and climbing of dislocations, sliding of grain boundaries and diffusional flow are the basic mechanisms of creep in metals and polycrystalline solids. In polymers, there are two types of bonds: strong chemical bonds along the main chains in polymers and weak intermolecular bonds. It's hard to determine which type of bond determines the creep behavior of polymers. Regel [89] reported that ultraviolet radiation can break chemical bonds in the main chain of polymers and the creep rate increased by a few orders of magnitude. In the same way, both active liquid media and hydrostatic pressure can influence the intermolecular interaction and reduce them, which leads to a significant increase of the creep rate. In case of crosslinked polymers, a constant load leads to a creep deformation and the equilibrium compliance will be established. After the load is removed, the recovery deformation follows a mirror image of the creep deformation and no permanent flow phenomena appear [90].

Carbon nanosheets can be considered as a crosslinked 2D polymeric network. The creep and recovery deformation are expected to be observed. In this section, we employ an experiment to determine the creep deformation under a constant load. We will present the results on the initial strain when the creep occurs, creep rates as a function of applied stress and discuss the recovery deformation as well.

4.4.2 Experimental description

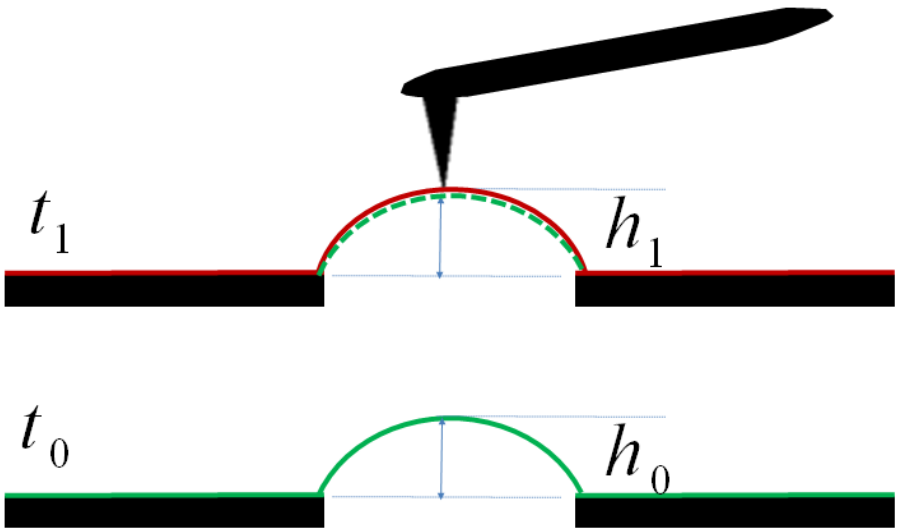

Fig. 34 A schematic diagram of the time-dependent deformation determined by the AFM.

The time-dependent deformations were carried out by performing bulge testing in an AFM. The central point method is chosen for probing the small change in the displacement of the membrane under certain pressure. As shown in the scheme fig. 34, the deflection of a carbon nanosheet could be determined as h_0 that is measured at time t_0; At time t_1, the carbon nanosheet experiences a small deformation that leads to a deflection increasing to h_1.

The tensile train can be derived from the following formula

$$\varepsilon = \frac{2h^2}{3a^2} \tag{38}$$

where h is the deflection and a is the half-width of membrane.

The creep rate is equal to the derivative of the creep strain ε with respect to time t

$$\frac{d\varepsilon}{dt} = \frac{d}{dt}\left(\frac{2h^2}{3a^2}\right) = \frac{4h}{3a^2} \times \frac{h_1 - h_0}{t_1 - t_0} \tag{39}$$

The creep rate has a unit of percentage of elongation/hour or % of elongation/second.

4.4.3 Results and discussion

Hysteresis in Carbon Nanosheets

In section 4.3, we observed that the loading portion of the pressure-deflection curve was higher than the unloading curve. We considered such a small hysteresis loop as an indication of specific characteristic of the viscoelasticity in carbon nanosheets. The pressure-deflection curves can be converted into the stress-strain curves in terms of the equations mentioned in section 3.2.

Fig. 35a shows the stress-strain curves of three cyclic loading and unloading measurements with a maximum strain at 0.85 %. They represent very little hysteresis between the loading and unloading curve, as well as a slight deviation existing among those cyclic measurements. The stretching energy dissipated as heat in the loading cycles and the energy loss is equal to the area between the loading and unloading curves. Fig. 35b also shows three stress-strain curves of loading-unloading measurements, with increasing maximum strains at ~0.65 %, ~1.2 % and ~1.7 %, respectively. The hysteresis loops between the loading and unloading curves were observed to increase with increasing the tensile strain. The dissipation energy as a function of the stress level could be further investigated and determined.

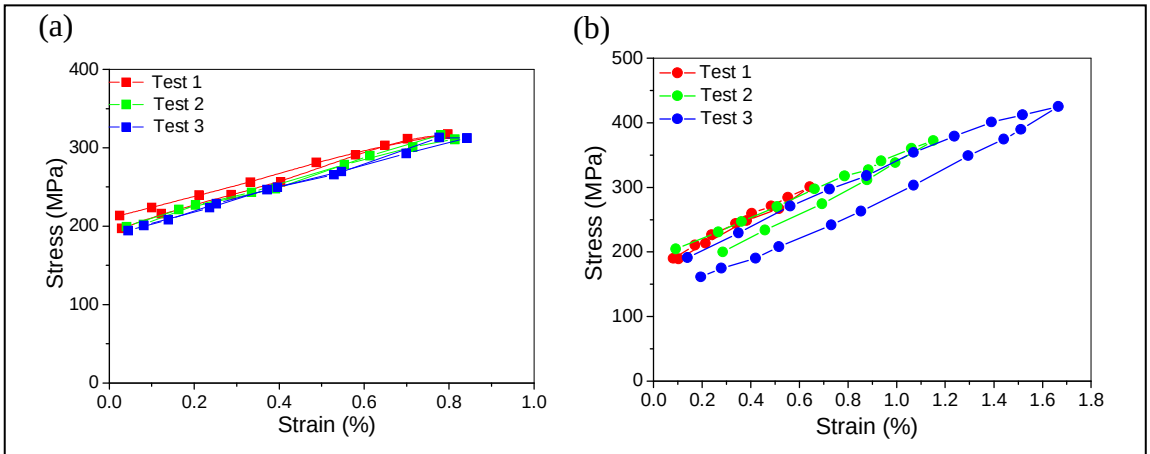

Fig. 35 (a) Stress-strain relationship of three successive loading-unloading measurements with the same maximum strain up to ~0.85 %. (b) Stress-strain relationship of three loading-unloading measurements with different maximum strains at ~0.65 %, ~1.2 %, ~1.7 %, respectively.

Tensile creep and stress relaxation in carbon nanosheets

Creep refers to the general characteristic of viscoelastic materials that undergo an increased deformation along time when loaded under a constant stress. Stress relaxation describes another characteristic of viscoelastic materials. The stress undergoes a relaxing process while under a fixed level of strain.

In our experiment, the deflection of carbon nanosheets can be recorded with time at room temperature. During the whole measurement, the pressure is kept as stable as possible, however still a small decrease in pressure was observed as a result of stress relaxation. A quantitative analysis was possible to be carried out by means of the central point method. As shown in fig. 36a, the strain fluctuates randomly from 0.816 % to 0.824 % when the nanosheet was stressed at 156 MPa. When the membrane was stressed over a certain limit, the creep deformation can be clearly observed with the AFM. The deflection of the membrane was measured every two minutes. A linear relationship between strain and time and the fitting curve was plotted in fig 36b.

The determination of the starting point of creep in carbon nanosheets is very important for engineering this material. It depends on the stress accumulated in the membrane that can overcome certain energy barriers and also relates to the sensitivity

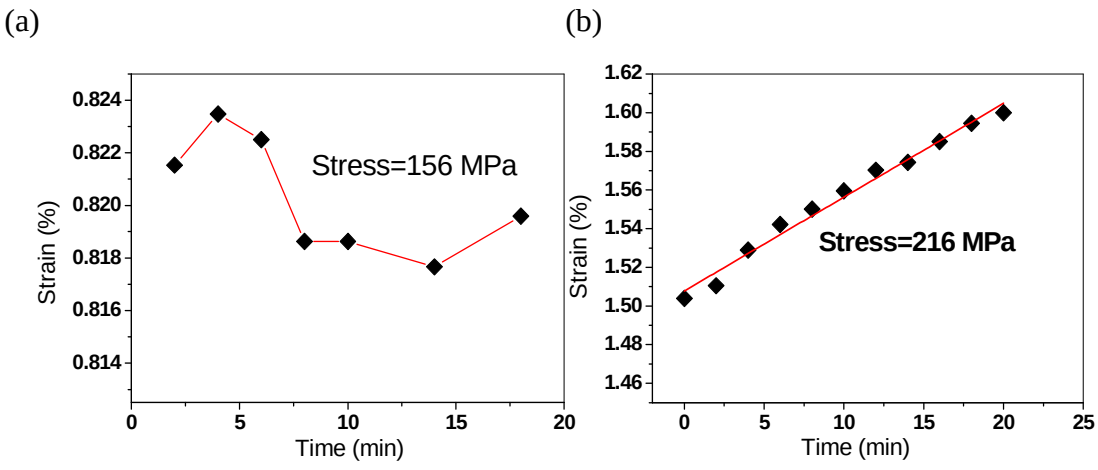

Fig 36 The time-dependent deformation of a carbon nanosheet: (a) Random variation of strain under an external tensile stress of 156 MPa; (b) An obvious time-dependent deformation under an external tensile stress of 216 MPa.

of instruments used for measurements. In case of a membrane that has a width of 60 μm and a deflection of 120 nm, the AFM can determine 1 nm variation in deflection every 2 min, the corresponding sensitivity of the strain rate is in the range of 10^{-8}~10^{-9} s^{-1}. However, the sensitivity of the AFM in determining the strain rate is rather limited by the pressure supply which fluctuates randomly and causes big errors to the deflection signal. As a result, we could determine a strain rate in the range of 10^{-7} s^{-1}.

Table 9 Creep strain and creep stress at starting point in different samples

Sample	Creep strain (%)	Creep stress (MPa)	Young's Modulus (GPa)
NBPT_I2	0.93	257	6.86
NBPT_E2	1.09	287	9.81
NBPT_E4	1.01	320	9.66

Table 9 shows the results of strain and stress values above which a creep behavior was detected by the AFM instrument. The creep strain ranges from 0.9 % to 1.2% and the corresponding stress from 250 MPa to 320 MPa. Carbon nanosheets with bigger Young's moduli creep at a higher tensile strain, which implies that the microstructures of carbon nanosheets play an important role both in elasticity and creep properties. The strain rates at the beginning of the creep are also variable from membranes with

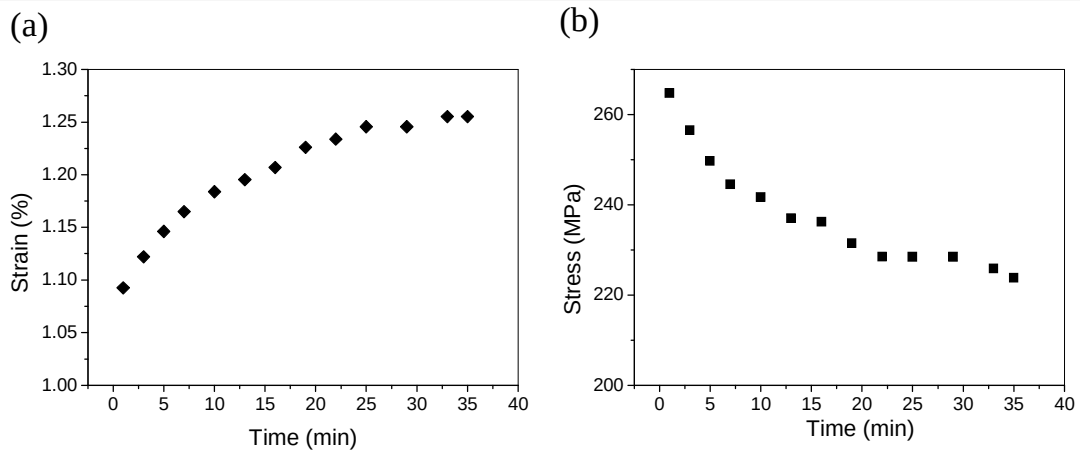

Fig. 37 (a) Creep deformation of a BPT carbon nanosheet; (b) Stress relaxation of the same carbon nanosheet.

different stiffness and range from $1.5\times10^{-6}s^{-1}$ to $3\times10^{-6}s^{-1}$.

As shown in fig. 37a, at a large time scale, strain is not linearly proportional to time and the growth exhibits a logarithmic growth along time, accompanied with a decreasing rate. The decrease in the strain rate is related to work-hardening of materials. Fig. 37b shows that the stress is also slowly decreasing with time, which can be explained by stress relaxation. In our experiments, we focus on creep behavior rather than stress relaxation.

Creep rate of carbon nanosheets

The creep rate $\frac{d\varepsilon}{dt}$ depends on the stress level and the temperature. It can be roughly derived from the slope of the creep curve. We observe that the creep rate of carbon nanosheets at room temperature is proportional both to tensile strain and tensile stress, as shown in fig. 38. Unlike polymers whose creep rate could span several orders of magnitude under different stress levels, carbon nanosheets display a rather stable creep rate in the range of 10^{-6} s^{-1}, even though being under a tensile strain 3.5 % that will lead to rupture. Furthermore, the creep rate is rather low compared to polymers. Traditional plastic polymers, such as polyamide (PA), polyethylene (PE) and poly(propylene) (PP), have a creep rate in the range of 10^{-4}~10^{-2} s^{-1} under a very low

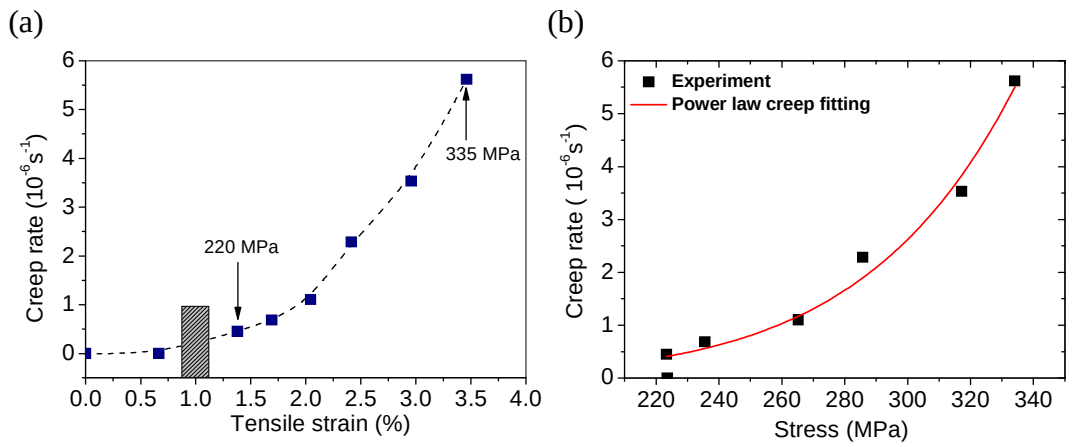

Fig 38 (a) Creep rate as a function of tensile strain, the creep can be only observed above certain strain; (b) Creep rate as a function of tensile stress and the corresponding power law creep fitting curve.

stress level, e.g. 14 MPa [91]. Enhancement of resistance to creep for polymers is favorable to realize by incorporation of micro- or nano-sized inorganic particles in the polymer matrix or distribution of inorganic networks in the soft organic polymer matrix. Here carbon nanosheets exhibit a very high resistance against creep which normally leads to failure. It indicates that the matrix of cross-linked SAMs is quite dense and close. Such unique and intrinsic structural properties of the matrix in a carbon nanosheet could be further proven by the gas permeability and ion transportation experiments.

Recovery of carbon nanosheets

In many high polymers, creep under a constant load can be subdivided into reversible and irreversible components. To understand the reversible creep in carbon nanosheets, we employed two different experiments: (1) Repeat the creep tests after a certain period of time and examine the recovery from those creep curves; (2) Measure the steady-state deflection at a lower stress level, afterwards the membrane is loaded to a higher stress level and held for a certain period, then unload the membrane for another certain period and load it to the same lower stress level and measure the corresponding steady-state deflection.

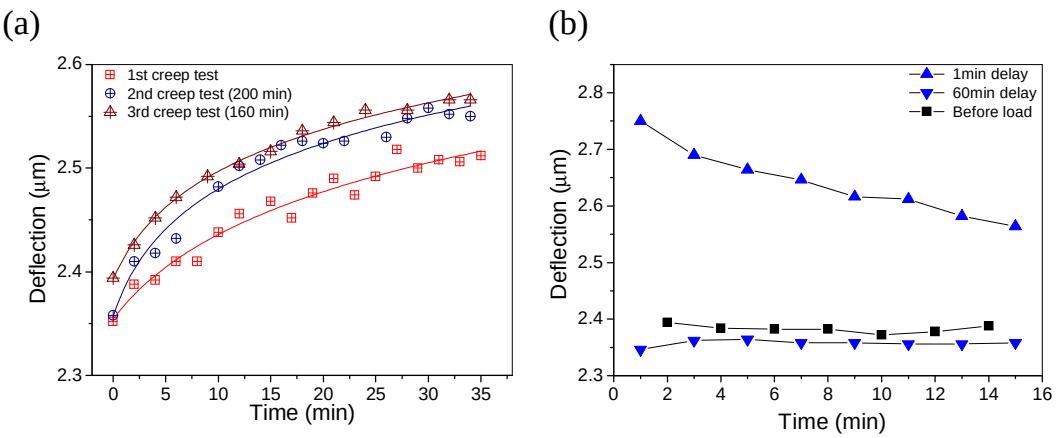

Fig 39 (a) Three creep deformations were recorded at room temperature, the second test was carried out 200 min after unloading and the third 160 min, respectively; (b) Deflection of a BPT nanosheet at 1.6±0.1 KPa before loading to a higher pressure (~4 KPa), 1 min and 60 min after unloading, respectively.

The results from the first experiment were presented in fig. 39a. Three creep tests were recorded at room temperature. The second and third creep tests were carried out 200 and 160 minutes after the last creep test, respectively. It indicates that carbon nanosheets undergo a slow recovery after creep unloading. It is also worthy to mention that stress relaxations were observed in these creep tests. The final steady-state stress in the second and third creep tests are 98 % and 94 % of that in the first creep test.

The second experiment was presented in fig. 39. The membrane's deflection was stabilized at 2.4 μm under a constant pressure ~1.6 KPa. The membrane was loaded to ~4 KPa for 5 min and was thus unloaded. After 1 min the membrane was again loaded to ~1.6 KPa, the resultant deflection was observed to decrease from 2.75 μm to 2.56 μm. After another 60 min, the deflection at ~1.6 KPa was stabilized at 2.35 μm, which is pretty close to the first steady deflection.

Both experiments demonstrated recovery of carbon nanosheets after creep unloading. It seems that most of the creep deformation could recover after a certain period of time, which implies that constant load leads to a slow process of molecular rearrangement that is temporary and reversible.

In summary, we have characterized time-dependent properties of carbon nanosheets. Carbon nanosheets show typical viscoelastic behavior as high polymers. Hysteresis, creep and relaxation were observed and the minimum strain that causes creep was thus determined. The creep rate increases with stress levels but appears to be rather stable in the range of 10^{-6} s^{-1}. Recovery from creep deformation is also demonstrated. The mechanism for the creep and recovery in carbon nanosheets is still not clear and further investigation should be performed.

4.5 Rupture of carbon nanosheets

4.5.1 Introduction

Ultimate tensile strength describes the maximum strength that a material can withstand when subjected to an external tension. It is one of the most important parameters for material engineering and applications, from which the failure of devices can be estimated under certain working conditions.

For bulk specimens, the common way to determine tensile strength is a micro-tensile testing machine where the specimen with a fixed cross section is clamped and pulled with a controlled and gradually increased force until it fails. For single molecules, the kinetics of bond rupture can be directly measured with an AFM and some theoretical models have been introduced to explain bond rupture [92]. However, the tensile strength and the rupture mechanism of ultrathin nanomembranes are not well understood. Watanabe [93] reported the ultimate tensile strength of ultrathin (20~40 nm) crosslinked organic macromolecules (e.g. melamine resin, urethane resin and phthalic resin) by means of the bulge test. The observed tensile strength of these nanomembranes is approximately 25% of the value for conventional materials.

Since the carbon nanosheet is a new 2D polymeric material, determination of tensile strength is very important for the application of this material. The rupture mechanism of carbon nanosheets is also crucial due to the fracture involving breaking bonds on the atomic level including the rigid covalent bonding and weak interactions between molecular domains. It may serve as a bridge to extract the energy landscape from a single molecular bond rupture to the fracture of macroscopic materials.

In this section, rupture testing is simply performed in a bulge test in order to determine the ultimate tensile strength of carbon nanosheets. The burst pressure is used to calculate the ultimate strength. The tensile strength of BPT nanosheets and NBPT nanosheets are compared in a basic statistic way. The mechanism will be discussed in a preliminary way.

4.5.2 Determination of ultimate tensile strength

The bulge test technique is used to determine the ultimate tensile strength of thin membranes from the burst pressure. For a small deflection compared to the dimensions of the membrane, a spherical shape may be assumed and other higher order geometrical terms are neglected. As we discussed before, the relationship between stress and pressure in a thin walled spherical pressure vessel is

$$\sigma_x = \frac{PR}{c_0 t} \tag{40}$$

where σ_x is the stress in the x direction, P is the pressure applied to the membrane, R is the radius of curvature and t is the thickness of the membrane. c_0 is a constant that is dependent on the geometry of the membrane. Substituting $R \approx a^2 / 2h$ for in this equation,

$$\sigma_x = \frac{Pa^2}{2c_0 th} = \frac{Pa^2}{c_1 th} \tag{41}$$

where a is the half width of the membrane in the x direction, h is the deflection of the membrane. $c_1 = 2c_0$ is a geometric parameter. For rectangular membranes c_1 is a function of aspect ratio. Long-rectangular means a much higher aspect ratio $b/a \geq 4$.

$$c_1 = \begin{cases} 4 \cdots\cdots\cdots\cdots \text{circular} \\ 3.393 \cdots\cdots\cdots \text{square} \\ c_1(b/a) \cdots\cdots \text{rectangular} \\ 2 \cdots\cdots\cdots\cdots \text{long-rectangular} \end{cases} \tag{42}$$

The strain can be obtained from the geometric considerations:

$$\varepsilon_x = \frac{R\theta - a}{a} \cong \frac{\arcsin\theta - \frac{a}{R}}{\frac{a}{R}} \approx \frac{(\frac{a}{R} + \frac{a^3}{6R^3}) - \frac{a}{R}}{\frac{a}{R}} = \frac{2h^2}{3a^2} \tag{43}$$

Because rupture events occur usually at higher pressure and the corresponding deflection is rather determined by the stretching energy of the membrane. The deflection of a membrane at higher pressure and the constant c_2 are given as

$$h = \left(\frac{Pa^4(1-\nu)}{c_2 Et}\right)^{1/3} \tag{44}$$

$$c_2 = \begin{cases} 8/3 \cdots\cdots\cdots\cdots\cdots\cdots \text{circular} \\ (0.8+0.062\nu)^{-3} \cdots\cdots \text{square} \\ g(\nu, b/a)^{-3} \cdots\cdots\cdots \text{rectangular} \\ 4/3(1+\nu) \cdots\cdots\cdots \text{long-rectangular} \end{cases} \tag{45}$$

where $g(\nu, b/a)$ is a function of the Poisson's ratio and the aspect ratio of the membrane and the value is taken from the literature.

Here we neglected the influence of residual stress on the ultimate deflection as well as the influence of the tensile creep at a higher load. Both assumptions overestimate the ultimate deflection value to some extent and thus underestimate the ultimate tensile strength of carbon nanosheets. Combine it with the equation for calculating membrane's stress and ultimate tensile stress σ_u and the corresponding ultimate strain ε_x may be presented as follows:

$$\begin{aligned} \sigma_x{}^3 &= \frac{EP^2a^2}{t^2(1-\nu)} \times \frac{c_2}{c_1{}^3} \\ \varepsilon_x &= \frac{2}{3}\left(\frac{Pa(1-\nu)}{c_2 Et}\right)^{2/3} \end{aligned} \tag{46}$$

If the residual stress is taken into account, the deflection will be re-estimated according to the pressure ratio that are both balanced by residual stress and stretching energy of a membrane.

$$
\begin{aligned}
P &= P_1 + P_2 = nP + (1-n)P \\
nP &= \frac{c_1 \sigma_0 t}{a^2} h_1 \\
(1-n)P &= \frac{c_2 E t}{a^4 (1-\nu)} h_2^{\,3}
\end{aligned}
\tag{47}
$$

Deflection values are calculated from both linear term h_1 for residual stress and cubic term $h_2^{\,3}$ for the stretching energy and compared to each other, by adjusting the ratio n of two parts of pressure until two deflection values converge ($h_1 = h_2 = h$). Substitute the new deflection value h into equation (44), the ultimate tensile strength is thus corrected.

In case of a membrane with a residual stress of 70~100 MPa, the pressure which is used to balance the residual stress is estimated to be 15~25 percent of the whole pressure that is applied to the membrane. It gives rise to an additional correction factor to enhance the ultimate tensile strength with ~30 MPa.

4.5.3 Results and discussions

When a differential pressure is gradually increasing and is applied to a membrane, a rupture incident occurs at the point where the pressure was recorded as burst pressure. There are several ways to monitor the rupture of membranes. The first one is to land the AFM tip directly on the membrane and observe the rupture from a DFL signal of photodiodes. The advantage is that the rupture incident can be precisely and directly determined and the disadvantage is that the influence of the AFM tip has to be taken into account. The second way is to observe with an optical microscope whether the membrane is still intact. This is a nondestructive method and it has yet rather bigger uncertainty compared to the fist method. During pressure loading in our experiments, the membranes are examined immediately after the pressure is increased. Small steps are chosen when the pressures are close to the estimated burst pressure.

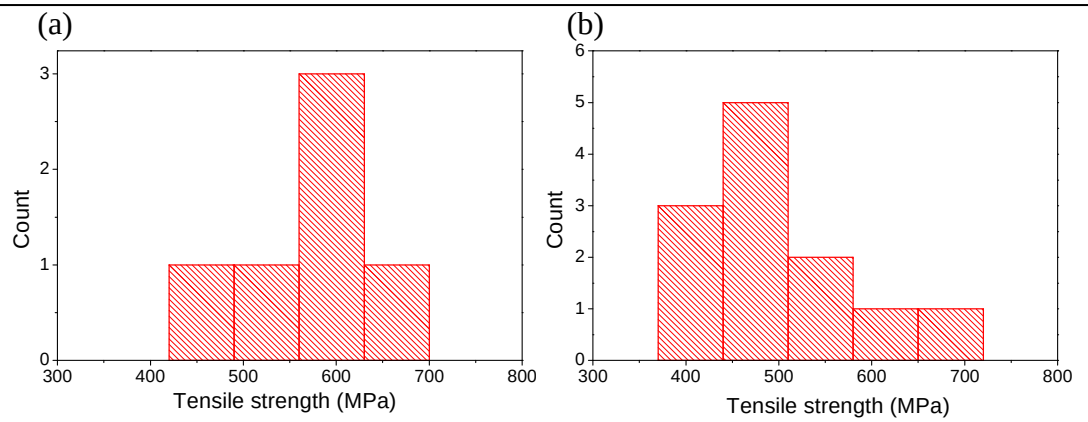

Fig. 40 (a) Histogram of the ultimate tensile strength of NBPT nanosheets; (b) Histogram of the ultimate tensile strength of BPT nanosheets.

Tensile strength from dynamic pressure loading is different from static pressure loading. The former causes instabilities on the membrane under a tension state, which may reduce the tensile strength value accordingly. To avoid that, gas stream is controlled as smoothly as possible in the experiments. Loading history and loading rates are considered to have influences on the rupture events. More frequent loading cycles will cause the membrane to break easily as a result of continuously cumulative permanent deformations. Therefore less loading cycles are preferred especially at higher pressure. The thermal effect of light shining in the optical microscope

Fig. 40 shows the statistical histogram of the ultimate tensile strength of 6 NBPT nanosheets and 12 BPT nanosheets. The tensile strength of NBPT nanosheets ranges from 430~700 MPa where a narrow peak is located at ~600 MPa. The tensile strength of BPT nanosheets has a relatively wide distribution, with a major peak at ~480 MPa. These results indicate that NBPT nanosheets are mechanically more stable than BPT nanosheets. From the wider distribution of BPT nanosheets, we can derive that there are more random defects in the membranes. According to XPS spectra, NBPT SAMs' thickness is determined as ~1.3 nm which is relatively higher than that of BPT nanosheets with a thickness of ~1 nm. This also suggests a better structural ordering of NBPT self-assembled monolayers. In aromatic SAMs, phenyl rings and their functional groups will introduce stronger interactions between molecule and substrate, as well between adjacent molecules. During the formation of the standing-up phase of

SAMs, hydrophobic interaction may become a competing driving force as the interactions of head-head group and molecule-molecule. Biphenylthiol molecules with a smaller dipole moment tend to have a higher adsorption rate which may create a bigger energy barrier for new molecules. It also explains why the exchange rate of BPT SAMs replaced by NBPT SAMs is three times lower than the other way round [94]. The NBPT molecule has a larger dipole moment and the mobility of molecules in solvent is expected to be better than BPT molecules. The mobility of molecules that are already bonded to the substrate reduces the energy barrier for new molecules and thus results in a good packing density of the monolayers. Among all other nanomembranes, IPN nanocomposite with organic-inorganic networks exhibit the highest tensile strength as 105 MPa [109]. Tensile strength of carbon nanosheets is 4~7 times higher than IPN nanocomposite.

Fig. 41a shows the tensile strength of three circular NBPT membranes as a function of diameters. With the decrease of dimensions, the membranes exhibit an increasing ultimate tensile strength. Fig. 41b shows that the circular nanomembranes have higher tensile strength than square membranes do. With a uniform pressure applied, the circular membranes have a uniform stress distribution. However square membranes bear a stress that gradually decreases from the middle of its sides to its corners. Such a non-uniform stress distribution enhances the possibility of a rupture event and thus

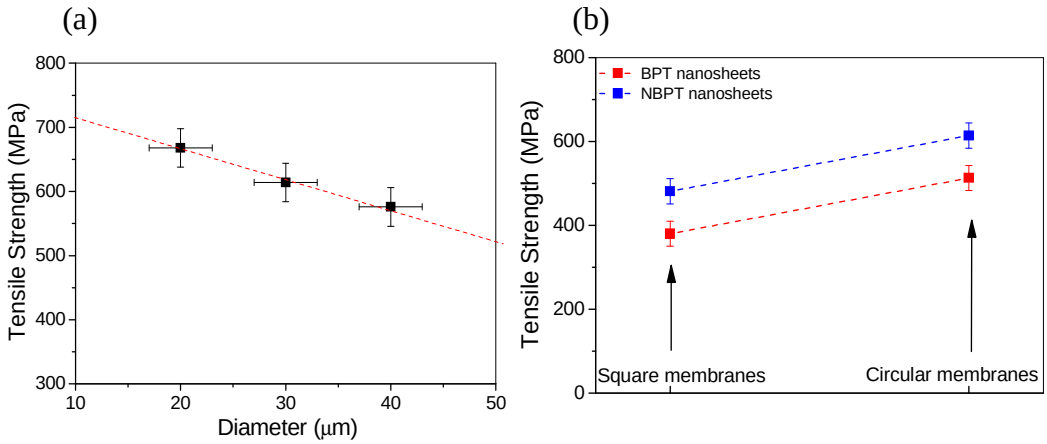

Fig. 41 (a) Tensile strength as a function of membranes' diameters; (b) Circular membranes show higher tensile strength than square membranes do.

reduces their ultimate tensile strength.

The rupture mechanism of carbon nanosheets is rather complex. If SAMs are regarded as an ideal two-dimensional system without defects, the fracture will be only related to the breaking of covalent bonds. In reality, it is well known that SAMs contain a few defects. First of all, some defects are caused by the substrate, such as surface impurities, gold vacancy islands, defects at gold crystalline grain boundaries, defects at gold step edges and so on. Secondly, some defects are formed as a result of the impurity of molecules, impurity of the solution during preparation, and the humidity and oxygen content in the atmosphere of the solution. Lastly, the formation of SAMs is a thermodynamic process and some defects are formed dynamically due to desorption of molecules from the substrate. Besides those defects formed during SAM preparation, new defects may be introduced into monolayers during the crosslinking process. It was reported that electron irradiation with a very low dose leads to noticeable reorientation of SAM constituents, creating potential sites for the exchange. As a result, creation of irradiation-induced defects seems to occur with a higher rate than crosslinking at the initial stage of irradiation [95].

Carbon nanosheets contain densely and uniformly distributed covalent bonds. They come either from the molecules themselves or form in the crosslinking process. Carbon nanosheets contain the relatively weak bonds in different kinds of defects and among those molecular domains as well. During pressure loading, the monolayer undergoes a series of structural rearrangements where stress is built up as stretching energy, and dissipated as thermal fluctuations. When the mechanical stress accumulated in the monolayer exceeds relatively weak bonds in those defects or among molecular domains, weak bonds are to break and defects may grow and coalesce consequently until a rupture event occurs. Therefore more experiments need to be carried out, for example observing defects growth with high-resolution transmission electron microscope (HRTEM) and observing free radicals with electron paramagnetic resonance (EPR), to obtain a better and complete understanding of the rupture mechanism of carbon nanosheets.

4.6 Multilayer carbon nanosheets

A multilayer system consists of a series of thin films, either metal, dielectric or polymer thin films, which are constructed in a certain way to meet a variety of requirements. Multilayer optical coatings are very important in advanced lenses and mirrors, optical fiber telecommunications. Multilayer polymer films are mainly used as food packages and multichannel medical bags.

Multilayer devices are prepared in various ways. Multilayer inorganic thin films are usually prepared by vacuum deposition, such as sputtering and evaporation. Multilayer polymer films are produced using co-extrusion and lamination techniques.

In this section, we introduce a technique to fabricate multilayer carbon nanosheets that could also be transferred to other substrates. The mechanical characterization has been performed on these freestanding multilayer carbon nanosheets.

4.6.1 Fabrication of freestanding multilayer nanosheets

Fabrication procedure is schematically shown in fig. 42. First of all, carbon nanosheets together with double layer PMMA (130 nm PMMA 50K/ 260 nm PMMA 950 K) are transferred on a silicon nitride substrate (150 nm Si_3N_4/10 nm SiO_2/Si, CryTec). After being baked at 90℃ for 2 min, the sample is mounted on a Teflon sample holder and immersed into acetone solvent and thus sonicated in an ultrasonic bath for 15 minutes. Afterwards the sample is rinsed with methanol and blown dry with nitrogen. It is possible to examine the completeness of the monolayer with an optical microscope. The second layer of carbon nanosheets with a PMMA double layer will be transferred onto the first monolayer. The same procedure is repeated to dissolve PMMA on the monolayer. The sample needs to be checked up with an optical microscope to make sure that each new layer is completely transferred.

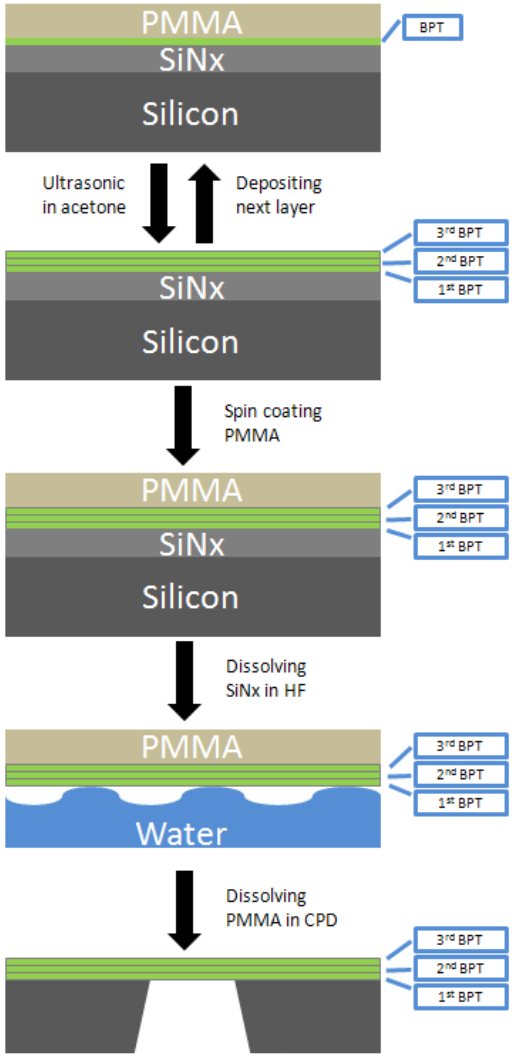

Fig. 42 Schematic diagrams describes the fabrication procedures of a freestanding multilayer carbon nanosheet.

When the desired number of layers has been reached, fresh PMMA will be spin coated onto the last layer of multilayer carbon nanosheets. Connections between PMMA and the edges of substrate need to be broken using a sharp blade, so that the HF solution can easily penetrate the interface. After a few seconds, the sample could be taken out from HF solution for further transferring. For the purpose of mechanical measurements it will be transferred to the silicon substrate with window-structured openings. Fig. 43 shows the optical microscopic images of a single layer, double layer and four multilayer carbon nanosheets in a suspended state.

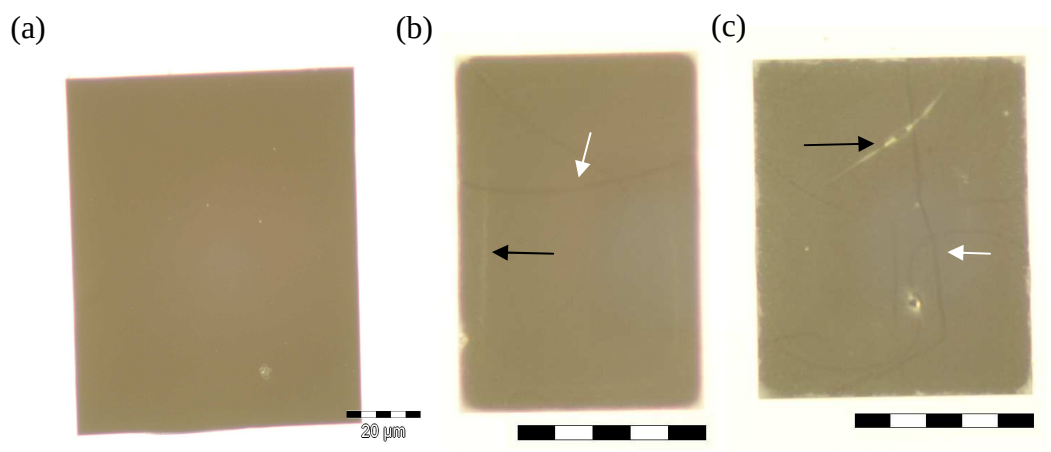

Fig. 43 The optical microscopy images of freestanding carbon nanosheets: (a) single layer; (b) double layers; (c) four multilayers. Scale bar: 20 μm

Since carbon nanosheets are quite flexible and have a relatively low stiffness, folds may exist in the nanosheets when they are transferred to new substrates. Once nanosheets are made freestanding, they have more freedom to adjust themselves and counteract those uneven morphologies. For a single monolayer, such folds cannot be observed on the freestanding nanosheets with an optical microscope. However, in multilayer carbon nanosheets, those folds probably existing in each layer are embedded in the system and could not be relaxed even in a suspended state. That is the reason why folds may often be clearly observed in multilayer carbon nanosheets. These folding features are one of the disadvantages of multilayer carbon nanosheets. On the other hand, microscopic cracks and holes, as well as invisible molecular defects can also be embedded in a multilayer stack. It improves the mechanical stability of suspended multilayer nanosheets and will enhance the yield of suspended multilayer nanosheets in even bigger sizes. Folds and cracks are shown in fig. 43 with black and white arrows, respectively.

4.6.2 Mechanical properties of multilayer nanosheets

The mechanical characterization of multilayer nanosheets is carried out by means of bulge testing. For larger membranes (>20 μm), the central point can be precisely

determined with a micro-positional system in an AFM instrument. In case of smaller membranes, we need to scan the membrane to find the central position.

We prepared multilayer nanosheets with various dimensions, such as of rectangular and circular shape, as well as of various sizes from 4 μm in diameter to around 30 by 60 μm in dimensions. The thicknesses are estimated to be a number of layers multiplied by 1 nm. All the results were presented in table 10. Basically, circular membranes have shown to be in agreement with each other, even though they have different dimensions with up to five times of size.

For measuring the small membranes with diameters below 10 μm, we have to scan the membrane to determine the central point due to the increased difficulties in the central point method. The deviation between rectangular and circular membranes was not so prominent. Such a random error is acceptable, because folds and cracks are also playing an important role in the mechanical stiffness of multilayer nanosheets. Such influence is not easily to be quantified and taken into account.

Table 10 Young's moduli of multilayer carbon nanosheets

Geometry	Sample	Number of layers	Young's Modulus (GPa)	Dimension
Rectangular Membranes	XZB004_D5	2 (~1.3)	5.6 (~8.8)	34.3×58.3 μm
	XZB004_D4	2	9.3	33.5×57.0 μm
	XZB010_F2	4	9.7	30.3×37.6 μm
Circular Membranes	XZB010_2	2	6.1	20 μm in diameter
	XZB012_3	3	6.7	4 μm in diameter
	XZB012_4	4	6.8	5 μm in diameter

It is worthy to mention that sample XZB004_D5 and XZB004_D4 are different membranes on the same substrate and they also have similar sizes. But Young's modulus of XZB004_D5 is about 40 % lower than that of XZB004_D4. The explanation for such an abnormal phenomenon would be that double layers in XZB004_D5 are not complete. From an optical microscope image we found that the membrane consisted of a complete first monolayer and only part of (about 30%) the second layer. If we take the thickness as 1.3 nm, Young's modulus would be 8.8 GPa for sample XZB004_D5, which is pretty close to the value of sample XZB004_D4.

In summary, we have successfully fabricated multilayer carbon nanosheets. The average Young's modulus is demonstrated to be very similar to the single layer carbon nanosheet. However, there are some open questions relating to multilayer nanosheets, for example, what interactions are there between each monolayer? How do they influence the mechanical stiffness? For answering these questions, further experiments need to be designed and a theoretical model is required as well.

4.7 Annealed carbon nanosheets

4.7.1 Introduction

In material science, annealing is a heating treatment through which desirable properties of materials can be achieved. For metal, this treatment will alter the microstructures and phase structures and it provides a way to adjust the strength and hardness of that material. For polymers, annealing can relieve the internal stress and also bring some changes in morphology, crystallization, chain mobility and thermodynamic properties. Apart from tailoring properties of the original materials via annealing treatment, organic polymers can also be utilized as a precursor to prepare other inorganic materials. Kyotani [96] reported that highly orientated graphite was prepared from polyacrylonitrile (PAN) by making use of the interlamellar openings of montmorillonite (MONT) as a two-dimensional space for cabonization, whereas carbon atoms from PAN between MONT are further subjected to annealing treatment after being released from MONT. This research suggested a way to prepare the multilayer graphene from organic molecules or polymers that are constrained in a limited space. Carbon nanotubes with diameters in the range of 40~200 nm have also been prepared from PAN using a porous aluminium oxide template via high-temperature pyrolysis [97].

Cross-linked aromatic SAMs were found to have a high thermal stability with an annealing termperature of ~1000 K [98]. Molecular surface patterns can be created due to desorption of non-crosslinked molecules and conservation of crosslinked structures after annealing treatment. Such a novel system provides a molecular route to prepare new two-dimensional carbon networks when subjected to an annealing treatment. Firstly, the monolayer could provide a carbon matrix as a precursor for the molecular rearrangement at high temperature. Secondly, the limited number of carbon atoms allows the formation of new structures with the thickness of only one nanometer. In this section, we will discuss the structural transformation of carbon nanosheets upon annealing treatment as well as their mechanical properties.

4.7.2 Structural transformation of carbon nanosheets upon annealing

The electrical properties of annealed nanosheets have been determined both with a two-point measurement in UHV and a four-point measurement under ambient conditions [99]. It was found that the annealing treatment can transform carbon nanosheets from an insulating to a conducting state. Sheet resistivity values measured in both methods are in very good agreement. After annealing at ~800 K, sheet resistivity corresponds to ~108 kΩ/□. Increasing the annealing temperature to ~1200 K, drops the sheet resistivity to ~100 kΩ/□, demonstrating the clear metallic nature of the film. This resistivity is only one order of magnitude higher than that of a defect-free graphene monolayer [100], and ~100 times lower than the sheet resistivity of single chemically reduced graphene oxide sheets [101], which are currently most favored for the mass production of graphene.

High-resolution transmission electron microscopy (HRTEM) was used to investigate the structural transformation of carbon nanosheets upon annealing [99]. For non-annealed carbon nanosheets, only one amorphous phase can be observed. For annealed carbon nanosheets, some curvy and parallel fringes can be observed, which indicates the presence of graphitic materials. From the selected area electron diffraction (SAED) patterns, the sharpness and intensity of the rings that correspond to the real space periodicities of 0.11 ± 0.02 nm and 0.20 ± 0.02 nm, increase in the samples which are annealed at higher temperatures and this indicates a progressing ordering in the graphitic nanosheets.

Raman spectroscopy has also been used to investigate the structural transformation of carbon nanosheets upon annealing. For annealing temperatures above 700 K, two peaks, at ~1350 and ~1590 cm^{-1}, are observed in the Raman spectrum. The Raman line at around 1580 cm^{-1}, the so-called G band, is assigned to the E_{2g} species of the infinite crystal. The other line at 1355 cm^{-1}, the so called D band, is attributed to the vibration mode A_{1g} of the graphite lattice which achieves Raman activity at the borders of the crystalline areas due to loss of translational symmetry. Since Raman

spectroscopy is very sensitive to structural disorder in different types of graphite and carbon, a small FWHM (full width at half maximum) of those lines indicates higher graphitization in the sample. The intensity ratio (R) of the D line to the G line is directly related to the "amount of crystal boundary".

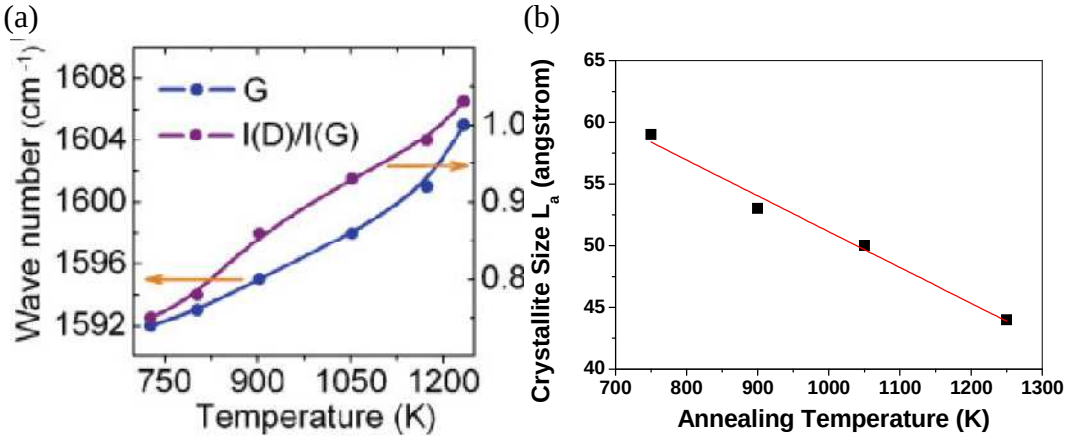

Fig. 44 (a) The intensity ratio of I(D)/I(G) and the position of G line as a function of annealing temperature (image taken from reference 99); (b) The crystallite size L_a as a function of annealing temperature.

Tuinstra and Koenig [102] have reported that the intensity ratio of the D line to the G line is reversely proportional to the average crystal size L_a in the graphite plane determined from X-ray diffraction techniques. They presented an experimental curve relating a series of samples in powders without orientational effect which can be used to estimate the average crystal size in annealed carbon nanosheets.

As shown in fig. 44a, the intensity ratio R=I(D)/I(G) systematically increased from ~0.75 to ~1 as the annealing temperature increased from ~750 K to ~1250 K. The average crystallite size of graphite in the annealed nanosheets can be obtained by substituting the intensity ratio R in that experimental curve. The relationship of crystallite size L_a and annealing temperature is shown in fig. 44b. It indicates that annealed nanosheets exhibit an average crystallite size of 50 Å, however a higher annealing temperature leads to a slight decrease of L_a, which may result from the desorption of more molecules with weaker bonds.

4.7.3 Mechanical properties of annealed carbon nanosheets

The structural transformation of a crosslinked aromatic monolayer is also reflected in its mechanical properties. To quantify these, we also fabricated a nanomechanical pressure sensor in which the annealed nanosheet acts as a membrane. This rather simple device demonstrates the utilization of carbon nanomembranes as nanomechanical transducers. Freely suspended nanosheets were mounted onto a sealed pressure cell, and a well-defined pressure difference between both sides of the membrane was applied. The resulting membrane deflection was measured by the AFM and was used to determine Young's modulus and the residual strain of nanosheets by bulge tests. Figure 45a shows an AFM image of a nanosheet annealed at ~900 K without applied pressure. Although the membrane is pushed down ~15nm by the tip, it remains intact. By applying a pressure of ~450 Pa to the sealed cell under the membrane, an upward deformation (bulging) occurs (Fig. 45b). This deformation is quantified by recording the AFM tip height at the membrane center as function of the applied pressure.

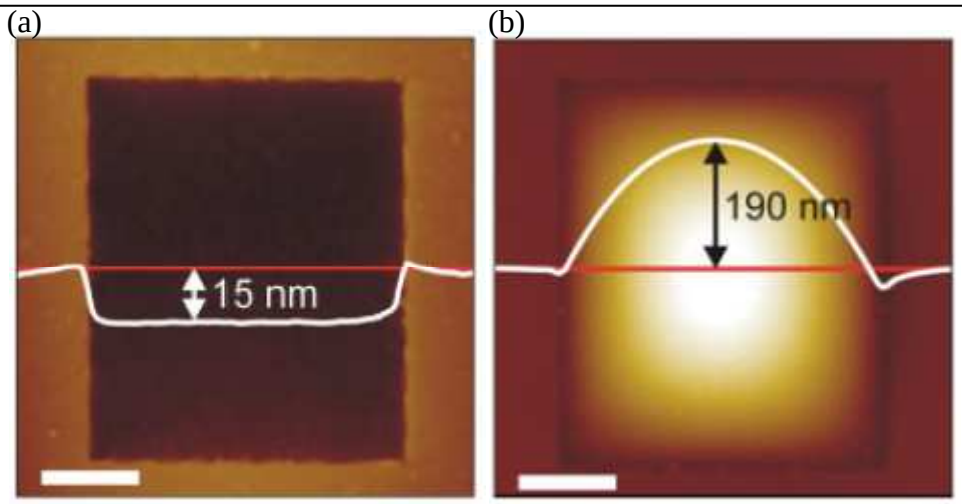

Fig. 45 AFM images of a membrane (topography, contact mode) (a) without and (b) with an applied pressure of 450 Pa. Scale bar: 10 mm. Line scans along the red lines are superimposed to the AFM images. (Images taken from reference 99)

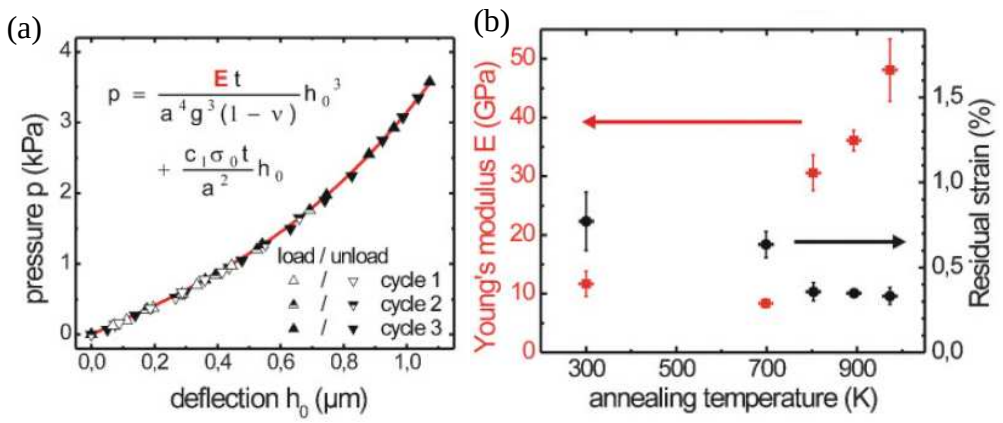

Fig. 46 (a) Young's modulus determination is presented for one nanomembrane (annealed at ~900 K). First the deflection at the membranes center is measured for different pressures, and then data are fitted by the displayed dependency, which yields the modulus. (b) Young's modulus as function of annealing temperature. At higher temperatures, the modulus shifts toward the value of graphite. (Images taken from reference 99)

Deformation datasets are presented in Figure 46a, which contains three successive measurement cycles. All measured data lie on one curve, and no hysteresis is detectable, we concluded that the deformation is elastic without any permanent change within the investigated strain range of up to 0.6%. The absence of any hysteresis shows that the nanosheet does not slide on the silicon frame, presumably due to a sufficiently strong van der Waals interaction. Long-term stability was tested after five months, and no changes in the elastic properties could be observed. This demonstrates that the nanomembrane deflection can be utilized for pressure sensing. The same model for pressure–deflection was chosen and the experimental data fit very well to this model, which is plotted in Figure 46a. Curve fitting yields Young's modulus and the residual strain. Figure 46b shows both quantities as a function of the annealing temperature. Without thermal treatment, Young's modulus is ~10 GPa. This value is comparable to Young's modulus of multilayered molecular/metallic nanocomposite membranes that are thicker by an order of magnitude. Annealing leads to a systematic increase of the modulus with rising temperature, up to 48 GPa at ~1000 K. This is in good agreement with an increasing graphitization, as Young's modulus of graphite varies from 39GPa to 1.1 TPa [103], depending on its orientation.

The formation of residual strain in the nanosheet is most likely related to structural transformations during the crosslinking process. Without annealing, the nanosheet shows a residual strain of 0.8%. Annealing reduces the residual strain of the nanosheet to ~0.35% above 800 K, which correlates with the onset of conductivity. Since nanomembranes are elastic and mechanically stable at ambient conditions, they can be further utilized as sensitive diaphragms in various applications. Conducting nanomembranes may act as transducers in NEMS and open an opportunity to build highly miniaturized pressure sensors that might eventually lead to microphones with nanometer dimensions. The possibility of chemically functionalizing nanosheets by chemical lithography [104] further permits their use as highly sensitive chemical sensors that change their electromechanical characteristics upon the adsorption of distinct molecules.

In summary, annealing treatment in UHV leads to structural transformation of carbon nanosheets. Increased graphitization was observed in Raman spectra which also indicate decreased crystallite size. Their mechanical properties showed an increased Young’s modulus upon annealing treatment.

Chapter 5

Mechanical Properties of Polymer Carpets

5.1 Introduction

Ultrathin polymer membranes have been considered as one of the most promising nanomaterials, due to their potential applications as nanosensors [105, 106], nano-separation membranes [107], and functional biosensors [108].

However, nanometer-thickness and macroscopic size seem to be not easily compatible, mainly due to the mechanical stabilities of those ultrathin membranes. Therefore, different methods have been tried to enhance the mechanical strength of the nanomembranes. For example, Kunitake et al. developed methods for the preparation of large, robust, free-standing nanomembranes by taking advantage of densely cross-linked interpenetrating hybrid networks (IPN) [109] of zirconia and acrylate, as well as by means of organic components of resin alone [110] . Tsukruk et al. showed that very robust 25-70 nm thick membranes were accessible by embedding rigid gold nanoparticles within polymeric nanomembranes prepared by a so-called SA-LbL assembly (spin-assisted layer-by-layer assembly) [111].

Due to embedding of polymer chains in those polymeric nanomembranes, the sensitivity of the system is mainly dependent on the exposed chains on the surface. In contrast with polymer-based nanomembranes, polymer brushes are much more stimulus-responsive and react much faster to environmental changes, such as solvent quality, PH, ionic strength, or temperature [112]. Therefore, polymer brushes that are grafted on biphenyl-based nanosheets provide a freestanding system for the development of adaptive layers as actuators and sensors. Because their morphological analogy is just like a real carpet that consists of soft and flexible brushes that are firmly attached to a thin and rigid two-dimensional framework, we refer to this as a “polymer carpet” [113].

In this chapter, the fabrication and mechanical characterization of polymer carpets will be discussed. Both bulge testing and nanoindentation are used to characterize the mechanical properties of polymer carpets. The composite system of mechanically stable nanosheets and flexible polymer brushes will also be analyzed.

5.2 Fabrication of polymer carpets

Photochemistry is a convenient way to graft organic polymers on inorganic and organic surfaces. In a surface photografting polymerization process [114], the substrate was placed in bulk monomer with benzophenone (BP) as a photosensitizer and irradiated with UV light at 340 to 360 nm. BP is excited to a single state (S1) and transformed to a triplet state (T1) by intersystem crossing and removing hydrogen from the substrate surface. The substrate radicals formed add monomers leading to grafted chains. However, in the self-initiated photografting and photopolymerization (SIPGP) process [115], a monomer itself acts as the photosensitizer and reaches a triple state upon photon adsorption in the range of near UV (300~400 nm). This triple state is in equilibrium with a biradical species, e.g. (·St·), which initiates a free radical polymerization in solution. This biradical species can also abstract a hydrogen radical from the organic substrate and thus create a surface radical site for surface-initiated polymerization of styrene.

The scheme of polymer carpets' preparation is outlined in Fig. 47. First, a ~1 nm thin nanosheet is prepared by electron beam induced crosslinking of a biphenyl SAM. A crosslinked 4'-amino-1,1'-biphenyl-4-thiol (cABT) SAM is prepared by electron irradiation of NBPT SAMs. After detachment from the substrate and deposition onto a solid silicon support, the nanosheet was used as a 2D template to grow polymer brushes by surface-initiated polymerization (SIP), forming the polymer carpet.

The silicon supported nanosheets were submerged into approx. 1 mL of freshly distilled and degassed styrene (Fluka) in a glass photoreaction vial. Polymerization was performed under argon atmosphere for different time periods under irradiation

with UV-light (max = 350 nm) at room temperature. After the polymerization, the samples were removed from the reaction solution and immediately washed with toluene. The samples were additionally cleaned in ethyl acetate and ethanol. Freestanding polymer carpets can be obtained by dissolving a few nitride layers beneath polymer carpets in hydrofluoric (48 %) and subsequently detaching them from a solid substrate on the water.

Afterwards freestanding polymer carpets can be transferred to other substrates, such as TEM Cu grids, Si substrate with window-structured openings for the mechanical characterization. We found out that no transferring medium is required for polymer carpets with a thickness bigger than 30 nm, while the transferring medium required for the thinner membranes due to difficulty of observing them with naked eyes.

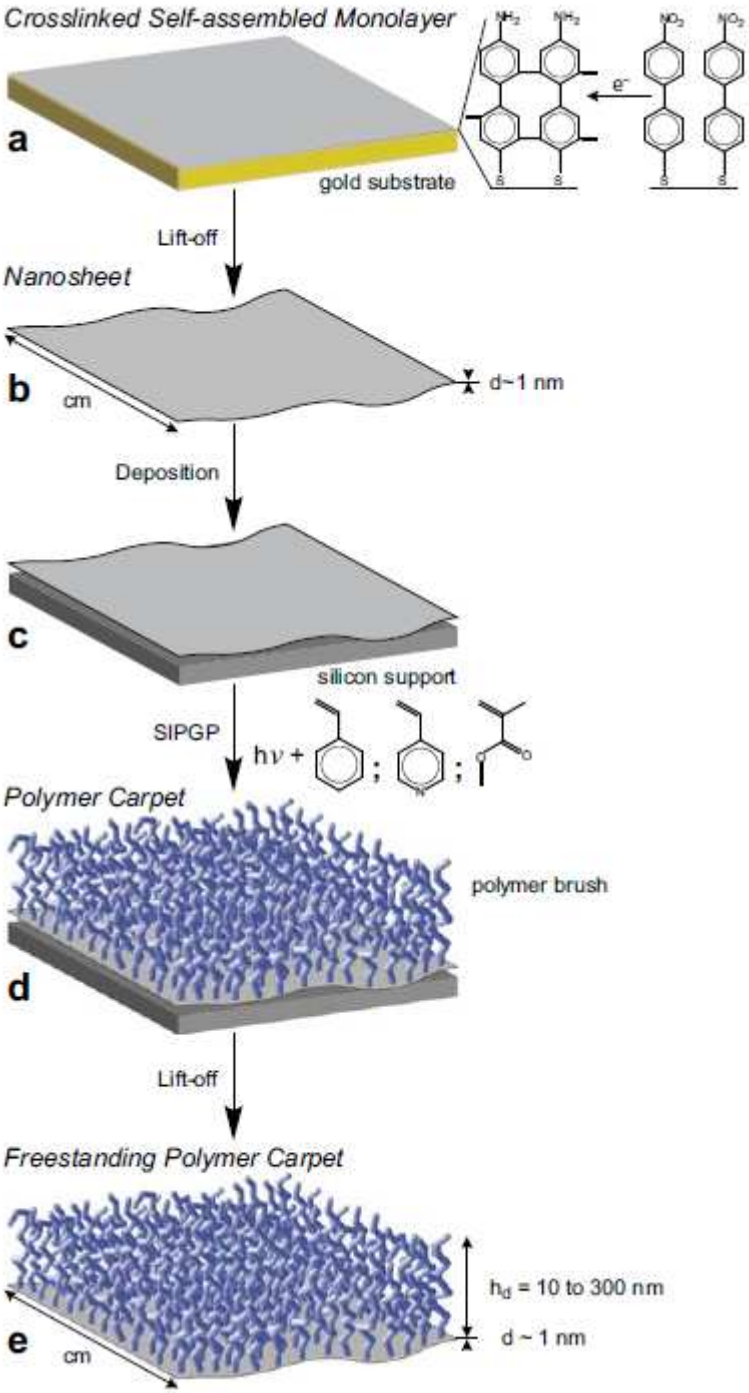

Fig. 47 Scheme of the preparation of polymer carpets: (a) A crosslinked cABT SAM is prepared by electron irradiation of NBT SAMs and (b) detached by dissolving the gold substrate with a KI/I_2 solution. (c) The nanosheet is deposited on a silicon substrate with thin silicon oxide or silicon nitride layer. (d) Supported polymer carpets are obtained by SIPGP of a vinyl monomer (styrene, 4-vinylpyridine or MMA). (e) Freestanding polymer carpets are obtained by dissolving the underlying layer (Si_3N_4) with HF. (Images taken from reference 113)

5.3 Mechanical characterization with bulge test

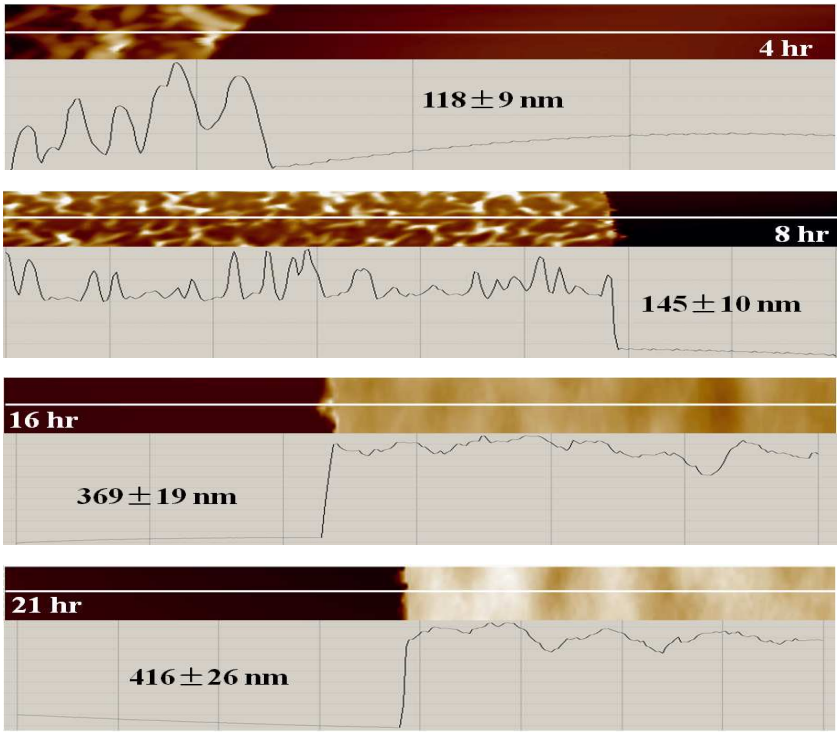

Fig. 48 The AFM height images and line profiles of polymer carpets transferred on silicon substrates with polymerization time and the corresponding thicknesses marked on figures.

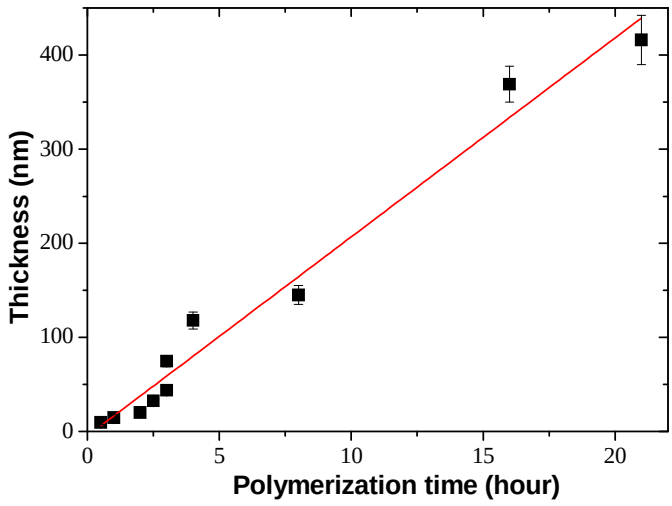

Fig. 49 Thicknesses of the PS carpets determined via an AFM instrument as a function of polymerization time.

First of all, thickness determination of polymer carpets is very crucial for the mechanical characterization. The thicknesses are linearly proportional to the UV irradiation time. However data scattering is more prominent from different sample preparing conditions. One should not just rely on the thickness derived from polymerization time. In order to obtain much more precise thicknesses, we use an AFM instrument to measure polymer carpets that were transferred on the silicon substrate. Over five different positions on the membrane edges are scanned with the AFM and five line profiles out of each position are taken to calculate the mean value of thicknesses. At lower polymerization time, their morphology indicates that a layer of flat and homogeneous film was formed on the surface. However, buckling structures were found in the polymer carpet with longer polymerization time. The AFM images and the corresponding line profiles are presented in fig. 48, where polymerization time and thicknesses were marked on those figures. The relationship between thicknesses and polymerization time is shown in fig. 49.

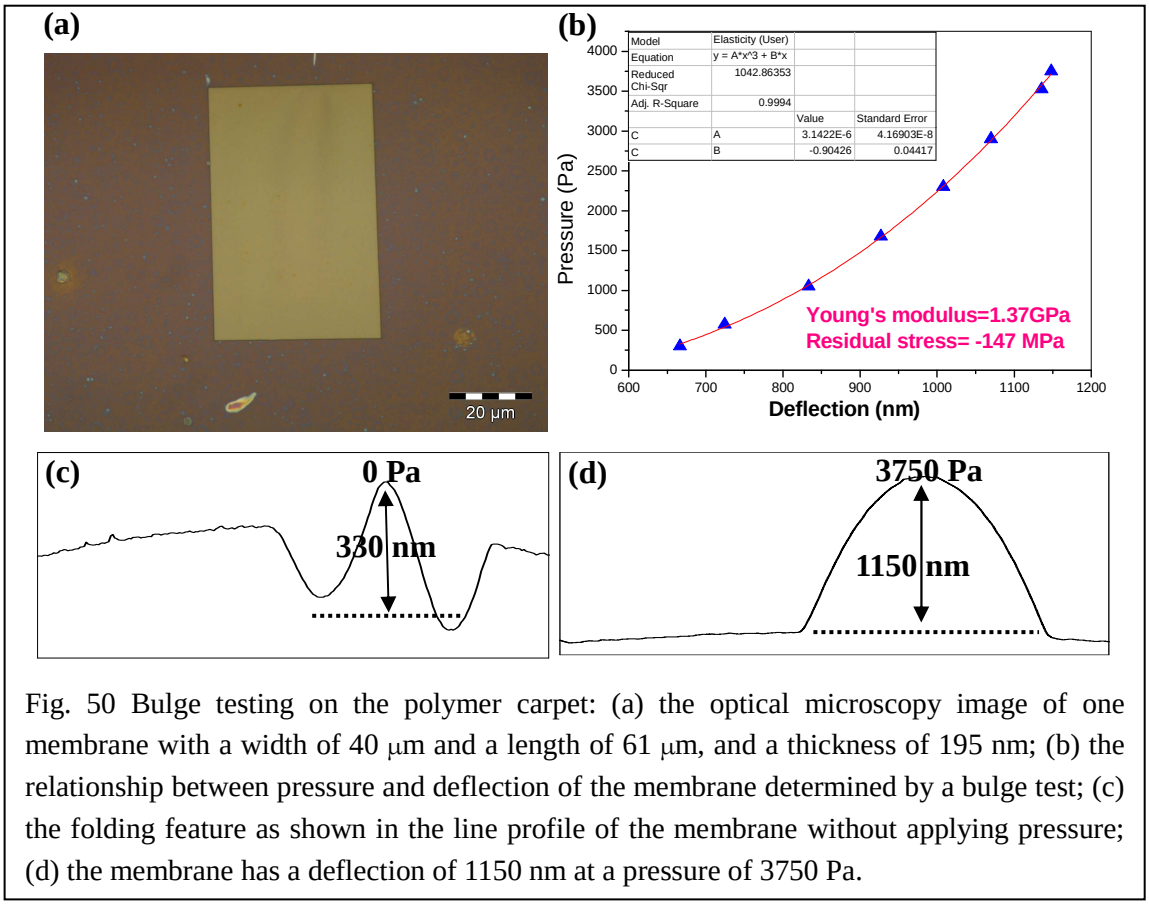

Fig. 50 Bulge testing on the polymer carpet: (a) the optical microscopy image of one membrane with a width of 40 μm and a length of 61 μm, and a thickness of 195 nm; (b) the relationship between pressure and deflection of the membrane determined by a bulge test; (c) the folding feature as shown in the line profile of the membrane without applying pressure; (d) the membrane has a deflection of 1150 nm at a pressure of 3750 Pa.

A bulge test has been used for characterizing the mechanical properties of polymer carpets. Fig. 50 shows the experiment data from one polystyrene (PS) carpet with an UV irradiation time of 8 hr. From the optical microscopy image one can see small folding feature across the membrane. The line profile of the AFM image clearly reveals that the fold has a height distribution of ~330 nm. After applying some pressure, the fold disappeared and displayed an arc profile, as shown in fig.50d. Its Young's modulus is determined as 1.37 GPa and residual stress as −147 MPa that could be explained by its existing folding feature.

Since polymer carpets are considered to be a composite system which consists of soft polymer brushes and a relatively rigid two-dimensional framework. Contributions from both components have to be taken into account. By means of mixture law [116, 117], the Poisson's ratio of the composite system is used to calculate Young's modulus and residual stress:

$$\upsilon_c = \Phi_1 \upsilon_1 + \Phi_2 \upsilon_2 \tag{48}$$

where υ_c represents the Poisson's ratio of the composite system, υ_1 and υ_2 are Poisson's ratio of each component, Φ_1 and Φ_2 the volume fraction of each component. Since PS has a Poisson's ratio of 0.34 and the NBPT nanosheet is assumed to have a Poisson's ratio of 0.35, the Poisson's ratio of this composite is taken as 0.35 to simplify the calculations.

Therefore, Young's modulus and residual stress can be determined for each component of the system using mixture formula:

$$E_{composite} = \frac{t_{NBPT}}{t_{total}} E_{NBPT} + \frac{t_{PS}}{t_{total}} E_{PS} \tag{49}$$

$$\sigma_{composite} = \frac{t_{NBPT}}{t_{total}} \sigma_{NBPT} + \frac{t_{PS}}{t_{total}} \sigma_{PS} \tag{50}$$

where E_i and σ_i represent Young's modulus and residual stress of composite system and two components, t_{NBPT} and t_{PS} represent the thickness of each

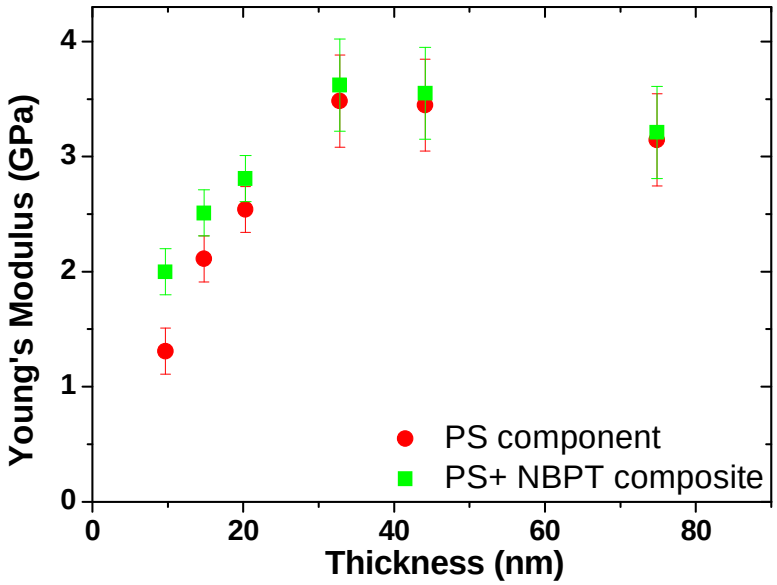

Fig. 51 Young's moduli of PS carpets of different thickness with (green squares) and without (red dots) the contribution of a NBPT nanosheet. (Image from reference 113)

component. According to our knowledge of NBPT nanosheets, Young's modulus is taken as 8 GPa and thickness is estimated to be 1 nm for theoretical calculations.

Fig. 51 shows a clear relationship between Young's modulus and the PS carpets layer thicknesses. As a whole, PS carpets have a Young's modulus in the range of 1~4 GPa which are lower than that of NBPT nanosheets. When the thicknesses are over 30 nm, Young's modulus get saturated at 3~4 GPa, which are very close to the PS's bulk value of 3.0~3.6 GPa. However, PS carpets experience a decrease in stiffness with a decrease of thickness smaller than 20 nm. The mixture law has been used to extract Young's modulus of the PS brushes component from the whole composite system, which is shown as red dots in the graph. It was found that the PS brushes component has a Young's modulus of ~1.3 GPa for the thinnest PS carpet. Our findings are in agreement with a recent report on PS brushes on solid substrates by Tsukruk et al [118], where they also reported that Young's modulus are significant lower than that of bulk PS. It can be explained that the ordering of the polymer chains in the brush morphology with lower polymer chain entanglement and the spatial constraints within the layer are responsible for the specific mechanical properties for thin brush layers.

5.4 Mechanical characterization with nanoindentation

Microindentation was commonly used to perform hardness testing. It can be used to study fine scale changes in hardness, either intentional or accidental. The Vickers and the Knoop tests are two most common microindentation tests. While the trend of miniaturization and fast development in nanotechnology requires new methods for the mechanical characterization of nanoscale materials and structures. Nanoindentation was established in such way that the penetration as a function of the applied load was recorded, instead of observing the dimensions of the residual indentation area in microindentation.

The mechanical properties of a substrate-film system can be determined by means of nanoindentation that is able to distinguish the deformation of individual components in the system. SAMs on a metal surface have been investigated by means of nanoindentation technique with a constant harmonic frequency [119]. It is shown that a different functional tail group of SAMs gives rise to the variation of phase angles and bulk density of alkyl chains may have an influence on the harmonic contact stiffness. It is quite challenging to carry out nanoindentation on a 1 nm thin carbon nanosheet. We have done some preliminary nanoindentation tests on carbon nanosheets and the technique was not sufficient to characterize them. The contact point between indenter and nanosheets is difficult to determine because of the uncertainty in the range of a few nanometers. Furthermore, the contribution of the substrate brings big difficulties to data analysis. Polymer carpet with a larger thickness was measured with nanoindentation.

In order to calibrate the nanoindentation instrument, first tests were performed on a Corning fused silica reference material. Continuous stiffness tests were performed up to an indentation depth of 2000 nm in Corning reference material. The material was deformed at a constant strain rate of 0.05 and this indicates that continuous values of modulus and hardness in fused silica are 72 GPa and 9.7 GPa, respectively, which are in agreement with typical values of fused silica reference.

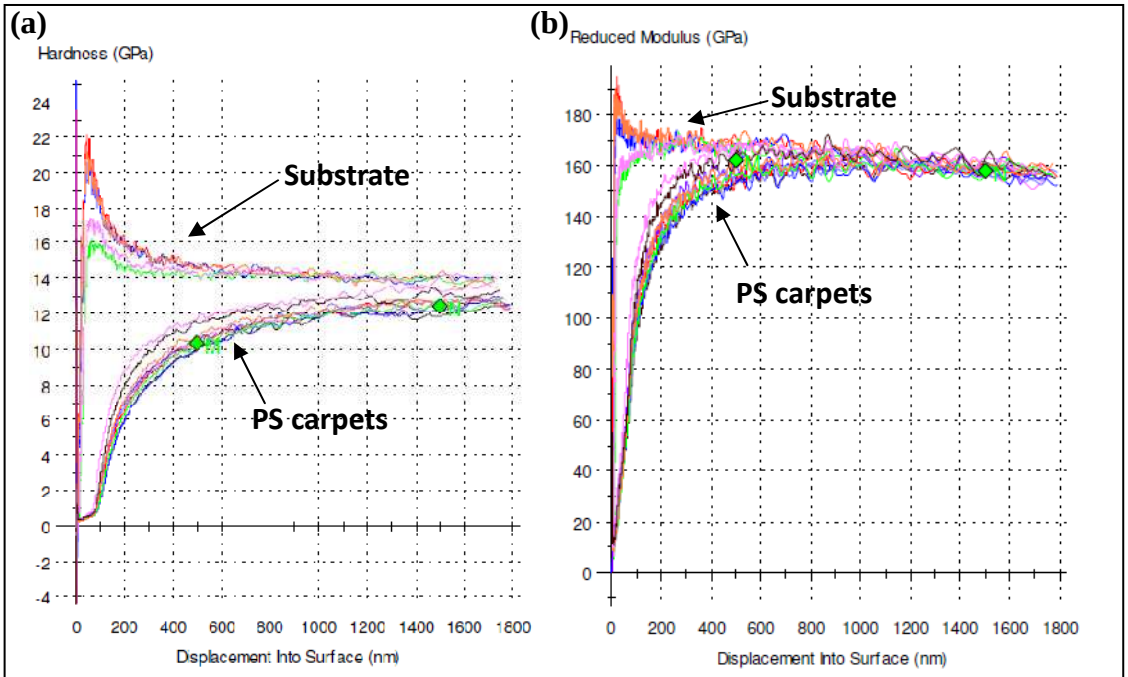

Fig. 52 (a) Hardness as a function of indentation depth on a PS carpet and its reference substrate; (b) Reduced moduli as a function of indentation depth on the PS carpet and its reference substrate.

As a next experiment, continuous indents to a depth of around 2000 nm were performed both on the sample with polymer carpets that have been transferred on the silicon substrate and on the substrate as a reference. All the experimental results were shown in fig. 52. Hardness and reduced moduli for both PS carpets and reference substrate as a function of displacement into surface were directly determined from measurements and presented together for comparison.

The reduced modulus E_r is determined from the slope of the unloading curve and calculated from the contact stiffness contributed from both indenter tip and sample.

$$\frac{1}{E_r} = \frac{1-\nu_i^2}{E_i} + \frac{1-\nu_s^2}{E_s} \tag{51}$$

where E_i and E_s indicate the elastic modulus of indenter tip and sample, ν_i and ν_s indicate Poisson's ratio of indenter tip and sample. In our case, a Berkovich pyramidal tip was used which has the elastic modulus of 1140 GPa and ν_i of 0.07. The moduli of PS carpets were computed and the results were presented in table 11.

Table 11 Statistical average modulus and hardness for polymer carpets and the substrate

	Polymer Carpets		Substrate	
	Young's Modulus (GPa)	Hardness (GPa)	Young's Modulus (GPa)	Hardness (GPa)
1	68.7	0.68	199.2	19.46
2	81.9	0.87	195.4	18.70
3	87.5	0.97	183.2	15.71
4	81.1	0.86	196.7	19.17
5	72.7	0.74	184.3	16.77
6	73.7	0.73		
7	85.3	0.89		
8	104.0	2.02		
9	87.9	0.99		
Mean	82.5	0.97	191.8	17.96
Std. Dev.	10.5	0.41	7.4	1.64
% COV	12.7	42.08	3.8	9.14

In fig. 52b, the substrate has a reduced modulus of about 168 GPa. It had a hardness of 18 GPa at an indentation depth of 80 nm. Although the PS carpet has a thickness of 120 nm, the hardness and reduced modulus for PS carpet even at an indentation depth of 80 nm showed clearly that substrate played a decisive role. On the one hand, it turns out that PS carpets can be easily distinguished from the substrate underneath and the nanoindentation is demonstrated to be a useful technique; On the other hand, the substrate effect was found to be too prominent to characterize intrinsic modulus of a PS carpet with a thickness of 120 nm. Much higher uncertainties could be expected for thinner PS carpets.

In summary, we presented the fabrication and mechanical characterization of polymer carpets which is a composite system of carbon nanosheets and polymer brushes. Both bulge testing and nanoindentation were used to determine the mechanical properties of polymer carpets. With big uncertainty in characterizing polymer carpets with nanoindentation instrument, we come to the conclusion that current nanoindentation is not yet suitable for the characterization of ultrathin nanomembranes such as carbon nanosheets.

Summary and outlook

Summary

The present work in this thesis focused on the mechanical characterization of carbon nanosheets that are prepared from the low energy electrons induced cross-linking of biphenyl-based self-assembled monolayers. For this purpose, we employed a novel bulge test for characterizing freestanding thin films, in order to apply tensile stress with a well-controlled gas pressure and to probe the resultant nanometer-scale deformation of carbon nanosheets with an AFM. CBPS nanosheets were directly prepared on silicon wafers with window-structured silicon nitride membranes as a sacrificial material. The AFM was used to scan the membranes and the resultant deflection as a function of applied gas pressure was used to determine Young's modulus and the residual stress of CBPS nanosheets. This was termed as the "line scanning method". However, regarding BPT and NBPT nanosheets, they were prepared on Au substrates and the transferring process had to be carried out. The line scanning method was not reliable for these carbon nanosheets due to the presence of a tiny amount of contamination from the PMMA on the surface. We developed a central point method to probe the deflection at the center of the membrane without scanning it. Calibration was carried out and it was demonstrated that the two methods were in good agreement.

At first, the adhesion between a carbon nanosheet and a substrate was estimated in order to prove that the van der Waals interaction guarantees neither slipping nor peeling during the gas pressure loading. We found that carbon nanosheets tended to conform to the substrate with the same corrugation wavelength and amplitude, even on substrates with different surface roughness. Apart from that, the adhesion between an AFM tip and a freestanding carbon nanosheet was also measured. The mixed van der Waals-capillary force was believed to dominate the interaction. We observed that the pull-off force between a tip and a nanosheet supported by a substrate was 5~6

times higher than that of between a tip and a suspended nanosheet.

The results focused on electron irradiation effects on the mechanical properties of carbon nanosheets that were prepared from various molecules. It was found that the mechanical stability was not enough to support freestanding carbon nanosheets with an electron irradiation dose of less than 20 mC/cm^2. A few intact membranes may come into being due to increasing cross-linkages with a dose from 30 to 40 mC/cm^2. The mechanical stiffness begun to stabilize with an electron doses above 50 mC/cm^2. Young's modulus range from 6 GPa to 8 GPa for BPT nanosheets and from 8 GPa to 10 GPa for NBPT nanosheets. CBPS nanosheets exhibit a Young's modulus in the range of 10~12 GPa and show a slight increase at higher electron doses. The mechanism can be understood by substrate conductivity and resultant different crosslinking for CBPS nanosheets on Si_3N_4 substrate.

Carbon nanosheets exhibit typical viscoelastic behavior as high polymers. Hysteresis, creep and relaxation were observed and the minimum strain that causes creep was determined. The creep rate increases with stress levels and appears to be rather stable in the range of 10^{-6} s^{-1}. The ultimate tensile strength of carbon nanosheets was also determined with a bulge test. BPT and NBPT nanosheets have tensile strengths ranging from 400 MPa to 700 MPa.

Multilayer carbon nanosheets have been successfully fabricated. The average Young's modulus is demonstrated to be very similar to that of the single layer carbon nanosheet. Annealing treatment in UHV leads to a structural transformation of carbon nanosheets. An increased graphitization was observed in Raman spectra which also indicated a decreased crystallite size. The mechanical characterization also demonstrated an increased Young's modulus upon an annealing treatment.

Moreover, polymer brushes grafted on biphenyl-based nanosheets provide a new class of material termed as "polymer carpet", which is considered as an adaptive nanomembrane in actuators and sensors. Bulge testing and nanoindentation were used to characterize the mechanical properties of polymer carpets.

Outlook

We have shown the fabrication and mechanical characterization of carbon nanosheets. They were demonstrated to act as a sensitive pressure sensor. We expect that carbon nanosheets could serve as a diaphragm in microphones, which is very sensitive to sound. As far as we know, on the macroscopic scale, the physics of sound is well understood. On the micro- and nanoscale, where macromolecules, membranes and supramolecular assemblies constitute living cells, the role of sound is less clear. We would expect that the motions of cellular membranes and of molecular machines inside the cells generate fluctuating pressure changes, i.e. sound.

A sufficiently small, yet sensitive microphone that can operate in the vicinity and inside cells is crucial for such sound measurements. We expect that supramolecular assemblies in a living cell generate sound in the MHz and GHz range. A microphone that operates inside a living cell must thus be able to detect sound in the GHz range. There the short attenuation length (2 µm at 5 GHz in water [120]) requires a correspondingly small distance between the source of the sound and the microphone.

The size of a nano microphone must be small enough so that it can be moved to different extra- and intracellular regions to detect sound levels with spatial resolution. Its dimensions should thus not exceed a few 100 nm. The active element in a microphone is an elastic membrane (diaphragm). In a nano-microphone, the diaphragm must be extremely small, thin and still elastic.

In the near future we want to build a functional nano-microphone with a carbon nanosheet diaphragm with a size of 100x100 nm^2 or smaller. We will optimize the microphone's performance and utilize it for sound measurements in liquids and in the vicinity of living cells. Due to its miniature size, the microphone might penetrate through the cell membrane and detect sound inside of living cells. We thus aim at investigating the intensity and the frequencies of sound at different extra- and intracellular locations, as well as in different physiological and developmental states of a living cell.

Abbreviations

2D	two-dimensional
AFM	atomic force microscope
AT	n-alkanethiol
BP	benzophenone
BPT	1,1'-biphenyl-4-thiol
cABT	crosslinked 4’-amino-1,1’-biphenyl-4-thiol
CBPS	4'-[(3-trimethoxysilyl)propoxy]-[1,1'-biphenyl]-4-carbonitril
CPD	critical point drying
DEA	dissociative electron attachment
DFT	density functional theory
DMF	dimethylformamide
DMT	Derjagin Muller and Toropov
EPR	electron paramagnetic resonance
EQCM	electrochemical quartz crystal microbalance
ESD	electron stimulated desorption
FT-IRRAS	fourier transform infrared reflection absorption spectroscopy
FWHM	full width at half maximum
GIXD	grazing incidence X-ray diffraction
HF	hydrofluoric acid
HRTEM	high-resolution transmission electron microscope
HTMECH	high-throughput mechanical characterization
IPN	interpenetrating hybrid networks
IR	infrared spectroscopy
IRAS	infrared reflection-absorption spectroscopy
JKR	Johnson, Kendall and Roberts
LEAD	low-energy atomic diffraction
MEMS	micro- electro-mechanical systems
MONT	montmorillonite
NBPT	4'-Nitro-1,1'-biphenyl-4-thiol
NEXAFS	near edge X-ray absorption fine structure spectroscopy
OTS	*n* -octadecyltrichlorosilane
PA	polyamide
PAN	polyacrylonitrile
PDMS	Poly (dimethysiloxane)
PE	polyethylene
PMMA	poly(methyl methacrylate)
PP	poly(propylene)
PS	polystyrene
SAED	selected area electron diffraction
SA-LbL	spin-assisted layer-by-layer

SAMs	self-assembled monolayers
SEM	scanning electron microscope
SERS	surface enhanced Raman spectroscopy
SIP	surface-initiated polymerization
SIPGP	self-initiated photografting and photopolymerization
SIMS	static secondary ion mass spectroscopy
SLSI	super-large-scale integration
SPR	surface plasmon resonance
STM	scanning tunneling microscope
TEM	transmission electron microscope
UHV	ultrahigh vacuum
UPS	UV-photoelectron spectra
XPS	X-ray photoelectron spectroscopy

List of Figures

List of Tables

References

[1] W.A. Chalifoux, R.R. Tykwinski, **Nature Chemistry**, doi:10.1038/nchem.828, 2010
[2] J. Sakamoto, J. Heijst, O. Lukin, A.D. Schlueter, **Angewandte. Chem. Int. Ed.** 48, 1030, 2009
[3] F. Behroozi, **Langmuir**, 12, 2289, 1996
[4] J.C. Meyer, A.K. Geim, M.I. Katsnelson, K.S. Novoselov, T.J. Booth, S.Roth, **Nature**, 446, 60, 2007
[5] I. Langmuir, **J. Am. Chem. Soc.** 39, 1848, 1917
[6] I. Langmuir, **Trans. Faraday Soc.** 15, 62, 1920
[7] K. Blodgett, **J. Am. Chem. Soc.** 57, 1007, 1935
[8] W. C. Bigelow, D. L. Pickett, W. A. Zisman, **J. Colloid Interface Sci.** 1, 513, 1946
[9] J. Sagiv, **J. Am. Chem. Soc.** 102, 92, 1980
[10] R. G. Nuzzo, D. L. Allara, **J. Am. Chem. Soc.** 105, 4481, 1983
[11] G. M. Whitesides, P. E. laibinis, **Langmuir**, 6, 87, 1990
[12] J. E. Houston, H. I. Kim, **Acc. Chem. Res.** 35, 547, 2002
[13] L. Qian, F. Tian, X. Xiao, **Tribol. Lett.** 15, 169, 2003
[14] X. Yang, S. S. Perry, **Langmuir**, 19, 6135, 2003
[15] J. Aizenberg, A. J. Black, G. M. Whitesides, **J. Am. Chem. Soc.** 121, 4500, 1999
[16] A. Salomon, D. Cahen, S. Lindsay, J. Tomfohr, V. B. Engelkes, C. D. Frisbie, **Adv. Mater.** 15, 1881, 2003
[17] M. Mrksich, J. R. Grunwell, G. M. Whitesides, **J. Am. Chem. Soc.** 117, 12009, 1999
[18] E. Ostuni, B. A. Grzybowski, M. Mrksich, C. S. Roberts, G. M. Whitesides, **Langmuir**, 19, 1861, 2003
[19] M. Himmelhaus, F. Eisert, M. Buck, M. Grunze, **J. Phys. Chem. B**, 104, 576, 2000
[20] K. Shimazu, I. Yagi, Y. Sato, K. Uosaki, **Langmuir**, 8, 1385, 1992
[21] P. Fenter, A. Eberhardt, P. Eisenberger, **Science**, 266, 1216, 1994
[22] R. F. DeBono, G. D. Loucks, D. D. Manna, U. Krull, **J. Can. J. Chem.** 74, 677, 1996
[23] E. Barrena, C. Ocal, M. Salmeron, **J. Chem. Phys.** 111, 9797, 1999
[24] F. Bensebaa, R. Voicu, L. Huron, T. H. Ellis, E. Kruus, **Langmuir**, 13, 5335, 1997
[25] R. G. Nuzzo, B.R. Zegarski, L.H. Dubois, **J. Am. Chem. Soc.** 109, 733, 1987
[26] H.M. Schessler, D.S. Karpovich, G.J. Blanchard, **J. Am. Chem. Soc.** 118, 9645, 1996
[27] T.Y.B. Leung, P. Schwartz, G. Scoles, F. Schreiber, A. Ulman, **Surf. Sci.** 458, 34, 2000
[28] S. Frey, V. Stadler, K. Heister, W. Eck, M. Zharnikov, M. Grunze, B. Zeysing, A. Terfort, **Langmuir**, 17, 2408, 2001
[29] P. E. Laibinis, R. L. Graham, H. A. Biebuyck, G. M. Whitesides, **Science** 254, 981, 1991
[30] F. Martin, P.D. Burrow, Z. Cai, P. Cloutier, D. Hunting, L. Sanche, **Phys. Rev. Lett.** 93, 68101, 2004
[31] B. Boudaiffa, P. Cloutier, D. Hunting, M.A. Huels, L. Sanche, **Science** 287, 1658, 2008
[32] K. Seshadri, K. Froyd, A.N. Parikh, D. L. Allara, M. J. Lercel, H.G. Craighead, **J. Phys. Chem.** 100, 15900, 1996
[33] M. Zharnikov, M. Grunze, **J. Vac. Sci. Technol. B** 20, 1793, 2002
[34] H. U. Mueller, M. Zharnikov, B. Voelkel, A. Schertel, P. Harder, M. Grunze, **J. Phys.**

Chem. B 102, 7949, 1998
[35] R.L. Garrel, J.E. Chadwick, D.L. Severance, N.A. McDonald, D.C. Myles, **J. Am. Chem. Soc.** 117, 11563, 1995
[36] D.A. Hutt, G.J. Leggett, **J. Mater. Chem.** 9, 923, 1999
[37] M.A. Huels, P.C. Dugal, L. Sanche, **J. Chem. Phys.** 118, 11168, 2003
[38] C. Zhou, A. Trionfi, J.W.P. Hsu, A.V. Walker, **J. Phys. Chem. C** 114, 9362, 2010
[39] W. Geyer, V. Stadler, W. Eck, M. Zharnikov, A. Gölzhäuser, M. Grunze, **Appl. Phys. Lett.** 75, 2401, 1999
[40] W. Eck, V. Stadler, W. Geyer, M. Zharnikov, A. Gölzhäuser, M. Grunze, **Adv. Mater.** 12, 805, 2000
[41] A. Gölzhäuser, W. Eck, W. Geyer, V. Stadler, T. Weimann, P. Hinze, M. Grunze, **Adv. Mater.** 13, 806, 2001; W. Geyer, V. Stadler, W. Eck, A. Gölzhäuser, M. Grunze, M. Sauer, T. Weinmann, P. Hinze, **J. Vac. Sci. Technol. B** 19, 2732, 2001
[42] A. Turchanin, D. Käfer, M. El-Desawy, C. Wöll, G. Witte, A. Gölzhäuser, **Langmuir**, 25, 7342, 2009
[43] P. Cabrera-Sanfelix, A. Arnau, D. Sanchez-Portal, **Phys. Chem. Chem. Phys.** 12, 1578, 2010
[44] Johnson, K. L. (1985) *Contact Mechanics* (Cambridge University Press, Cambridge)
[45] Derjaguin B.V., Muller V.M., Toropov Yu.P., **J. Colloid. Interface Sci.** 53, 314, 1975
[46] Image redrawn from J.W.S. Hearle, J.T. Sparrow, P.M. Cross, 1972
http://www.biologie.uni-hamburg.de/b-online/e03/03e.htm
[47] Universal curve:
http://www.phys.au.dk/~philip/pictures/physicsfigures/physicsfigures.html
[48] Agilent Nanoindenter G200 from: http://www.home.agilent.com/
[49] J.W. Beams: Mechanical properties of thin films of gold and silver, in *Structure and Properties of Thin Films*, John Wiley and Sons, New York, 1959, P. 183.
[50] H. Itozaki, *Mechanical Properties of Composition Modulated Copper-Palladium*, Ph.D. Dissertation, Northwestern University (1982)
[51] J.J. Vlassak, *New experimental techniques and analysis methods for the study of mechanical properties of materials in small volumes*, Ph.D. Dissertation, Standford University, 1994
[52]H. Vatanabe, T. Ohzono, T. Kunitake, **Macromolecules** 40, 1369, 2007
[53] Y. Xiang, X. Chen, J.J. Vlassak, **J. Mater. Res.** 20, 2360, 2005
[54] P. Martins, P. Delobelle, C. Malhaire, S. Brida, D. Barbier, **Eur. Phy. J. Appl. Phys.** 45, 10501, 2009
[55] C. Lee, X. Wei, J.W. Kysar, J. Hone, **Science**, 321, 385, 2008
[56] E.W. Schweitzer, M. Göken, **J. Mater. Res.** 22, 2902, 2007
[57] S. Timoshenko, S. Woinowsky-Krieger, *Theory of Plates and Shells*, McGraw-Hill, New York, P. 400, 1959
[58] P. Lin, *The In-Situ Measurement of Mechanical Properties of Multilayer-Coatings*, Ph.D. Dissertation, 1990
[59] J. J. Vlassak, W. D. Nix, **J. Mater. Res.** 7, 3242, 1992
[60] L. Gross, F. Mohn, N. Moll, P. Liljeroth, G. Meyer, **Science**, 325, 1110, 2009
[61] P. Martins, P. Delobelle, C. Malhaire, S. Brida and D. Barbier, **Eur. Phys. J. Appl. Phys.**

45, 10501, 2009
[62] U. Komaragiri, M.R. Begley, and J.G. Simmonds, **J. Appl. Mech.** 72, 203, 2005
[63] O.N. Scott, M.R. Beglez, U. Komaragiri, T.J. Mackin, **Acta materialia** 52 , 4877, 2004
[64] J. L. Sormana, S. Chattopadhyay, J. C. Meredith, **Rev. Sci. Instrum.**, 76, 062214, 2005
[65] C. Lee, X. Wei, J.W. Kysar, J. Hone, **Science**, 321, 385, 2008
[66] J. E. Sader, J.W.M. Chon, P. Mulvaney, **Rev. Sci. Instrum.** 70, 3967, 1999
[67] K.T. Wan, S. Guo, D.A. Dillard, **Thin Solid Films**, 425, 150, 2003
[68] IUPAC Compendium of Chemical Terminology:
http://old.iupac.org/publications/compendium/index.html
[69] R. Maboudian, C. Carraro, **Annu. Rev. Phys. Chem.** 55, 35, 2004
[70] U. Srinivasan, M.R. Houston, R.T. Howe, R. Maboudian, **J. Microelectromech. Syst.** 7, 252, 1998
[71] J.N. Israelachvili, *Intermolecular and Surface Forces* (second edition), Academic Press, 1992.
[72] A. Gupta, G. Chen, P. Joshi, S. Tadigadapa, P.C. Eklund, **Nano Lett.**, 6, 2667, 2006
[73] S. Sonde, F. Giannazzo, V. Raineri, E. Rimini, **J. Vac. Sci. Technol. B**, 27, 868, 2009
[74] J.B. Brzoska, I. Ben Azouz, F. Rondelez, **Langmuir**, 10, 4367, 1994
[75] S. Perutz, J. Wang, E.J. Kramer, C.K. Ober, **Macromolecules**, 31, 4272, 1998
[76] Z.H. Aitken, R. Huang, Submitted in 2010.
[77] M. He, A.S. Blum, D.E. Aston, C. Buenviaje, R.M. Overney, R. Luginbuhl, **J. Chem. Phys.** 114, 1355, 2001
[78] L.D. Landau, E.M. Lifshitz, *Theory of Elasticity*, Butterworth-Heineman, Oxford, 1996
[79] A.E.H. Love, *A treatise on the Mathematical Theory of Elasticity*, Dover, New York, P.163, 1944
[80] R. Lakes, **Science**, 235, 1038, 1987
[81] R. Henda, M. Grunze, A.J. Pertsin, **Tribology Letters**, 5, 191, 1998
[82] W. Kiridena, V. Jain, P. K. Kuo, G. Liu, **Surf. Interface Anal.** 25, 383, 1997
[83] V. B. Engelkes, C. D. Frisbie, **J. Phys. Chem. B**, 110, 10011, 2006
[84] F. W. DelRio, C. Jaye, D. A. Fischer, R. F. Cook, **Applied Physics Letters** 94, 131909, 2009
[85] O. L. Blakslee, **Journal of Appllied Physics** 41, 3373, 1970; P. Hess, **Applied Surface Science**, 106, 429, 1996; S.J. Cho, K.R. Lee, K.Y. Eun, J.H. Han, D.H. Ko, **Thin Solid Films**, 341, 207, 1999;
http://www.matweb.com;
http://www.esi.umontreal.ca/accelrys/materials/insight400P/polymer/11-QSPR_1.doc.html
[86] Christine L. A. Lamont, John Wilkes, **Langmuir**, 15, 2037, 1999
[87] A. Turchanin, D. Käfer, M. El-Desawy, C. Wöll, G. Witte, A. Gölzhäuser, **Langmuir**, 25, 7342, 1999
[88] Mohamed El-Desawy, *Characterization and Application of Aromatic Self-Assembled Monolayers*, Ph. D. Dissertation, Bielefeld University, 2007
[89] V.R. Regel', T.B. Boboev, N.N. Chernyi, **Mekh. Polim.** 3,442, 1969
[90] F. Bueche, *Physical Properties of Polymers*, John Wiley & Sons, P. 203~206, 1962.
[91] J. Yang, Z. Zhang, K. Friedrich, A.K. Schlarb, **Macromol. Rapid Commun.** 28, 955, 2007

[92] M. Grandbois, M. Beyer, M. Rief, H. C. Schaumann, H. E. Gaub, **Science**, 283, 1727, 1999; G. I. Bell, **Science**, 200, 618, 1978; A. Garg, **Phys. Rev. B**, 51, 15592, 1995; Y. Suzuki, O. K. Dudko, **Phys. Rev. Lett.** 104, 048101, 2010
[93] H. Watanabe, T. Ohzono, T. Kunitake, **Macromolecules**, 40, 1369, 2007
[94] A. Beyer, A. Godt, I. Amin, C.T. Nottbohm, C. Schmidt, J. Zhao, A. Gölzhäuser, **Phys. Chem. Chem. Phys.** 10, 7233, 2008
[95] N. Ballav, M. Zharnikov, **J. Phys. Chem. C**, 112, 15037, 2008
[96] T. Kyotani, N. Sonobe, A. Tomita, **Nature**, 331, 331, 1988
[97] J. Khanderi, J.J. Schneider, Z. Anorg. **Allg. Chem.** 635, 2135, 2009
[98] A. Turchanin, M. El-Desawy, A. Gölzhäuser, **Appl. Phys. Lett.** 90, 053102, 2007
[99] A. Turchanin, A. Beyer, C.T. Nottbohm, X. Zhang, R. Stosch, A. Sologubenko, J. Mayer, P. Hinze, T. Weimann, A. Gölzhäuser, **Adv. Mater.** 21, 1233, 2009
[100] K. S. Novoselov, A. K. Geim, S. V. Morozov, D. Jiang, M. I. Katsnelson, I. V. Grigorieva, S. V. Dubonos, A. A. Firsov, **Nature**, 438, 197, 2005
[101] C. Gomez-Navarro, R. T. Weitz, A. M. Bittner, M. Scolari, A. Mews, M. Burghard, K. Kern, **Nano Lett.** 7, 3499, 2007
[102] F. Tuinstra, J.L. König, **J. Composite Mater.** 4, 492, (1970)
[103] A. Bosak, M. Krisch,M. Mohr, J. Maultzsch, C. Thomsen, **Phys. Rev. B** 75, 153408, 2007
[104] A. Gölzhäuser, W. Eck, W. Geyer, V. Stadler, T. Weimann, P. Hinze, M. Grunze, **Adv. Mater.** 13, 806, 2001
[105] X. Wang, C. Drew, S.H. Lee, K.J. Senecal, J. Kumar, L.A. Samuelson, **Nano Lett.** 2, 1273, 2000
[106] C. Guizard, P. Lacan, **New J. Chem.** 18, 1097, 1994
[107] M. B. Shiflett, H.C. Foley, **Science** 285, 1902, 1999
[108] H.M. Keizer, B.R. Dorvel, M. Andersson, D. Fine, R.B. Price, J.R. Long, A. Dodabalapur, I. Köper, W. Knoll, P.V. Anderson, R.S. Duran, **ChemBioChem** 8, 1246, 2007
[109] R. Vendamme, S.Y. Onoue, A. Nakao, T. Kunitake, **Nature Materials** 5, 494, 2006
[110] H. Watanabe, T. Kunitake, **Adv. Mater.**, 19, 909, 2007
[111] C. Jiang, S. Markutsya, Y. Pikus, V. V. Tsukruk, **Nature Materials**, 3, 721, 2004
[112] U. Schmelmer, A. Paul, A. Küller, M. Steenackers, A. Ulman, M. Grunze, A. Gölzhäuser, R. Jordan, **Small,** 3, 459, 2007
[113] I. Amin, M. Steenackers, N. Zhang, A. Beyer, X. Zhang, T. Pirzer, T. Hugel, R. Jordan, A. Gölzhäuser, **Small**, 15, 1623, 2010
[114] B. Ranby, W.T. Yang, O. Tretinnikov, **Nuclear Instruments and Methods in Physics Research B** 151, 301, 1999
[115] S.J. Li, C.G. Li, *Polymer photochemistry principles and applications*, Fudan University Press: Shanghai, P. 110, 1993
[116] O.R. Shojaei, A. Karimi, **Thin Solid Films** 332, 202, 1998
[117] P. Martins, P. Delobelle, C. Malhaire, S. Brida, D. Barbier, **Eur. Phys. J. Appl. Phys.** 45, 10501, 2009
[118] D. Julthongpiput, M. LeMieux, V. V. Tsukruk, **Polymer** 44, 4557, 2003
[119] C. Chang, J. Liao, **Nanotechnology** 19, 315703, 2008
[120] J. Shaham-Bronstein, D. Sarid, W. Low, **J. Chem. Phys.** 52, 3201, 1970

Acknowledgements

First of all, I would like to thank my advisor Prof. Armin Gölzhäuser for the chance he gave me to work in this subject, for his valuable instruction, patience and support. He gave me many opportunities to present my work in conferences and I also thank him for the recommendation which gave me the opportunity to participate in the Lindau Nobel Laureates Meeting. His vision in science and his care for the students has deeply influenced me.

I would also like to thank PD Dr. André Beyer for his precise instructions in my experiments and data analysis, and for his patience in our discussions. I also want to thank Dr. Berthold Vökel for his help and suggestions in using many instruments. I would like to thank my previous colleague Dr. Laxman Kankate who was very glad to help me in my work and my life. I should mention that PD Dr. Andrey Turchanin also gave me some helpful instructions in my presentation and experiments.

Particularly, I would like to thank Frau Lorentzen for her help in various documents, for her warmhearted instructions in my life, for her patience in bringing me newspapers and magazines continuously, for her love and patience in correcting the grammatical errors in my thesis.

I would like to thank Dr. Ihsan Amin for his help in preparing polymer carpets for me. Particularly I thank Nils Mellech for sputtering samples with gold, for his valuable discussions and for his countless help in my daily life. I also want to mention undergraduate student Shourjya Sanyal for helping me with Piezoresistivity measurements, as well as Melanie Dannemeyer for her diligence in sample preparation. To my other colleagues, I specially thank Henning Vieker who helped me with the work in LEEPS and his help with XPS, Matthias Büenfeld for his help with XPS and annealing experiments, Nils-Eike Weber for his help in annealing experiments, Mark Schnietz for his help with XPS, Dr. Zhikun Zheng and Dr.

Christoph Thilo Nottbohm for their suggestions and help as chemists, Melek Uygun, Dr. Min Ai, Dr. Dan Matei, Dr. Udo Werner, Heiko Muzik, Andreas Winter, Elina Oberländer, Anna Aguf, Daniel Emmrich for their help and discussions.

Especially, I would like to thank Prof. Dr. Peter Reimann who read through my thesis and gave me helpful suggestions and comments. I also want to thank Dr. Holger Pfaff from Agilent Technologies who helped me with the nanoindentation experiments.

I would like to thank Isaiah Pinilla in New Hampshire who helped me in correcting the grammatical errors in my thesis within a limited time period. I also thank all the people from Chinese Christian Fellowship, International Student Fellowship and International Baptist Church in Bielefeld who have helped and supported me through these years in Bielefeld.

Finally, I thank my parents for their support. I would also like to thank my wife Jing for her advices to my presentations from her perspective, for her support and encouragement all the time.